Development of Statistical Shape and Intensity Models of Eroded Scapulae to Improve Shoulder Arthroplasty

by

Azita Sharif Ahmadian
BSc, University of Tehran, 2016

A Thesis Submitted in Partial Fulfillment
of the Requirements for the Degree of

MASTER OF APPLIED SCIENCE
in the Department of Mechanical Engineering

Supervisory Committee

Development of Statistical Shape and Intensity Models of Eroded Scapulae to Improve Shoulder Arthroplasty

by

Azita Sharif Ahmadian
BSc, University of Tehran, 2016

Supervisory Committee

Dr. Josh Giles, Department of Mechanical Engineering
Supervisor

Dr. Keivan Ahmadi, Department of Mechanical Engineering
Departmental Member

Abstract

Reverse Total shoulder arthroplasty (RTSA) is an effective treatment and a surgical alternative approach to conventional total shoulder arthroplasty for patients with severe rotator cuff tears and glenoid erosion. To help optimize RTSA design, it is necessary to gain insight into the geometry of glenoid erosions and consider their unique morphology across the entire bone. One of the most powerful tools to systematically quantify and visualize the variation of bone geometry throughout a population is Statistical Shape Modeling (SSM); this method can assess the variation in the full shape of a bone, rather than of discrete anatomical features, which is very useful in identifying abnormalities, planning surgeries, and improving implant designs. Recently, many scapula SSMs have been presented in the literature; however, each has been created using normal and healthy bones. Therefore, creation of a scapula SSM derived exclusively from patients exhibiting complex glenoid bone erosions is critical and significantly challenging.

In addition, several studies have quantified scapular bone properties in patients with complex glenoid erosion. However, because of their discrete nature these analyses cannot be used as the basis for Finite Element Modeling (FEM). Thus, a need exists to systematically quantify the variation of bone properties in a glenoid erosion patient population using a method that captures variation across the entire bone. This can be achieved using Statistical Intensity Modeling (SIM), which can then generate scapula FEMs with realistic bone properties for evaluation of orthopaedic implants. Using an SIM enables researchers to generate models with bone properties that represent a specific, known portion of the population variation, which makes the findings more generalizable.

Accordingly, the main purpose of this research is to develop an SSM and SIM to mathematically quantifying the variation of bone geometries in a systematic manner for the complex geometry of scapulae with severe glenoid erosion and to determine the main modes of variation in bone property distribution, which could be used for future FEM studies, respectively.

To draw meaningful statistical conclusions from the dataset, we need to compare and relate corresponding parts of the scapula. To achieve this correspondence, 3D triangulated mesh models of 61 scapulae were created from pre-operative CT scans from patients who were treated with RTSA and then a Non-Rigid (NR) registration method was used to morph one Atlas point cloud to the shapes of all other bones. However, the more complex the shape, the more difficult it is to maintain good correspondence. To overcome this challenge, we have adapted and optimized a NR-Iterative Closest Point (ICP) method and applied that on 61 eroded scapulae which results in each bone shape having identical mesh structure (i.e., same number and anatomical location of points).

To assess the quality of our proposed algorithm, the resulting correspondence error was evaluated by comparing the positions of ground truth points and the corresponding point locations produced by the algorithm. The average correspondence error of all anatomical landmarks across the two observers was 2.74 mm with inter and intra-observer reliability of ±0.31 and ±0.06 mm. Moreover, the Root-Mean-Square (RMS) and Hausdorff errors of geometric registration between the original and the deformed models were calculated 0.25±0.04 mm and 0.76±0.14 mm, respectively.

After registration, Principal Component Analysis (PCA) is applied to the deformed models as a group to describe independent modes of variation in the dataset. The robustness of the SSM is also evaluated using three standard metrics: compactness, generality, and specificity. Regarding compactness, the first 9 principal modes of variations accounted for 95% variability, while the model's generality error and the calculated specificity over 10,000 instances were found to be 2.6 mm and 2.99 mm, respectively.

The SIM results showed that the first mode of variation accounts for overall changes in intensity across the entire bone, while the second mode represented localized changes in the glenoid vault bone quality. The third mode showed changes in intensity at the posterior and inferior glenoid rim associated with posteroinferior glenoid rim erosion which suggests avoiding fixation in this region and preferentially placing screws in the anterosuperior region of the glenoid to improve implant fixation.

Keywords: Scapula, Osteoarthritis, Reverse Total Shoulder Arthroplasty, Non-Rigid registration, Statistical Shape Modeling, Statistical Intensity Modeling, Principal Component Analysis.

Table of Contents

List of Tables

List of Figures

Glossary

Abduction	The movement of a limb away from the midline of the body. The opposite of abduction is adduction.
Arthroplasty	A surgical procedure for any joint intended to restore joint function by replacing natural articular surfaces with a prosthetic device.
Atlas	Specific source model for a population dataset.
Fossa	A shallow depression in the bone surface.
Glenoid	Shallow articular cavity of the shoulder joint.
Hounsfield Unit	A relative quantitative measurement used in the interpretation of computed tomography (CT) images.
Image Segmentation	The process of partitioning an image into multiple segments to locate objects and boundaries.
Morphology	The study of the size, shape, and structure of organisms and the relationships of their constituent parts.
Osteoarthritis	Degeneration of joint cartilage and the underlying bone caused by wear and tear, as well as biological processes.
Registration	The process of transforming different sets of data into one reference coordinate system.
Scapula	Shoulder blade bone.

Abbreviations

BMD	Bone Mineral Density
CS	Coordinate System
CSA	Critical Shoulder Angle
CT	Computed Tomography
DICOM	Digital Imaging and Communications in Medicine
DOF	Degree of Freedom
FEM	Finite Element Modeling
HU	Hounsfield Unit
ICP	Iterative Closet Point
ISB	International Society of Biomechanics
JCS	Joint Coordinate System
KNN	K Nearest Neighbor
MRI	Magnetic Resonance Imaging
NR	Non-Rigid
OA	Osteoarthritis
PCA	Principal Component Analysis
PDM	Point Distribution Model
ROM	Range of Motion
RMS	Root Mean Square
RTSA	Reverse Total Shoulder Arthroplasty
SD	Standard Deviation
SIM	Statistical Intensity Modeling
SSM	Statistical Shape Modeling
SVD	Singular Value Decomposition
2D/3D	Two dimensional or three dimensional
±	Plus, or minus; prefixes magnitude of one standard deviation
°	degrees (unit of rotation)

Acknowledgments

This thesis would not have been possible without the inspiration and support of wonderful individuals; my thanks and appreciation to all of them for being part of this journey and making this thesis possible.

First and foremost, I would like to express my sincere gratitude to my supervisor Dr. Josh Giles for the continuous support of my Master's study and research, for his patience, motivation, enthusiasm, and immense knowledge. His guidance helped me in all the time of my research and writing of this thesis. I could not have imagined having a better advisor and mentor for my Master's study. I also want to express my gratitude to my committee member, Dr. Keivan Ahmadi for his insight and knowledgeable support. I would like to thank my colleagues at Orthopaedic Technologies and Biomechanics Lab for their support and help throughout my study.

Finally, my special and deepest thanks to my family for their love and support over the years. I am forever indebted to my parents for giving me the opportunities and experiences that have made me who I am.

Dedication

To my beloved parents, without whom none of my success would be possible and to my husband, for his endless love, support and encouragement.

Chapter 1
Introduction

This chapter focuses on the relevant areas which are essential to this thesis. These main topics can be divided into three major parts. The first topic explains the shoulder bone anatomy and its complexity in geometry, the second topic describes Glenoid erosion that happens clinically, and the third topic provides a brief description about Reverse Total Shoulder Arthroplasty (RTSA). At the end of this chapter, the problem definition and objectives for this thesis are detailed.

1.1 Anatomy

Anatomy is the study of the structure of the human body, which introduces functions and structural organization of living organisms. Studying anatomy gives us the knowledge of the body structures that is needed to identify the anatomical parameters. In the following sections, anatomical terminology and scapula anatomy will be discussed.

1.1.1 Anatomical terminology

In the field of biomechanics and biomedical engineering, it is important to understand musculoskeletal anatomy and be familiar with common anatomical terms. These standard terms are briefly explained in this section.

1.1.2 Standard anatomical position

To easily describe relative positions and orientations of anatomical features, it is useful to first define a standard anatomical body position. In this position, a person is standing upright with the feet together or slightly apart and facing forward, the upper limbs are at the sides with the palms facing forward and thumbs pointing away from the body, and head and eyes directed straight ahead. The standard anatomical position in human body is shown in Figure 1 [1].

1.1.3 Anatomical reference planes

Knowledge of the directional terms and reference planes is essential for study of anatomy. They are hypothetical planes used to divide the human body into different sections in order to describe the location or direction of different body structures. There are three major planes as described in Table 1 and graphically illustrated in Figure 1.

Table 1. Standard reference planes used in anatomical terminology [1].

Sagittal/ lateral plane	Divides the body vertically into symmetrical right and left sides. (The midsagittal plane located in the midline through the center of the body which all other sagittal planes are parallel to it.)
Frontal/coronal plane	Divides the body into anterior and posterior (front and back) portions and is placed at right angles to the sagittal plane.
Transverse/ axial plane	Divides the body horizontally into superior and inferior (upper and lower) portions. It is a horizontal plane through the center of the body which is parallel to the ground.

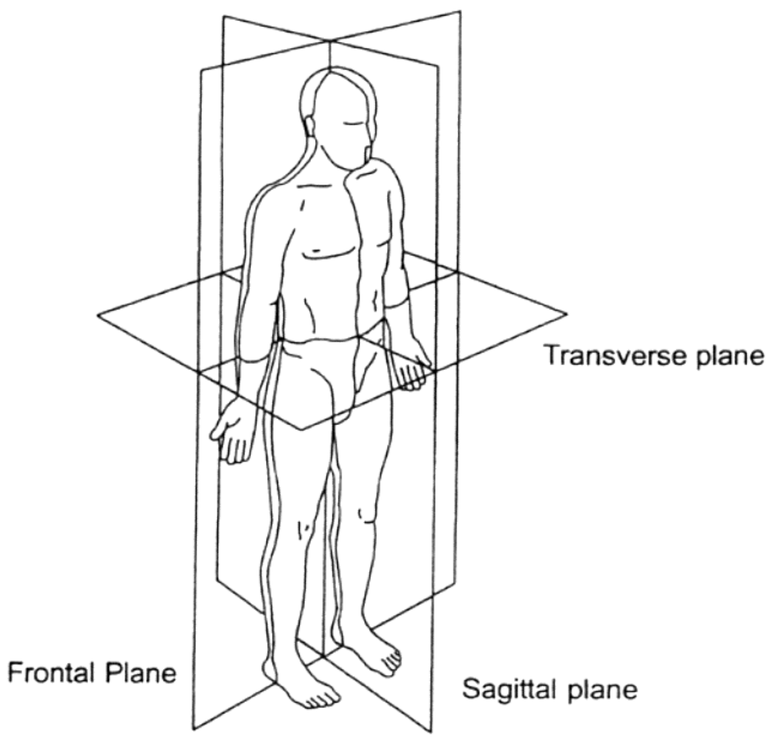

Figure 1. Illustration of standard anatomical position along with standard reference planes [2].

1.1.4 Directional terms

Certain directional terms are essential to refer to the directions of motion or to describe the relative locations of different skeletal parts. All the following terms in Table 2 are defined in standard anatomical position of human body and the schematic view of these directional terms are shown in Figure *2*.

Table 2. A list of important directional terms refers to the human body in standard anatomical position [1].

Anterior/ ventral	Describes the front or direction toward the front of the human body.
Posterior /dorsal	Opposite of anterior; describes the back or direction toward the back of the human body.
Superior /cranial	Describes a position above or higher than another part of the body; toward the head end of the human body.
Inferior/ caudal	Opposite of superior; describes a position below or lower than another part of the body or body parts away from the head.
Medial	Describes the middle or direction toward the middle of the body or toward the midline.
Lateral	Opposite of medial; describes the side or direction toward the side of the body or away from the midline.
Proximal	Describes a position in a limb that is nearer to the point of attachment or the trunk of the body. Nearest the axial skeleton, usually used for limb bones.
Distal	Opposite of proximal; describes a position in a limb that is farther from the point of attachment or the trunk of the body, farthest from the axial skeleton.

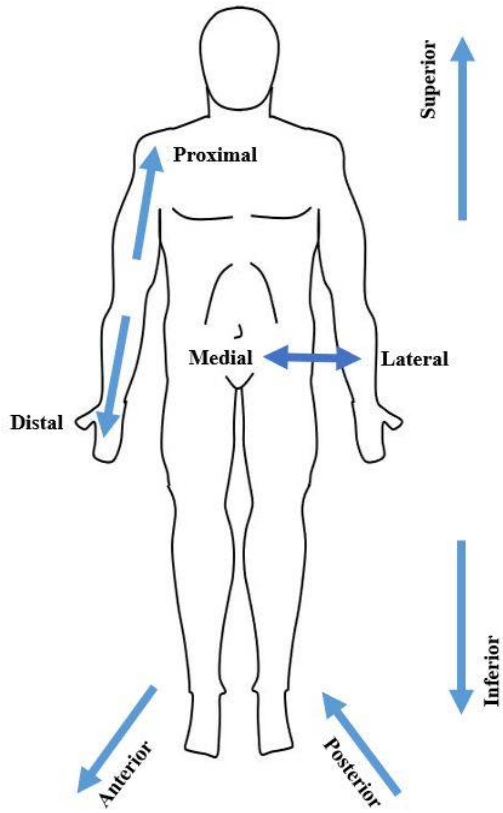

Figure 2*. Directional Terms Applied to the Human Body.*

1.1.5 The shoulder complex anatomy

The shoulder complex consists of the scapula, humerus and clavicle, which are shown in Figure 3. This unit is a group of bones, muscles, and joints. These components together allow the hand and arm to do their tasks [3]. It should be noted that the anatomical components in Figure 3, Figure 5, Figure 6, Figure 7 and Figure 9 are created using an educational software on anatomy named Complete Anatomy 2021 [4] and are labeled manually. A brief discussion of each of these bones is provided in the following sections.

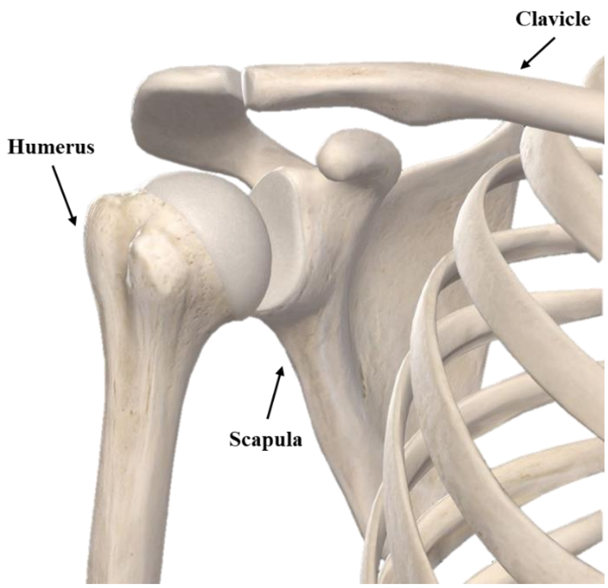

Figure 3. Illustration of shoulder complex including the scapula, humerus and clavicle.

1.1.5.1 Scapula

The scapula is known as the shoulder bone, shoulder blade, wing bone or blade bone. The scapulae (plural of scapula) are paired and roughly triangular in shape. They are located at the back of the shoulder on both side of the body. The scapula has one of the most complex structures in the human musculoskeletal system. The complexity of the scapula results from the adaptive development of the shoulder to meet human functional requirements including significant degrees of arm mobility.

In the lower limbs, one of the key functions of the bones is weight bearing; however, this is not the upper extremity's primary function. Instead, when a load applied to this unit, the scapula plays a dampening role and absorbs the load through the connected muscles [5].

Indeed, the scapula is a floating bone and it is suspended by the many muscles that connect it to the thorax. This floating nature gives the scapula a very large range of motion (ROM) and this helps to greatly increase the mobility of the attached arm and hand, which can move through a much larger excursion [3].

The scapula is categorized as a flat bone that provides a broad range of attachment sites for various muscles with differing functional roles that are critical to enabling the arm to move through its full ROM.

This complex structure is made of two large surfaces, one anterior and the other posterior, and a number of structures primarily located on the lateral side of the scapula. The anterior surface is smooth, articulates with the posterior wall of the thorax, and acts as the site for muscle attachment. The posterior side of the scapula is divided into two parts by a protruding ridge of bone called the spine; these two parts of the posterior surfaces are known as the supraspinous fossa (i.e. superior to the spine) and a large inferior surface known as the infraspinous fossa [6]. Three important features of the scapula are the complex structures known as the acromion process, coracoid process, and glenoid fossa, which are introduced briefly below and are shown in Figure 4 (It should be noted that, this figure is created and labeled using one scapula sample in our dataset).

- **Acromion process:** The above-described spine ends laterally in a large, flat surface named the acromion process. It has a roughly rectangular shape with rounded corners in the axial plane. The deltoid muscle, which elevates the arm through abduction, forms its origin along the lateral most edge of the acromion process.
- **Coracoid process:** In the lateral border of scapula, there is a hook-shaped or bent-finger-like structure named the coracoid process, which serves as an anchor for many tendons and ligaments. The tendons are the pectoralis minor, coracobrachialis, and short head of the biceps brachii muscles, and the ligaments are the coracoclavicular, coracohumeral, coracoacromial, and transverse scapular ligaments, which are explained in the next section.
- **Glenoid fossa (i.e. cavity):** The shallow cavity on the lateral side of the scapula which articulates with the head of humerus to form the glenohumeral joint, which is what lay people often think of when they say ‘shoulder’ joint. It is a ball-and-socket joint that is the major articulation of the shoulder girdle and has the greatest range of motion of any joint in the body. This large range of motion is caused by the shallow glenoid fossa and spherical shape of humeral head. Accordingly, this large range of motion provides abduction-adduction, flexion-extension, and internal-external rotations for the humerus [6].

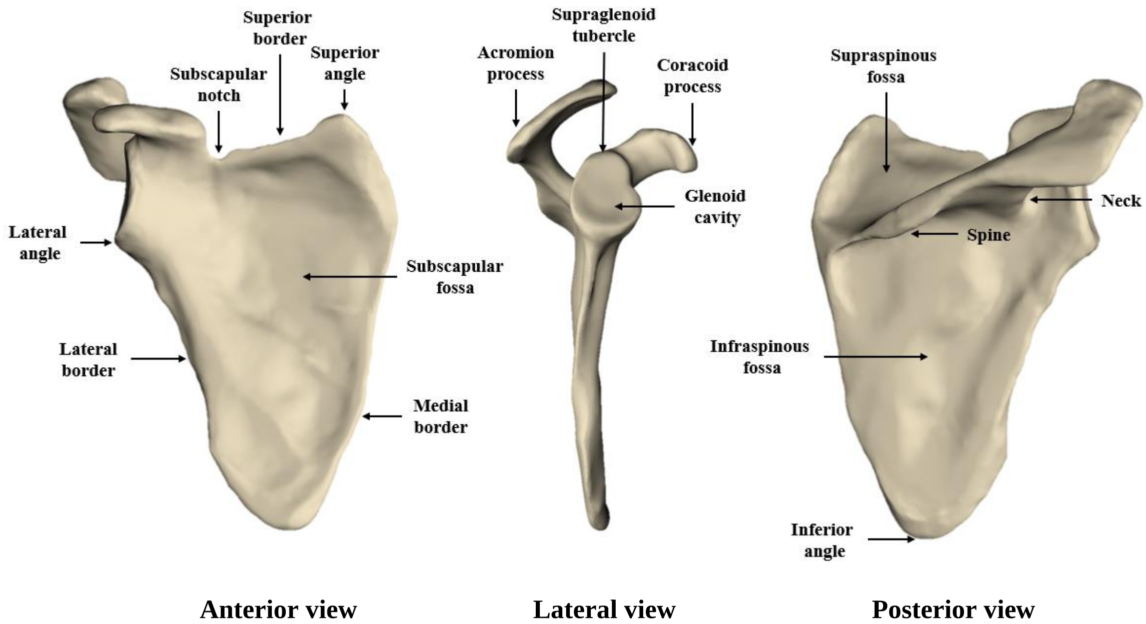

Figure 4. Scapula anatomy is presented in anterior, lateral, and posterior view.

1.1.5.2 Humerus

The humerus is the upper arm bone and the longest bone in the arm. It is composed of a head, neck, shaft, and some short processes. The proximal humerus is the humeral head that articulates with the glenoid fossa of scapula forming the glenohumeral joint. The anatomical neck is the circumferential circle around the bone that marks the inflection point where the humeral shaft begins to rapidly diverge into the humeral head anatomy.

The shaft is the main body of the humerus and has a cylindrical shape and two bony processes called the greater and lesser tuberosities. Finally, the distal humerus has two epicondyles (lateral and medial epicondyles), two processes (capitulum and trochlea), and three fossae (coronoid fossa, radial fossa, and olecranon fossa). The capitulum and the trochlea articulate with radius and ulna forearm bones respectively forming the elbow joint [6]. The humerus anatomy is shown in Figure 5.

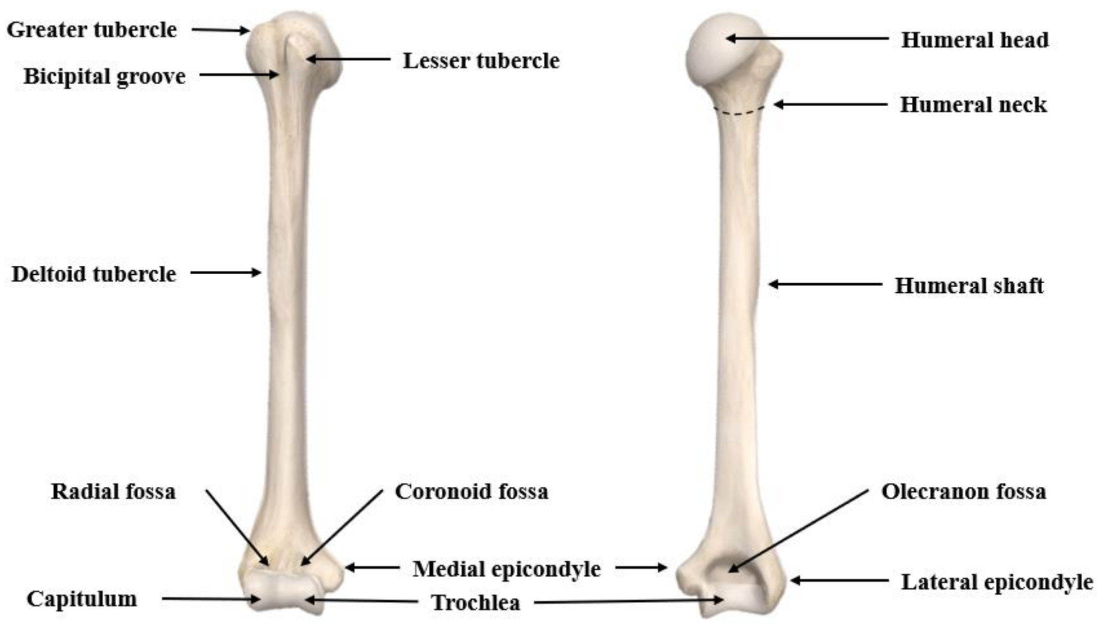

Figure 5. Humerus anatomy

1.1.5.3 Clavicle

The clavicle, or collarbone, is a large, long curved bone connecting the arm to the trunk. This is the only long bone in the human body which lies horizontally, and it links the scapula with the sternum. There are two clavicles, one on the right and one on the left. The clavicle and the scapula form the shoulder girdle, which is shown in Figure 6. The flattened lateral end of clavicle articulates with the acromion process of the scapula and form the acromioclavicular joint and the rounded medial end connects to the sternum which forms the sternoclavicular joint. There are three ligaments connected to the clavicle involving in shoulder stabilizing to the nearby bones: the acromioclavicular, the coracoclavicular and the sternoclavicular ligaments. Ligament tear and injury can cause clavicle instability [7].

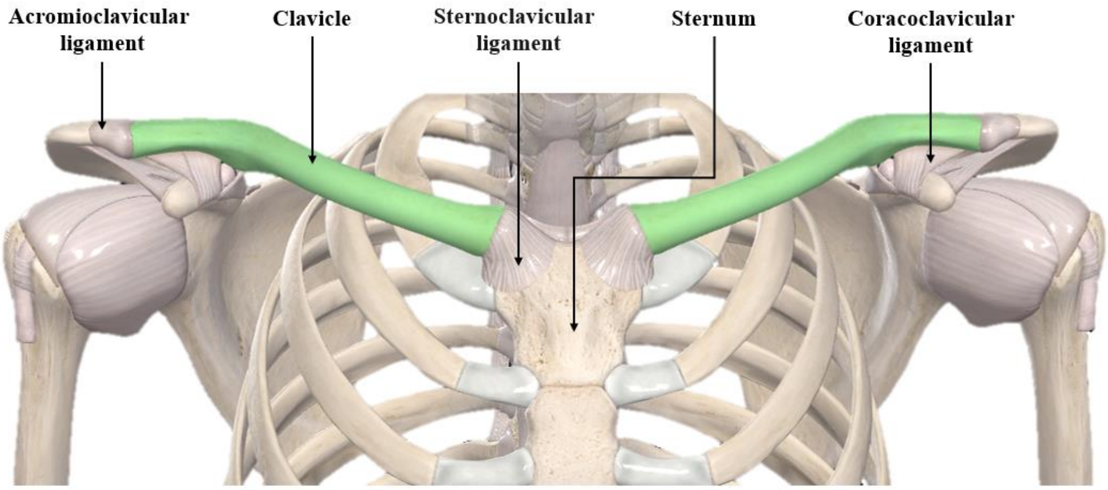

Figure 6. Clavicle anatomy

1.1.6 Shoulder ligaments

Ligaments and tendons are both made of fibrous connective tissue. Ligaments connect bone to bone and tendons, located at each end of a muscle, attach muscle to bone. The shoulder is not a single bone, but a complex arrangement of bones, ligaments, muscles, and tendons. Important ligaments in the shoulder are as follows and there are shown in Figure 7.

- **Glenohumeral ligaments (GHL):** A joint capsule is a fibrous sheath that surrounds a joint and encloses the structures of the joint. In the shoulder, the joint capsule is formed by a group of ligaments that connect the humerus to the glenoid and provide stability to the shoulder. They include the superior, middle, and inferior glenohumeral ligaments. Their responsibility is to hold the shoulder in place and keep it from dislocating.
- **Coraco-humeral ligament (CHL):** This is a broad ligament connecting the coracoid process of the scapula to the greater tubercle of the humerus and it strengthens the upper part of the joint capsule.
- **Coraco-acromial ligament (CAL):** It forms a connection between the coracoid and acromion processes, and it can limit excessive superior movement of the head of the humerus.
- **Acromio-clavicular ligament (ACL):** It links the anterior apex of acromion to the lateral end of the clavicle and serves as the primary restriction to vertical displacement.

- **Coraco-clavicular ligaments (CCL):** It is made of two ligaments, trapezoid ligaments anteriorly and conoid ligament posteriorly. It attaches the clavicle to coracoid process of the scapula. These ligaments play a key role in keeping the scapula attached to the clavicle and therefore keeping the shoulder in place. They are strong and carry a massive load.
- **Transverse humeral ligament (THL)**: It functions to hold the tendon of the long head of biceps muscle in the groove between the greater and lesser tubercle on the humerus [3], [6].

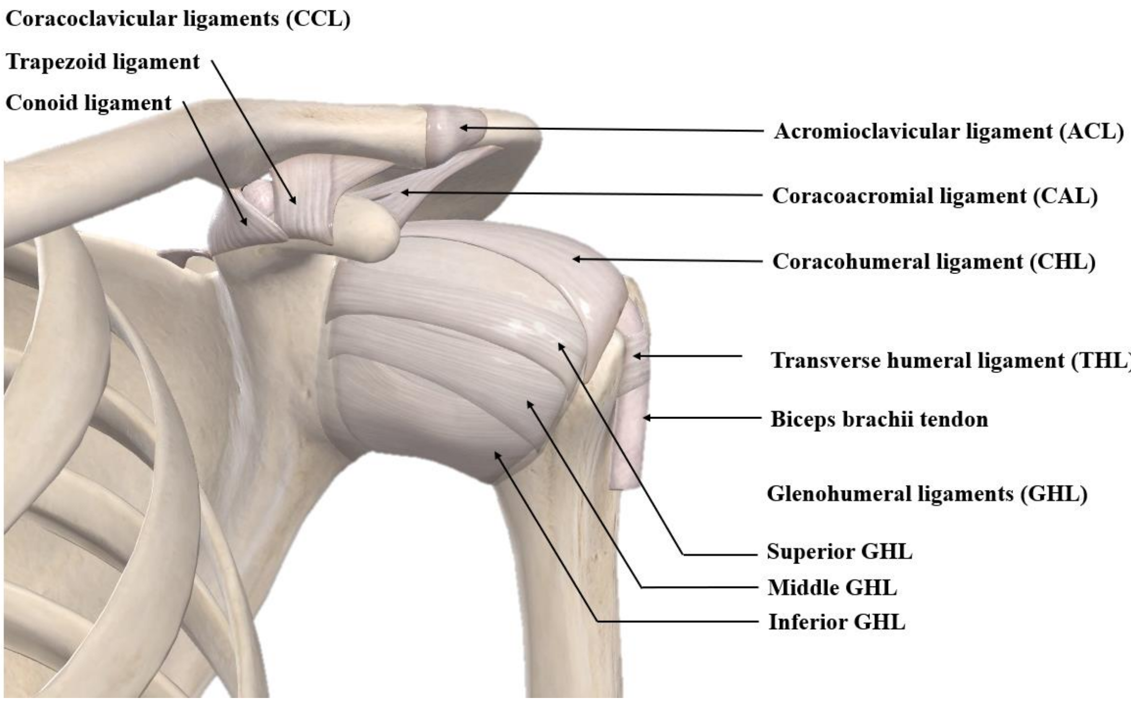

Figure 7. Scapula ligaments

1.1.7 Shoulder muscles

The skeletal muscles provide three main functions that can account for human body movement. These consist of producing movement for locomotion, maintaining postures, and stabilizing the joints.

The shoulder muscles are divided into four groups. The first one is the scapulothoracic muscles that control the motion of the scapula. Second is glenohumeral muscles that work across that joint. The third group consists of muscles that cross two or more joints. Fourth are the muscles that are not directly involved with functioning of the shoulder but have important anatomic landmarks [6].

Shoulder movement involves a large number of muscle units crossing the shoulder joint and they play an important role in the joint stability [8]. In Table 3, these muscles will be briefly explained. It should be noted that names of muscles are taken from their origin and insertion sites which are connected to bone via tendons [9].

The deltoid muscle is the largest muscle of the shoulder and is the major driver of arm elevation. It is commonly described using three sections, the anterior section from the clavicle, the middle section around the acromion and the posterior section toward the scapular spine. These three sections contribute to flexion, abduction, and extension, respectively, as well as aiding in internal and external rotation. In addition, four muscles form the rotator cuff which covers the shoulder capsule: the supraspinatus, infraspinatus, subscapularis, and teres minor.

Other muscles involved in shoulder movement are briefly introduced below [6] and some important muscles are shown in Figure 8.

Table 3. Shoulder's muscles description.

Biceps brachii	The long head originates from the supraglenoid tubercle, while the short head from the coracoid process. This muscle is responsible for elbow flexion.
Coracobrachialis	Its origin is the coracoid process. Its actions include adduction and flexion at the shoulder joint.
Deltoid	Largest muscle of shoulder. Its actions include flexion and medial rotation, abduction, extension, and lateral rotation at the shoulder joint.
Infraspinatus	It originates from the infraspinous fossa. This rotator cuff muscle helps with the raising and lowering of the upper arm.
Latissimus dorsi	It originates from the inferior angle. This flat rectangular muscle performs a variety of actions, such as adduction, extension, and medial rotation at the shoulder joint.
Levator	This group of muscles insert into the superior angle and medial border (superior to the spine). Their roles are to elevation the scapula.
Omohyoid	Its origin is the superior border (adjacent to the suprascapular notch) and causes depression of hyoid or lingual bone.
Pectoralis major	This large fan-shaped muscle stretches from the armpit up to the collarbone and down across the lower chest region. It connects to the sternum.
Pectoralis minor	The smaller of the pectoralis muscles, this muscle fans out from the upper ribs up to the shoulder area. It inserts into the coracoid process. Its actions consist of protraction and depression of the scapula.

Rhomboid major	Its insertion is the medial border (inferior to the spine). This muscle performs elevation and retraction of scapula.
Rhomboid minor	It inserts above the scapular spine. It performs actions like elevation and retraction of the scapula.
Serratus anterior	Its insertion is along the medial border, from the superior angle to the inferior angle. This muscle protracts and rotates the scapula.
Subscapularis	This is a large triangular muscle near the humerus and collarbone which originates from the subscapular fossa. It performs adduction and medial rotation at the shoulder joint and helps rotate the humerus.
Supraspinatus	This rotator cuff muscle originates from supraspinous fossa. It is responsible for abduction at the shoulder joint.
Teres major	Its origins are the posterior surface of the inferior angle and the lower part of the lateral border. Its role is to perform adduction and medial rotation at the shoulder joint.
Teres minor	It originates from the lateral border of the posterior surface. Its action consists of lateral rotation at the shoulder joint.
Trapezius	It inserts superiorly along the spine, acromion process, and clavicle. Its actions include elevation of the scapula and rotation of scapula during abduction of humerus beyond 90 degrees.
Triceps brachii	This large muscle in the back of the upper arm helps straighten the arm and elbow extension.

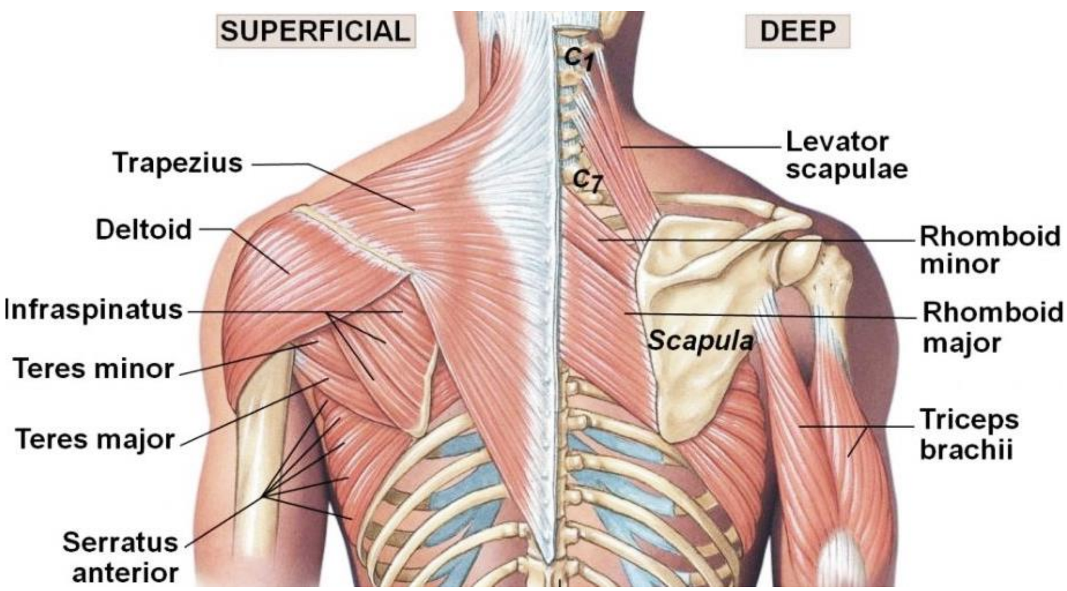

Figure 8. Shoulder muscles [10] .

1.1.8 Shoulder joints

The shoulder complex consists of four joints, namely three anatomical joints and one functional joint. The anatomical joints of shoulder are the sternoclavicular joint, the acromioclavicular joint, and the glenohumeral joint [11], whereas the scapulothoracic joint is regarded as a functional joint as it does not conform to the definition of a diarthrodial joint (see Figure 9).

- **The sternoclavicular joint:** This is a synovial joint between the sternum and the proximal end of the clavicle. It is the only articulation between the axial skeleton (i.e. the bones of the skull, vertebral column, and the ribcage) and the upper limb. The articular surfaces of the medial end of the clavicle and the sternum have unequal dimensions which makes the joint unstable. The ligamentous structure of sternoclavicular, costoclavicular ligaments and interclavicular ligaments along with the articular disc which is a fibrocartilage layer between the clavicle and the sternum participate significantly in sternoclavicular joint stability with minimum rotation [12].
- **The acromioclavicular joint**: This is a synovial joint between the lateral end of the clavicle and the acromial process. The ligaments around this joint and its joint capsule provide the joint stability whereas the joint capsule cannot maintain the joint integrity without ligaments' support. The main stabilizer of this joint is acromioclavicular ligament which prevents the joint from anteroposterior displacement. In addition, vertical displacement is prevented by the coracoclavicular ligament consists of conoid and trapezoid ligaments [12].
- **The glenohumeral joint**: This is a ball and socket type synovial joint linking the glenoid cavity of the scapula and the head of the humerus. The shallow articular surface of the glenoid fossa along with hemispherical shape of the humeral head brings large mobility to the joint. The joint capsule around the joint is extended from the glenoid fossa to the anatomical neck of the humerus. The joint friction is reduced with presence of synovial membrane, synovial bursae, and the synovial fluid. The glenohumeral ligaments discussed in section 1.1.6, and the shoulder muscles surrounding the glenohumeral joint presented in section 1.1.7 play an important role in maintaining the joint stability [8]. In the shoulder complex, the glenohumeral joint is considered as the most critical joint for

its extensive range of motion but which also predisposes this joint to injuries and joint dislocations [11].

- **The scapulothoracic joint**: This sliding joint is not considered as a true joint anatomically for its lack of joint characteristics like cartilaginous or synovial tissues. It is defined as a functional joint which is articulating the scapula with the posterosuperior part of the rib cage through the kinematic restraint provided by the acromioclavicular and sternoclavicular joints. In fact, the scapula is held against the rib cage only by muscles originated or inserted on the scapula deeply or superficially [13].

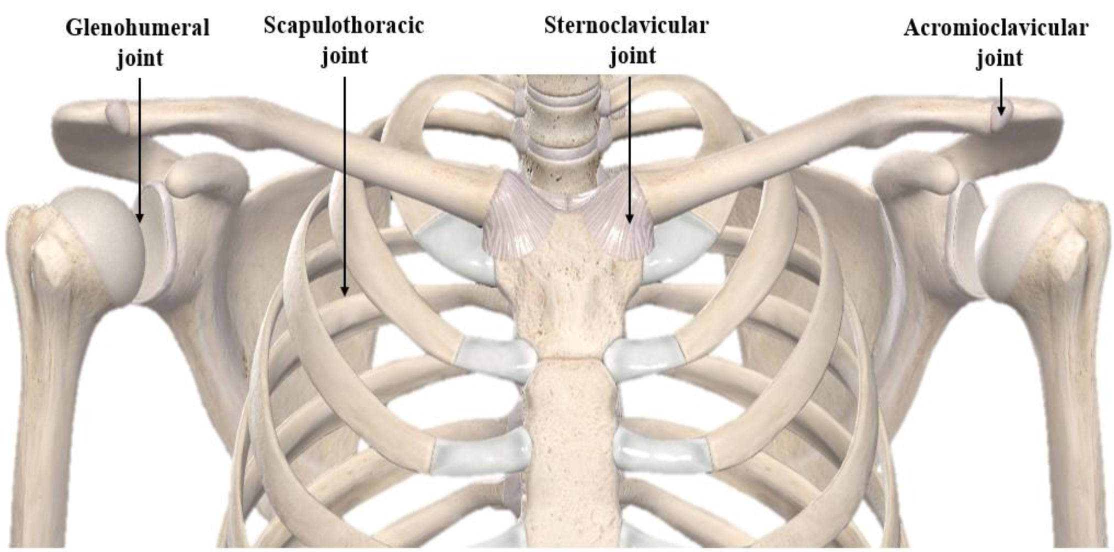

Figure 9. The anatomical joints of scapula (sternoclavicular joint, acromioclavicular joint, glenohumeral joint, and scapulothoracic joint)

1.2 Glenoid erosion

The glenohumeral joint is the most mobile joint in the human body which brings a large range of motion to the upper limb. The interaction of ligament, tendons and muscles helps the joint to keep in place during extreme movements. This significant mobility is at the expense of stability and the increased likelihood of joint injury. There are several problems and diseases associated with the shoulder joint including dislocation, separation, inflammation (tendinitis, bursitis, impingement syndrome), rotator cuff tears, frozen shoulder, fracture and arthritis [6]. In the next section, we will discuss what glenohumeral arthritis is and what causes that in human body.

1.2.1 Osteoarthritis

The most common and widespread joint disease is called arthritis. According to the statistics of Canada in 2019, 19.8 % of Canadian population (6,058,900 persons) 12 years old and over were reported as diagnosed arthritis [14]. Arthritis occurs more frequently in elderly persons and for that reason in 2019, 46.5 % of Canadian adults over the age of 65 years were diagnosed with arthritis. There are various types of arthritis and they can affect people of all ages, races, and sexes. One of the most common types of arthritis is Osteoarthritis. In osteoarthritis, the cartilage on the end of bones wears away and bone rubs against bone which is painful for patients. Many reasons can cause this loss of cartilage such as:

- Wear and tear over time
- Chronic inflammatory condition (rheumatoid arthritis)
- Trauma (fracture or dislocation)
- Osteonecrosis (bone death due to loss of blood supply)
- Infection
- Chronic rotator cuff tears (humeral head loses its proper position in the glenoid cavity)
- Post-surgical changes due to over-tightening during instability surgery
- Rare congenital and metabolic conditions

All the aforementioned reasons cause cartilage to wear away and leaves the joint vulnerable to potential risks but there are several options for patients who struggle with joint pain from simple medical treatments to advanced surgeries depending on their level of arthritis [15], [16], [17], [18], [19]. Arthroplasty or joint replacement therapy is an orthopaedic procedure which is used when medical treatments no longer relieve joint pain effectively and it helps patients to restore their joint's function. Different types of shoulder arthroplasties will be discussed in detail in section 1.3.

1.2.2 Glenohumeral osteoarthritis

Shoulder osteoarthritis occurs in the glenohumeral joint which involves the articulation between the glenoid cavity of the scapula and the proximal head of the humerus [20]. In severe cases, arthritis leads to significant bone erosion with varying morphologic features in the shape of the scapula. Therefore, understanding the pattern of glenoid and humerus erosions helps orthopedic surgeons in treatment planning including the precise pre-operative decisions they make with respect to implant selection and placement. These choices in turn affect the quality of patient outcomes and the durability of shoulder arthroplasty. The two most common categories to classify glenoid deformities are called the Walch and the Favard type classifications. The Walch classification categorizes glenoid defects that are caused by osteoarthritis and the Favard classification categorizes glenoid erosion in patients with rotator cuff arthropathy [21]. These two classifications are discussed in detail in the following sections.

1.2.3 Walch classification of glenoid erosion

Glenoid deformity and glenohumeral subluxation were characterized by Walch et al. for the first time. They used 113 scapula CT scans from males and females with primary osteoarthritis for their assessment. The initial Walch classification contained five types of glenoid morphology which is shown in Figure 10 [22].

- **A1**: centered humeral head with minor erosion.
- **A2**: centered humeral head with major central glenoid erosion.
- **B1**: posterior subluxated head without bony erosion.
- **B2**: posterior subluxated head and posterior erosion with glenoid biconcavity.
- **C**: dysplastic glenoid with at least 25° of retroversion regardless of erosion.

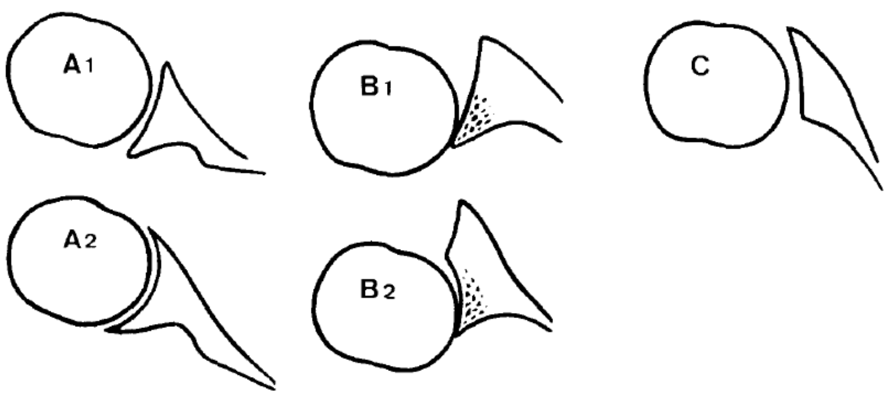

Figure 10. Initial Walch classification on glenoid deformity in primary glenohumeral osteoarthritis [23].

After the first classification, Walch and their colleagues modified and expanded their system to include more glenoid erosion patterns in order to help surgeons in treatment and predicting outcomes. Their modified classification includes the addition of types B0, B3, and D which are demonstrated in Figure 11 and they are defined as follows [24]:

- **B0**: pre-osteoarthritic posterior subluxation of the humeral head.
- **B3:** progression of the B2 deformity and characterized by uni-concavity, retroversion, posterior humeral head subluxation, and medialization.
- **D**: glenoid anteversion or anterior humeral head subluxation.

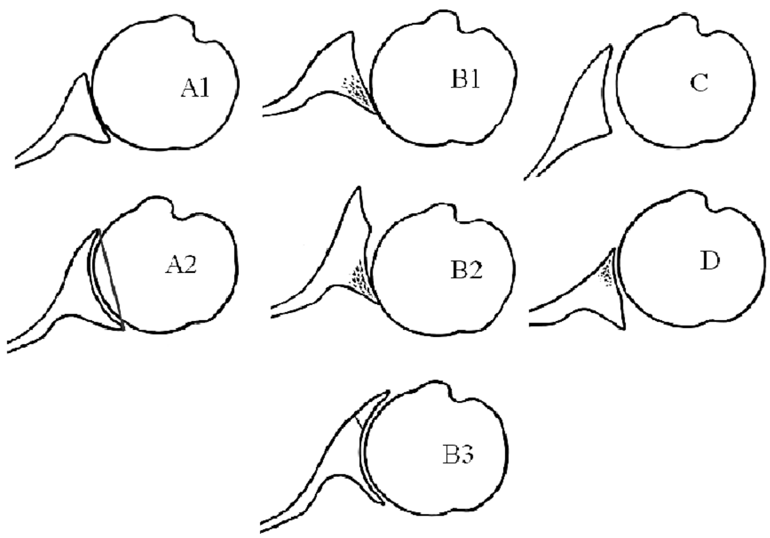

Figure 11. Schematic illustration of modified Walch classification [24].

1.2.4 Favard E-type classification of glenoid erosion

Superior glenoid bone loss is most often seen in rotator cuff tear arthropathy. This arthropathy creates glenoid erosion in the frontal plane because of humeral head migration. In 2004, Favard et al. described the most common patterns of glenoid erosion attributed to rotator cuff tear arthropathy as E-type classification. In this classification, four types of glenoid erosion were defined by varying degrees and location of glenoid erosion in the sagittal plane. In type E0, the humeral head migrated upwards without glenoid erosion. Type E1 has concentric erosion of the glenoid, while type E2 has only superior glenoid erosion. Type E3 is a progression of superior E2 type erosion extending to the inferior side of the glenoid [25]. Later in 2008, they also added a fifth type of glenoid erosion to the Favard classification. They described type E4 for inferior wear of the glenoid in which glenoid inclination is oriented downward [26]. All five types of glenoid erosion according to Favard classification are shown in Figure 12.

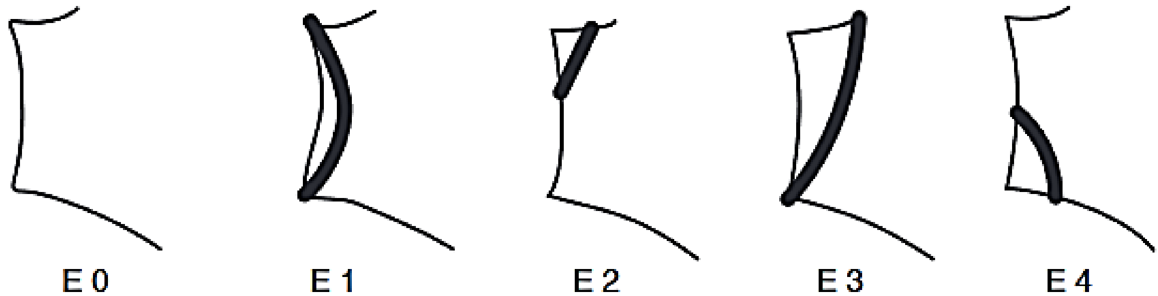

Figure 12. Schematic illustration of Favard E-type classification of glenoid erosion, E0: Humeral head migration without glenoid erosion, E1: Concentric glenoid erosion, E2: Superior glenoid erosion, E3: progression of superior E2 to the entire glenoid face and E4: Glenoid erosion isolated to inferior edge [20].

1.3 Shoulder arthroplasty

Shoulder arthroplasty or shoulder replacement surgery is recommended when patients have severe pain in their shoulder joint and conservative treatments have been found to be ineffective to relieve pain. The main purposes of shoulder arthroplasty is to eliminate pain, restore the joint function by removing damaged tissue, balancing muscles, and replace the destroyed joint with an artificial implant [27].

1.3.1 Origin of shoulder replacement

The earliest shoulder arthroplasty in a human was conducted by a French surgeon named Jules Emile Pean in 1893 on a 37 years old baker in Paris [28]. The patient reported increased strength in his arm, unfortunately, after 2 years infection required the implant to be removed.

After Pean, there were no more developments for almost 60 years and shoulder arthroplasty was not performed commonly until 1955 when Neer performed a proximal humerus hemi-arthroplasty with a Vitallium prosthesis in 12 patients [29]. The Neer work still forms the foundation for current knowledge of indications and many surgical techniques for shoulder replacement. For many years, total shoulder replacement (e.g. replacing both the humeral head and glenoid surface with anatomical implants) was the standard option for patients with rotator cuff tears and arthritis. In the 1970s, it was observed that unsatisfactory results were achieved with traditional implants in patients that had loss in the rotator cuff function, which helps to stabilize the glenohumeral joint.

Consequently, constrained designs with fully conforming humeral and glenoid implants were introduced to compensate for the stability deficit due to loss of the rotator cuff. Although some functional improvements were reported in some cases, the critical complication of these designs was rapid loosening of the glenoid components, which caused numerous revisions in patients. These loosening failures demonstrated that implants with traditional post and keel based glenoid implant fixation were insufficient to withstand the significantly higher loads experienced in patients with loss of rotator cuff function.

The aforementioned challenges in constrained shoulder arthroplasty encouraged researchers and surgeons to explore a new method of shoulder replacement that later became known as Reverse Total Shoulder Arthroplasty (RTSA). In section 1.3.3 and 1.3.4, the history of RTSA and the biomechanical aspects of RTSA designs will be discussed in detail.

1.3.2 Different types of shoulder arthroplasties

There are three different types of shoulder arthroplasties as follows:

- **Total shoulder arthroplasty (TSA):** This is a procedure in which both the humeral head and glenoid cavity are removed and replaced by artificial prosthesis. Since the glenohumeral joint is like a ball in socket joint, the humeral head is replaced by a stemmed implant with a spherical-shaped end and the glenoid is resurfaced by a small thin socket-shaped implant to mimic the anatomic structure of shoulder joint which is shown in Figure 13 [30], [27]. Also, TSA designs can be divided into three groups in terms of replacement components which are listed in Table 4.

Table 4. Main categories of total shoulder arthroplasty.

Unconstrained	In these implants, there is no mechanical constraint or physical link between the humeral head and glenoid components due to the shallow cavity of the glenoid component. The implant components attempt to mimic the normal anatomy which is shown in Figure 13 (a). They basically rely on the surrounding musculotendinous cuff for stability. As a result, musculotendinous units need to be healthy enough in order to support the shoulder joint.
Semi-constrained	These prostheses are similar to unconstrained implants and the glenoid and humeral head components are matched together but the superior glenoid component has an extension which prevents the humeral head to migrate upward which is shown in Figure 13 (b).

Fully constrained	In these implants, the humeral head and glenoid components are mechanically constrained and coupled around a fixed center of rotation which is shown in Figure 13 (c). This is theoretically a good option for those patients who have rotator cuff deficiencies, and it can prevent superior migration of the humeral component. Nowadays, this kind of design is rarely employed in shoulder arthroplasty, because it produces forces to be tolerated by the implant and interfaces rather than the surrounding soft tissues which eventually leads to fracturing of components and loosening [31].

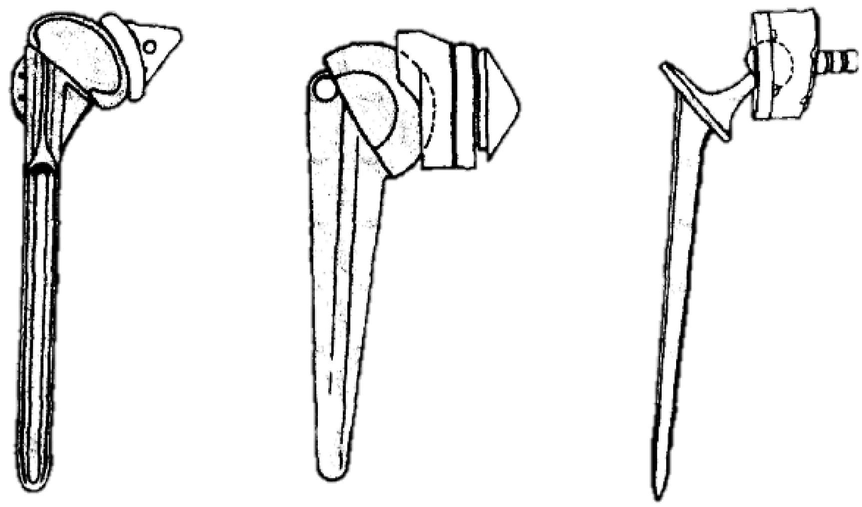

(a) **(b)** **(c)**

Figure 13. Three main categories of total shoulder arthroplasty in terms of replacement components. (a)Unconstrained, (b) Semi-constrained and (c) Fully constrained [32].

- **Shoulder hemi-arthroplasty:** It is a partial shoulder replacement that only consists of a humeral component. The proximal head of humerus is replaced with a stemmed implant and it is used when the native glenoid surface is in good condition which is shown in Figure 14 (b) [33].
- **Reverse total shoulder arthroplasty (RTSA):** In this procedure, the ball and socket parts of the shoulder joint switch sides which is opposite of its location in nature. The schematic presentation of this procedure is shown in Figure 14 (c). It is recommended for patients with damaged rotator cuff muscles. This allows the deltoid

muscle to provide movement and compensate for the forces lost due to the damaged rotator cuff muscles. It can improve the range of motion, strength, and stability of the shoulder joint [34].

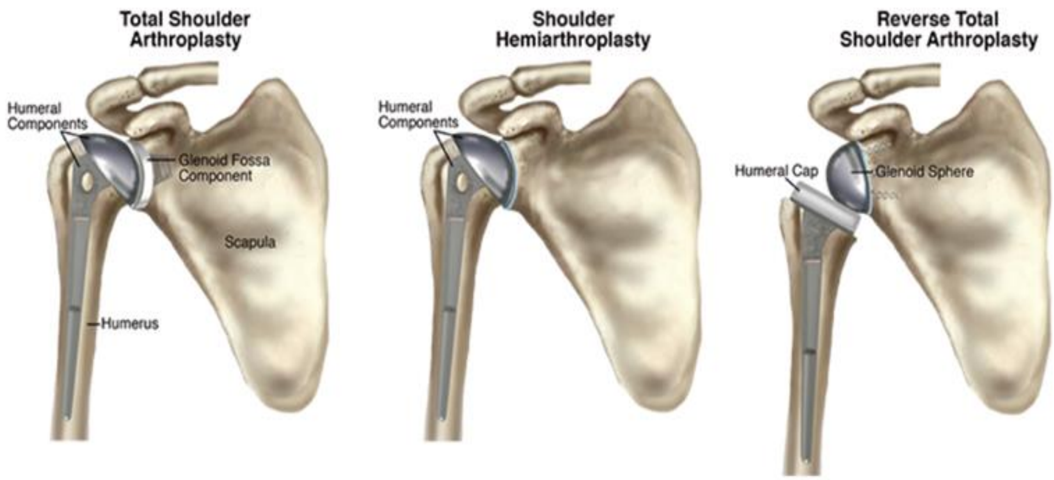

(a) **(b)** **(c)**

Figure 14. *Three different shoulder arthroplasties. (a) Total shoulder arthroplasty, (b) Hemi-arthroplasty and (c) Reverse total shoulder arthroplasty [35]*

1.3.3 History of reverse total shoulder arthroplasty

Early reverse designs in the 1970s were aimed to improve the range of motion and strength and to resolve the instability issue in previous designs but they suffered from poor scapular implant fixation. Finally, in 1985, a new concept in RTSA was proposed by Dr. Paul Grammont for the first time to address the issues which caused poor outcomes in conventional total shoulder arthroplasty. The idea of Grammont's prosthesis relied on the deltoid muscle in order to provide movement and stability which differed from the previous failed designs to treat indications involving rotator cuff deficiencies. His new concept was introduced on three principles:

1. Design the weight-bearing component as convex shape, and the supported component as concave shape.
2. Make the glenoid component large and the humeral component's surface small to have a semi-constrained articulation.

3. Make the center of rotation fixed and move it medially and distally relative to the native glenohumeral joint.

(a) **(b)**

Figure 15. (a) First Grammont reverse prosthesis in 1985 [36] and (b) Grammont Delta III prosthesis in 1991.

Although, his first generation of new reverse shoulder prostheses relieved pain from patients, several failures were reported with the cemented glenoid component. As a result, in 1991 and 1994, second and third versions of the reverse prosthesis were introduced, which significantly improved the implant's survivorship by achieving sustained implant fixation [29].

1.3.4 Biomechanical aspect of RTSA

In order to clarify the Grammont concept, comparison of muscle's function before and after RTSA will be presented. There are two fundamental factors contributing to the capability of muscles in producing limb motion; namely, the moment arm of the muscle and the muscle's force generation capability [37]. In the Grammont design, the position of the glenoid component has a significant effect by shifting the center of rotation which brings several mechanical advantages. The two important functional factors affecting the biomechanics of RTSA are as follow:

- **Reposition of center of rotation**: By shifting the center of rotation medially, the effective deltoid moment arm is increased, which is shown as L2 in Figure 16. This change helps by increasing the abduction torque the deltoid muscles can produce with the same applied force, which is beneficial for patients with rotator cuff deficiency as it compensates for the lost torque generation capabilities of these muscles.
- **Lowering the humerus position**: By this change, the humeral surface covers less than half of the area the glenoid component which reduces the torque on the glenoid interface due to friction induced tangential loads. In addition, deltoid lengthening results in increasing the deltoid muscle tension. Increasing the deltoid muscle's force which is shown as F2 in Figure 16, helps the patients to restore their arm elevation in absence of rotator cuff muscles [38] [39].

Many alternative approaches have been suggested, but the majority of modern RTSA designs continue to use the same principles.

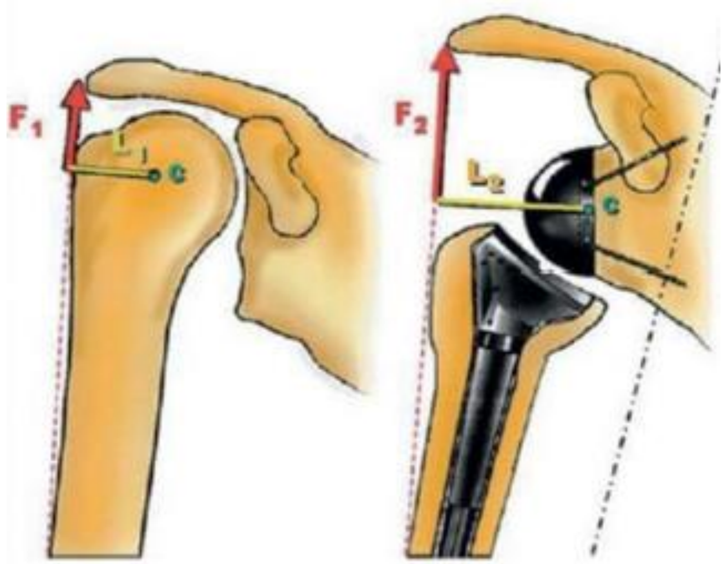

Figure 16. Illustration of moment arm of deltoid muscle and lever arm by shifting the center of the rotation[40] .

The improvements in patient's pain and range of motion have made the RTSA an increasingly popular option for surgeons. Despite the potential benefits, there are many complications associated with RTSA. The most persistent and common complications are neurologic injury during surgery, intraoperative fracture, postoperative hematoma formation, infection, scapular notching, dislocation, baseplate failure, and acromial fracture [41]. Another type of complication is geometric mismatch between the shape of patient's scapula and implant since it is necessary for scapula implants to accommodate a wide range of body sizes and shapes. Therefore, it is neccesary to have implants of differing sizes and with built in adjustability to fit well with individual patients' scapulae [42], and custom-made guides to secure guide pins in the desired angle and position [43]. Consequently, comprehensive investigations and studies on the biomechanical variations are required to address the aforementioned concerns and challenges that have arisen with the RTSA procedure.

1.4 Motivation and objectives

Many innovations and developments in orthopaedic surgery rely on computer assisted technologies as they provide quick access to preoperative data, improved visualization, and the ability to more thoroughly analyse and evaluate patient characteristics. In disease diagnosis and disorder recognition the analysis of organ shape and the properties of organ tissue is a critical consideration. Similarly, in shoulder arthroplasty, it is critical to understand the variations in bone shape and bone material property distributions that characterise a specific disorder in a patient subcategory in order to design implants that work optimally within that specific patient population. As well, being able to compare an individual patient's shape and bone property characteristics to gain insight about variation in bone morphology and mechanical characteristics of the scapula is increasingly important in planning the best treatment for that patient.

This study aims to develop and use the methods needed to create statistical representations of the shape and mechanical property characteristics of the scapula across a population of patient treated with RTSA. Having this statistical representation will enable future researchers to optimize RTSA design for this population with respect to improving functional outcomes, reducing instances of loosening, and creating technologies that can assist surgeons in planning their surgeries on a patient-specific basis. This will be achieved through the development and use of statistical shape and intensity modeling methods, where intensity refers to the gray scale intensity of voxels, measured in Hounsfield Unit (HU), in Computed Tomography (CT) scans, which are commonly acquired pre-operatively for patients treated with RTSA. This thesis will specifically focus on creating statistical models for a population of patients that exhibit erosion of the bone that forms the glenoid fossa as these patients continue to have inferior results compared to patients treated with RTSA that do not have glenoid erosion. It was decided to include patients with various types of erosions including both Walch-type erosions classified as B2 and B3, and Favard-type erosions classified as E1 and E2 to ensure the registration method would work with both. However, in the future, it is likely that further statistical models will be created that disaggregate the inputs based on their specific erosion-type.

The objectives of this thesis are as follows:

1. Generate 3D shapes from scapula CT images of RTSA patients with glenoid erosion using segmentation methods.
2. Develop a correspondence maintaining registration algorithm to create a point cloud-based dataset based on our patient scans.
3. Develop a statistical description of scapula morphology to quantify variation across the population.
4. Develop a statistical description of material property distribution in patients' scapulae associated with their shape morphology to quantify intensity variation across the population.

The first contribution of this research was to use 61 patients' CT scans treated with RTSA and perform image segmentation on 2D images for generating 3D scapula models. The second contribution was to study eroded scapula models rather than healthy scapulae which makes this study significantly challenging due to various types of bone erosion in the different patients' scapulae. The third contribution was to implement a registration algorithm from the literature for the complex geometry of the scapula. The fourth contribution was to develop a statistical shape model from 61 patients' scapulae in order to quantitatively study bone morphology. The fifth contribution was to develop a statistical intensity model to quantitatively study bone property distribution throughout the group of RTSA patients.

1.5 Thesis outline

This thesis is structured as follows:

Chapter 0 is a literature review on three major topics including shoulder anatomy, glenoid erosion, and shoulder arthroplasty. The objective of this chapter is to introduce relevant anatomical terminologies on shoulder complex and explain common techniques in shoulder joint replacement surgeries along with the biomechanical aspects of RTSA.

Chapter 2 describes the data acquisition methods used in this study. A brief explanation along with visual illustrations are provided for the segmentation process and point cloud generation.

Chapter 3 discusses the concept of registration methods, as well as common rigid and non-rigid registration techniques. Subsequently, a non-rigid registration algorithm is adapted from the literature to work with a set of scapulae with complex erosions and at the end of this chapter, the algorithm is evaluated with respect to its geometric fitting and correspondence accuracies.

In Chapter 4, the statistical shape modeling method is presented by explaining the mathematical approach of principal component analysis to construct a scapular SSM and identify the main modes of shape variation across the population.

Chapter 5 presents the results of SSM along with evaluation methods used to assess the performance of SSM. The SSM results are evaluated through three standard metrics of compactness, generalization ability and specificity to assess the quality of constructed models. In addition, anatomical measurements on scapula models and SSM results are discussed along with relevant terminologies and required descriptions on landmark selection.

Chapter 6 demonstrates the steps taken toward developing the statistical intensity models to find the intensity variations in our population of patients. These steps include the volume mesh generation, mesh morphing process and material property assignment procedure. At the end of this chapter, SIM results on the dataset are presented along with result discussion.

Chapter 7 concludes this work by providing a brief summary of SSM and SIM studies along with future works and research directions. This chapter provides an overview of the findings and results in this study considering the goals previously described in the thesis objectives.

Finally, supplementary information is presented in the Appendix A and B after the list of references.

Chapter 2
Data preparation

In this chapter, the data preparation aspects of this project will be explained from the initial steps of image processing to the final step of dataset formation. Therefore, in the following sections, medical image segmentation and relevant information required for data processing will be presented along with the step-by-step procedure of image segmentation which we used to generate our 3D dataset for this study.

2.1 Medical image technologies

Development of medical imaging technologies allows scientists and researchers to access valuable information of internal organs of human body. The medical imaging is not only a way to visualize the anatomical structures for disease diagnosis and therapeutic purposes but also a powerful tool for surgical planning, motion tracking in robotic surgeries and simulation in many clinical applications [44], [45].

2.2 Data comprehension

The development of imaging technologies has had a great impact on improving the clinical analysis and medical diagnoses. These technologies can provide valuable data to visualize and describe skeletal anatomy.

SSM is a powerful technique to study the anatomical shapes and produce a compact representation of shapes. The initial step in SSM is to prepare a dataset, which is a collection of instances of the shape of interest. These instances can be 2D or 3D structures depending on the application. In this project, as discussed in previous chapter, our application is the investigation of the anatomical shape of the scapula (shoulder blade). In order to build an SSM, we need to have access to a large set of shape instances that represent the variation in the population of interest (e.g. patients with Favard-type E and Walch-type B erosion). Medical imaging technologies can help us to accurately capture the bone geometry. The most relevant imaging modality for capturing bone geometry is Computed Tomography (CT) scanning. It refers to a computerized x-ray imaging procedure in multiple planar x-ray projections are taken from different angles around a patient and are reconstructed into a 2D image representing the material composition within the plane of the projections. This process is repeated for multiple projection planes (i.e. ‘slices’) to create a stack of images that represent the 3D anatomy [45].

The second step is creating 3D shapes from each patient’s scan. There are many medical image processing software available for this purpose such as Mimics (Materialise, Leuven, Belgium) which is a 3D image-based engineering software [46]. In this project, the imaging datasets are collected using CT scan images. These images capture the right or left shoulder blade of patients who are suffering from osteoarthritis (OA) and are treated by Reverse Total Shoulder Arthroplasty (RTSA).

2.3 Demographic data

A series of imaging datasets of patients with eroded scapulae (N = 61) was used for this study. The CT images were obtained in an anonymized form (University of Victoria Ethics approval # 18-217) from Dr. George Athwal, MD, FRCSC at the Hand and Upper Limb Centre (London, ON). These CT images were captured by a GE Lightspeed CT scanner (General Electric Healthcare, Waukesha, WI, USA) and scan parameters are provided in Table 5.

Table 5. Scan parameters used for CT imaging by GE Lightspeed CT scanner.

Beam energy	120 KV_p
Slice thickness	1.25 mm
Pixel spacing (Resolution)	0.5 x 0.5 mm
Total pixels (Matrix size)	512 x 512
Convolution kernel[1]	BonePlus [47]
Tube current	Auto-adjusted to patient

The study population was drawn from the Canadian population, specifically of patients treated with RTSA. Demographic information including age and sex are provided in detail for all patients in Table 6 and divided in terms of their glenoid erosions in Table 7.

[1] Note: It is a matrix used for blurring, sharpening, embossing, edge detection, etc. in image processing.

Table 6. The demographic data of all scapulae in the dataset.

Sex	Quantity	Age
Female	31	73.6 ± 6.76
Male	28	67.9 ± 8.68
All	61	70.9 ± 8.2

Table 7. The demographic data based on the glenoid erosion type.

Sex	Favard-Type E		Walch-Type B	
	Quantity	Age	Quantity	Age
Female	12	77.5 ± 4.2	19	71.2 ± 6.9
Male	9	71.4 ± 8.2	19	66.2 ± 8.4
All	21	74.9 ± 6.9	38[2]	68.7 ± 8.1

2.4 Mimics software

There are a variety of platforms and software available for scientists and industries for 3D reconstruction of medical images [48], [49]. Each one has its own strengths and weaknesses that vary by their functionality, accessibility, accuracy, and ability to read different types of medical images. For this study, Materialise Mimics software has been chosen to convert our raw data from DICOM images to 3D shapes [50]. DICOM stands for Digital Imaging and Communications in Medicine, which is used globally to store, exchange, and transmit medical images [51]. DICOM data from CT or MRI images can be uploaded into Materialise Mimics to be viewed, segmented, edited and reconstructed into 3D shapes.

The following section will explain how Mimics can facilitate and accelerate the surface reconstruction and segmentation of anatomical structures using one example of upper body CT images which is shown in Figure 17.

[2] Note: demographic information for two sets of CT scans were not available.

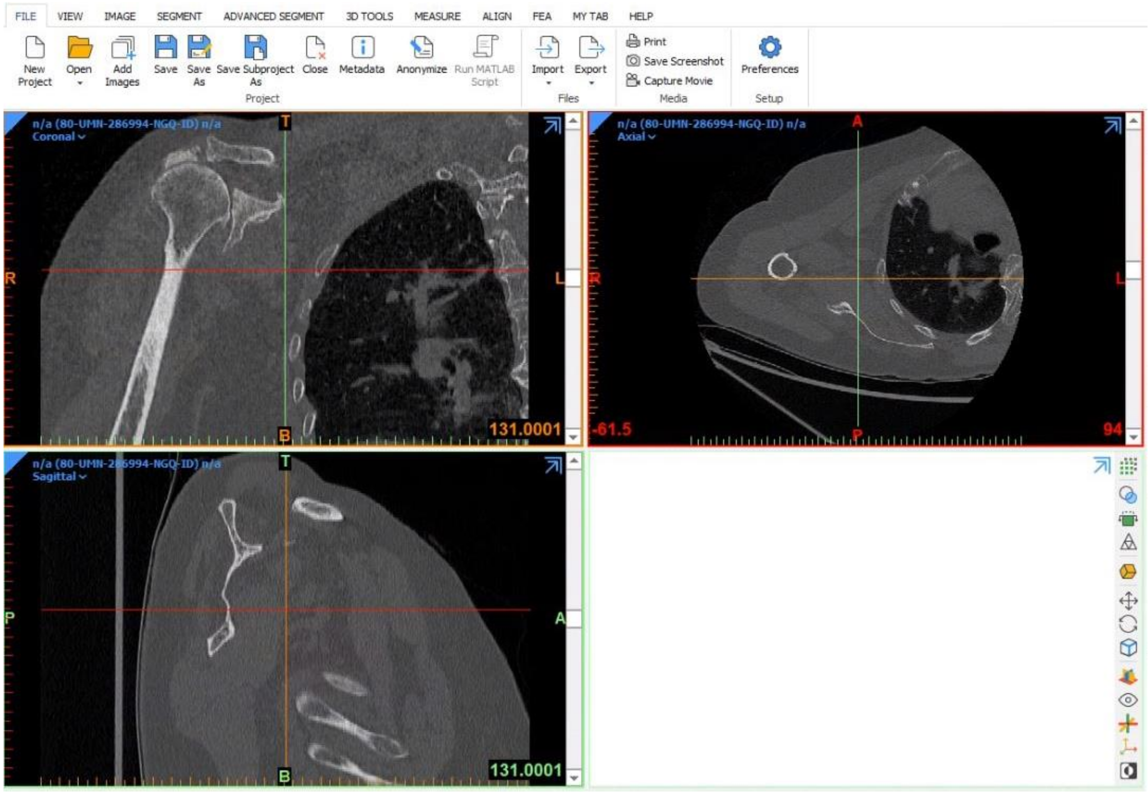

Figure 17. Illustration of Materialise Mimics workplace displaying an upper body CT scan in three planes (Coronal: top left, axial: top right, and sagittal: bottom left).

2.5 Segmentation process

Segmentation is the process of identifying and marking the regions of interest in each 2D image within a stack of 3D images that make up a CT scan (e.g. identifying the portions that correspond to a bone of interest). This is the first step in pre-processing of an image set which can be performed in Mimics. In this study, each scapula in the dataset was segmented from the remainder of the shoulder anatomy presented in the 2D scans using the Mimics software's features in order to allow reconstruction of a 3D model that accurately represents its geometry. In Mimics, segmentation masks are created using tools consisting of thresholding, region growing, mask splitting, and mask editing. Steps taken to produce 3D models from the image set are outlined below:

- **Thresholding:** The majority of the bone of interest can be separated from the remainder of the image using thresholding feature. Thresholding is the first action performed to create a segmentation mask and effectively splits the image into regions whose voxels either do or do not fall within a specified intensity range measured in Hounsfield Unit (HU). There are predefined HU threshold settings for certain biological materials such as bone which has a relatively high and well-defined intensity range as shown in Figure 18.

- **Region growing:** Because thresholding is purely based on voxel intensity, it does not differentiate between regions that represent different anatomical features that are unrelated such as two different bones. Thus, after thresholding, it is often necessary to differentiate between portions of the thresholding generated mask that represent unrelated regions due to the existence of contiguous voxels between regions. An example of contiguous voxels between the scapula and humerus on a selected slice is shown in Figure 19. Region Growing enables this by taking a user specified seed point within the existing mask (i.e. a voxel that the user clicks) and growing a region outward by adding voxels from the existing mask to a new mask until it encounters voxels that are not contained within the existing mask. In this way it is possible to semi-autonomously create a mask that contains only voxels that are contiguous and for the most part related to the same bone of interest. The result is shown in Figure 20.
- **Mask splitting:** To further segment different parts of a mask, Mimics provides a Split Mask tool that allows the user to easily select two parts of a mask and split them into two separate regions. An example is splitting a mask that contains both the humerus and scapula, which have voxels that are contiguous, into two separate masks as shown in Figure 21.
- **Mask editing:** This feature enables user to draw, erase, or locally threshold a specific mask, which may not have been correctly captured using the previous automatic segmentation steps.

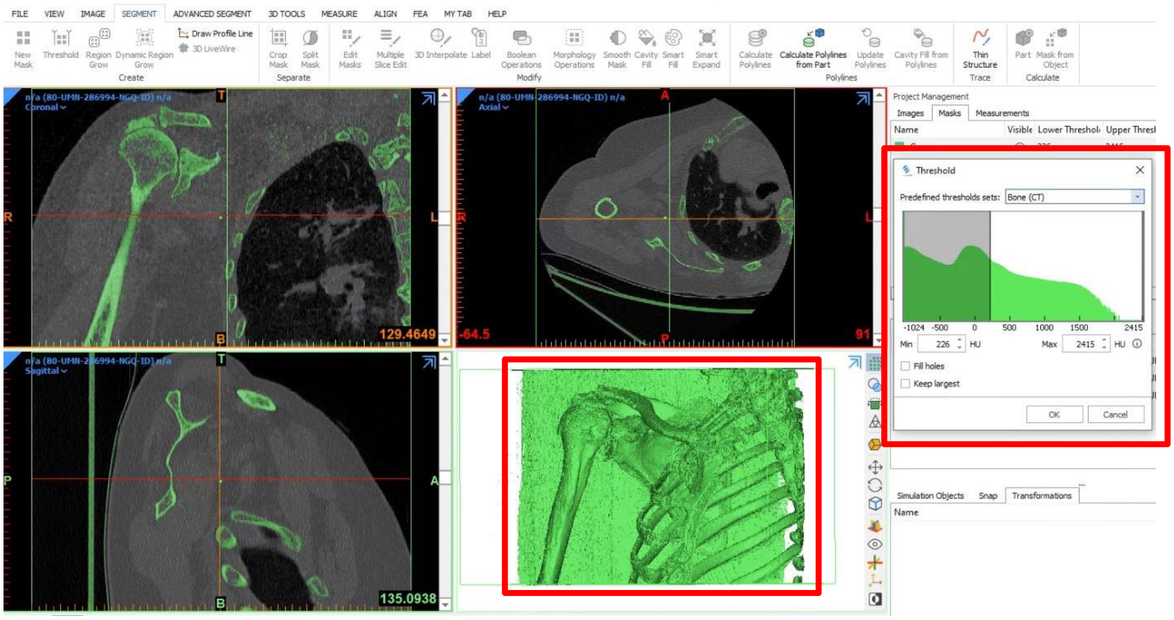

Figure 18. Thresholding step of image segmentation in Mimics software with 2D images showing all material that has an intensity within the range corresponding to bone having been added to the green mask. 3D preview model (shown in left red rectangle) of all material with intensity within predefined threshold (shown in right red rectangle) including bones and scanner bed.

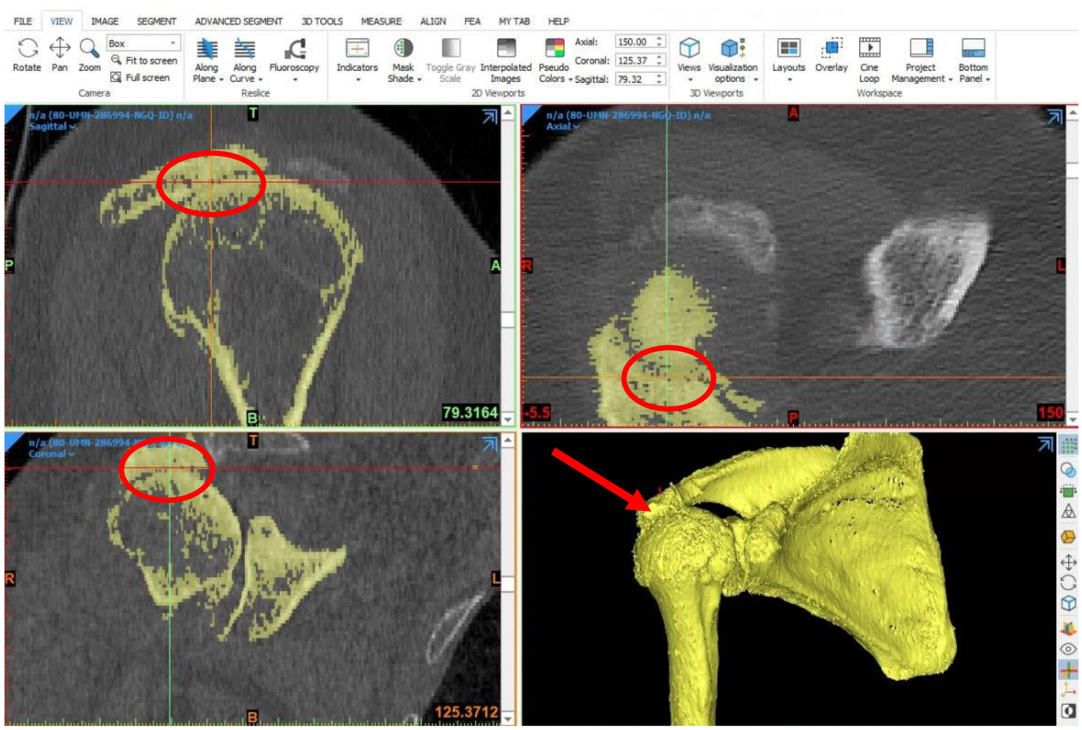

Figure 19. Illustration of contiguous voxels between scapula and humerus on a selected slice in Mimics software.

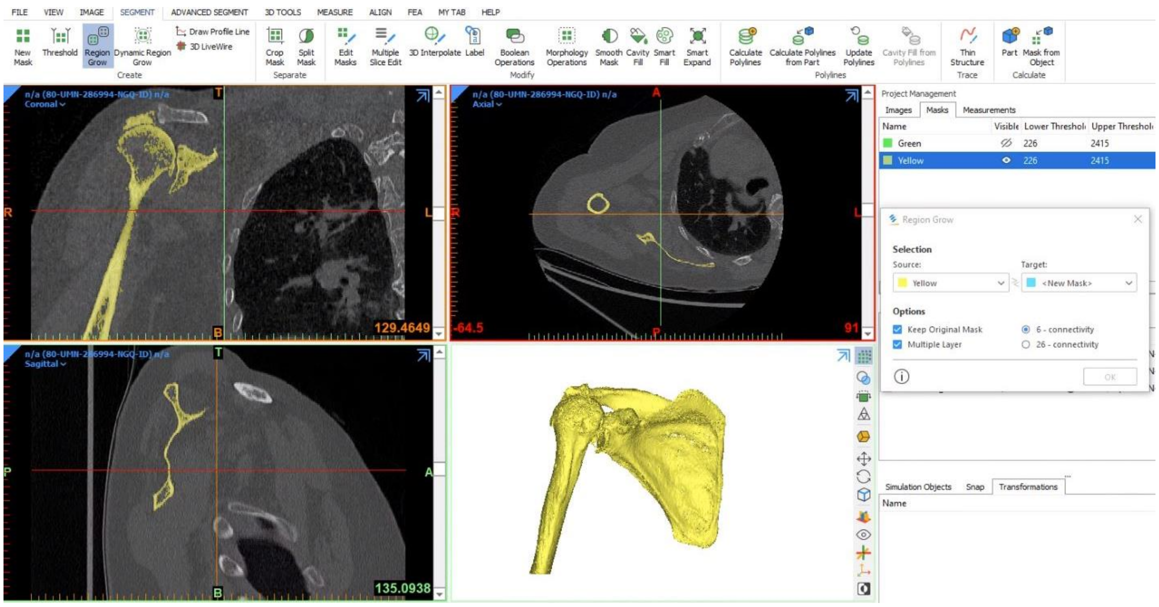

Figure 20. Region growing step of image segmentation in Mimics software showing how the selection of a seed point on the scapula has yielded a yellow mask that has remove most of the material not related to the scapula with the exception of the humerus which has remained in the mask because it had voxels in the green mask that were contiguous with the scapula voxels. (3D preview model of shoulder bones: bottom right).

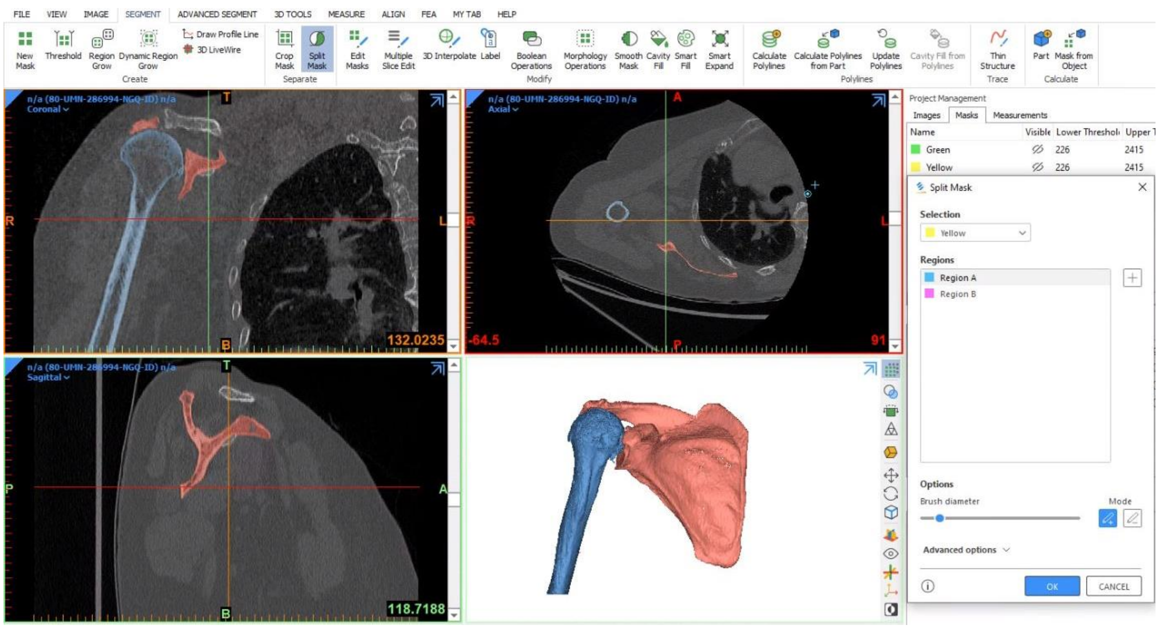

Figure 21. Illustration of the result of splitting the yellow mask into separate humerus (blue) and scapula (red) masks (3D preview model of separate scapula from humerus: bottom right).

2.6 3D model reconstruction

After completing the segmentation process and ensuring the scapula is properly captured in each slice, the stack of segmented 2D masks can be reconstructed into a 3D geometric model (see Figure 22) using the Calculate Part tool. Once the 3D parts are created, they may still have holes or defects on their surfaces which need to be removed and refined. These defects are mainly a result of the original 2D images that were used to generate the model. The quality of the 3D models that Mimics can create, directly correlates to the slice thickness and pixel size of the 2D images. The smaller the slice thickness and pixel size, the higher the quality of 3D parts. Reductions of slice thickness and pixel size require a corresponding increase in patient x-ray exposure and thus to limit exposure, these two parameters are usually kept to moderate values of 1.25mm and 0.5mm, respectively. This in combination of parameters can result in 3D reconstructions with unwanted artifacts.

Therefore, Mimics has provided 3D tools including Smooth and Wrap options to remove large defects and fill in holes that were generated during the previous steps, which is shown in Figure 22. An example of the result of smoothing and wrapping of one scapula model is shown in Figure 23. This feature ensures accurate 3D shape formation and results are not deflected by poor image quality or abnormal bone growths [52].

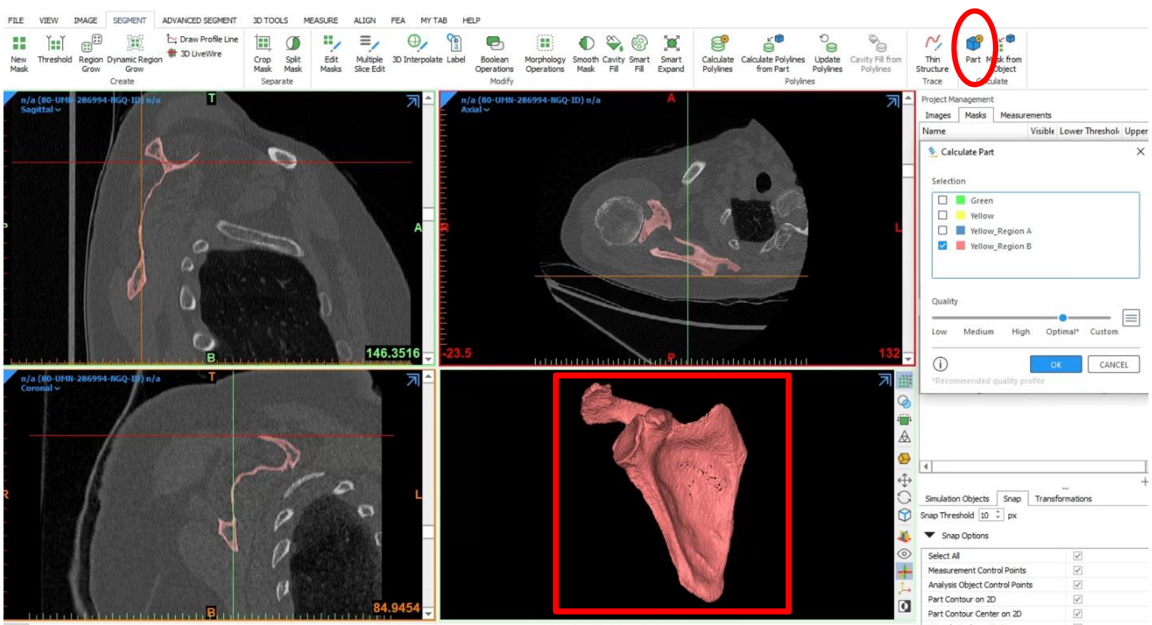

Figure 22. Illustration of initial 3D reconstruction of scapula from 2D masks by part calculation tool (shown in red square) before using smooth and wrap features of Mimics software.

Figure 23. *Illustration of final 3D model of scapula after using 3D tools (smooth and wrap features) on initial 3D reconstructed scapula shown in previous figure in Mimics software.*

Depending on the type of output file needed, Mimics can export 3D models into various formats including exporting in the STL format which will be discussed in section 2.7.

2.7 STL file

STL is a file format created by 3D Systems which is used in rapid prototyping, 3D printing and Computer Aided Design (CAD) software [53], [54]. It is an abbreviation of the word Stereolithography, although it also refers to "Standard Triangle Language". An STL file stores information about 3D geometry and describes only the surface geometry of a 3D object without any representation of internal structure. An STL file is a triangulated surface mesh file composed of a series of nodes. The file contains the three nodes for each triangle and defines the normal direction of the triangle. This file format is ideal for anatomical geometry because of its simplicity in file structure and flexibility to match with any contour desired.

In this study, we have exported our 3D models created from CT scans in Mimics software into STL file format to be used in future investigations. Since in SSM we are only interested in studying bone geometric morphology, a surface mesh representation is sufficient.

2.8 3-matic software

Materialise’s software suite also includes 3-matic, a software that combines CAD tools with pre-processing and meshing capabilities [55]. Once the 3D model is created in Mimics, it is often necessary to perform mesh editing, remeshing, or volumetric mesh generation from the surface mesh. To achieve this, the STL file can be transfered from Mimics to 3-matic. In this project, surface meshes are created to be used in SSM and represent the scapula morphology. In order to have better observation and further access to small details of scapula geometry, it is recommended to use a dense and uniform mesh structure for the 3D models due to the complex and thin shape of scapula. 3-matic’s provides the tools and control needed to modify the exported non-uniform mesh from Mimics, which can be seen in Figure 24, into a uniform and more dense mesh, which is shown in Figure 25.

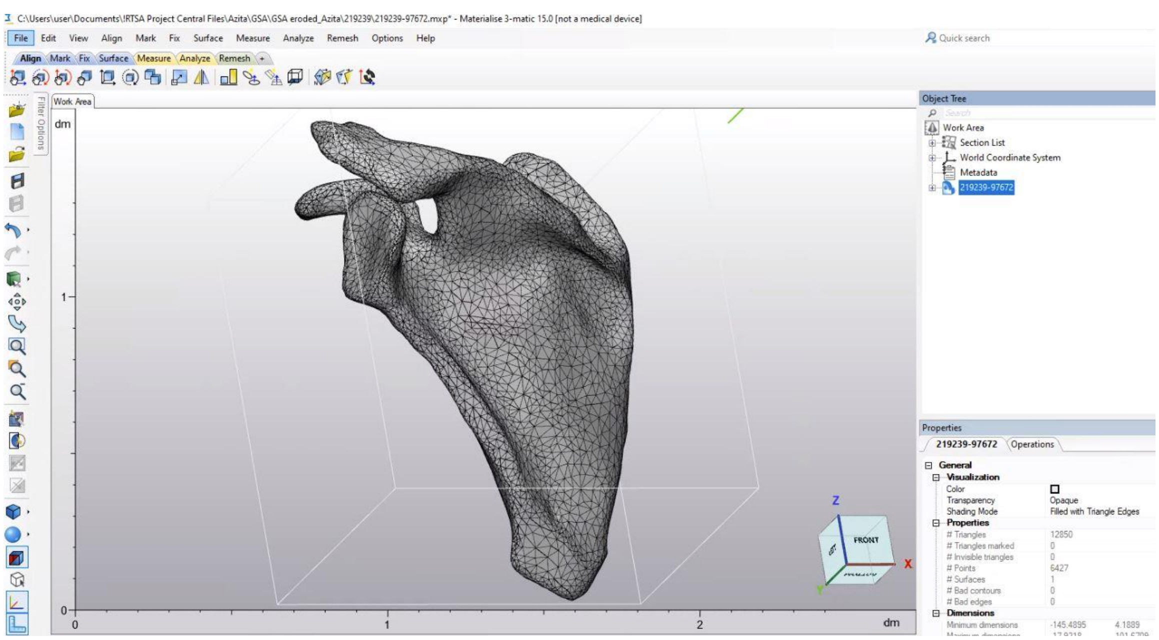

Figure 24. Illustration of 3-matic workplace with a non-uniform and low density surface mesh.

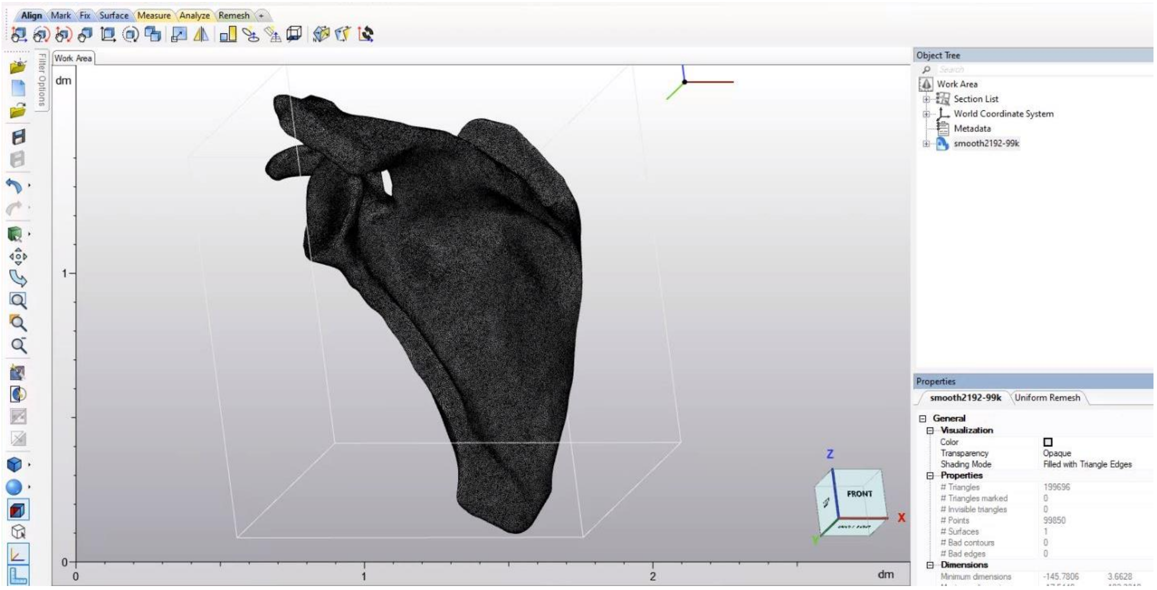

Figure 25. Final surface mesh with uniform and density triangulation.

Triangular surface meshes were generated with an average triangular mesh element size of 0.6 mm, which is the average edge length of the surface mesh triangles. This number was selected based on the thickness measurement of thin scapula body and borders. It enables the accurate representation of the various irregular structures of the scapula. This remeshing process resulted in surface meshes with an average of 106k nodes for each scapula model. The mesh information is presented in Table 8.

Table 8. Surface mesh information of all 61 scapulae

Number of mesh nodes (k)	Number of mesh faces (k)	Mesh edge length (mm)
106.7 ± 43.3	219.8 ± 56.7	0.64 ± 0.09

It should be noted that the dataset is made of 35 right shoulders and 26 left shoulders. Right-side scapulae were mirrored to be left-sided in the 3-matic software to simplify the registration process in the next steps. A scapula that was visually determined from normal and healthy dataset to not have any sign of trauma or erosion was selected as the Atlas to be used as our source model for the registration process. It was formed by 119k nodes with an average edge length of 0.6 mm. It is recommended to choose the source model to be near the median size of scapula as reported in the literature [56]. A scapula near the median size and shape was chosen as it makes the registration process less challenging because it can be morphed to match the most extreme samples with less significant deformation than if a non-median case was selected. In addition, generating a volume mesh from a surface mesh can be performed in the 3-matic software and is generally used to create Finite Element Analysis (FEA) models. However, we used this feature for the first step of the SIM portion of this research in order to transform the triangulated surface mesh to a tetrahedral volumetric mesh that can represent the internal material property variations of the scapula.

Chapter 3

Registration

The fundamental requirement for creating an accurate SSM is a set of objects described using 3D point clouds with the same number of points where each numerated point is positioned in the same anatomical location for each bone, (i.e., points correspond to one another in each model). To achieve this requirement, a Registration method that preserves the needed anatomical correspondence is used. This chapter discusses the registration process and its applications along with common methodologies in this area and the proposed registration process will be presented at the end.

3.1 Surface registration

Registration can be used on different datasets such as signals, images, surfaces, etc. This topic is one of the most important and challenging areas in machine vision and image processing [57], [58]. In studying the variation of shape, the registration in this work is only concerned with registering the surfaces of the various scapulae to a common reference (i.e. the source or atlas model).

Surface registration is a transformation process, which deals with 3D datasets that can be point clouds, mesh structures or sparse 3D point data. Surface registration is a frequently used technique in many applications, such as surface recognition, or surface reconstruction [59], [60]. Surface registration is used to transform datasets captured in different coordinate systems into a common reference frame, which results in alignment. These datasets represent the surface of 3D objects in the form of point-based features. These 3D surfaces are generally obtained from a 3D scanning process like laser scanning or imaging technologies such as X-ray, Ultrasound etc. Due to their varying methodologies these 3D scanning or imaging technologies capture their datasets in variable reference frames. To be able to easily relate and compare different 3D objects, it is necessary to first align them using a registration method [61].

Surface registration is a fundamental element in computer vision, reverse engineering, augmented reality, pattern recognition, motion tracking and even healthcare. In healthcare applications, registration can be used in cancer tissue or small hole detections, artefact recognition [62], [63]. In other fields like computer vision, it can be used in spatially matching multiple views of an object in order to make a complete model of that object. In addition, it can be useful in position tracking in the field of robotics. For example, tracking the position of a sensor when it moves from one point to another by matching different views taken at different times [64]. Other applications can be finding object correspondences in big datasets and reassembling missing or fractured parts [61].

Registration algorithms can be broadly classified in two ways 1) rigid or non-rigid (NR), which differentiates those that are limited to transforming an object as a whole without changing its shape and those that can stretch, shrink, warp, etc. an object; 2) coarse and fine, which relates to the quality of registration. More specifically, these classifications can be defined as follows:

1. Rigid registration is one of the simplest methods in the category of linear transformation models. A rigid approach can register objects which are related by rotation and translation. In rigid methods, homogeneous transformations can be modelled using only 6 degrees of freedom (DOF) – 3 translations and 3 rotations. Whereas Non-Rigid methods can be applied on articulated objects or deformable models while using more than 6 DOF in their modelling [63] to enable the a registered object to locally change in shape and scale in addition to its overall pose defined by translation and rotation.
2. Coarse registration methods perform an initial geometric alignment that results in two objects being roughly aligned but not optimally so, whereas fine registration methods apply a transformation that optimally minimizes the error between a cloud of points on two models. Therefore, it is recommended to use coarse registration firstly and then fine registration to achieve best results. Also, combination of coarse and fine registration algorithms can be performed to reduce the total number of iterations to get an optimal alignment between point clouds [65].

3.2 Rigid registration

The main purpose of all rigid registration algorithms is to find a transformation method that best aligns all the point clouds of our dataset into a common coordinate system using the same translation and rotation for all points in the registered model (i.e. the relative relationships between the model's points does not change from before to after registration). Most of the existing algorithms in the literature employ three popular methods for registration [66], based on:

1. Principal Component Analysis (PCA)
2. Singular Value Decomposition (SVD)
3. Iterative Closest Point (ICP) algorithm

How to choose one of the aforementioned algorithms depends on various characteristics like computational complexity, accuracy, running time, rate of convergence and mostly on the type of data used and its environment. Each method tries to estimate the optimal rigid transformation in order to map a source point cloud on a target point cloud. In the next paragraphs, these three methods will be discussed and compared with each other in detail.

Each registration algorithm can be defined as a cost function that represents the matching error or distance between corresponding points in each 3D point cloud. This cost function can be minimized by any optimization techniques like least-squares minimization, homogeneous transformation, etc.

3.2.1 PCA-based methods

PCA is commonly used method to reduce the dimensionality of large datasets, by transforming a large set of variables into a smaller one while preserving information as much as possible. One of the applications of PCA is in compression and classification of datasets into an orthonormal basis in the direction of the largest variance, which corresponds to the largest eigenvector of the covariance matrix of the dataset. Also, the magnitude of this variance can be calculated by the corresponding eigenvalue. For registration purposes, PCA can be used to align two different point clouds when their covariance matrices differ from the identity matrix. It can be obtained by simply aligning the eigenvectors of their covariance matrices utilizing the following steps:

1. The center of one point cloud should coincide with the center of the other point cloud. It should be noted that the centroid of each point cloud can be determined by dividing the sum of all point coordinates by the total number of points in each point cloud which corresponds to the average coordinate of all points. Once the center of each point cloud is identified, point cloud centering can be calculated by simply subtracting the centroid coordinates from each of the point cloud coordinates.
2. The next step is to find the direction of the largest variance, which is required for alignment. Therefore, the covariance matrix of each point cloud should be determined. It is an orthogonal matrix, and the diagonal values represent the variances while the off-diagonal values represent the covariance.
3. Then, the eigenvector with the largest eigenvalue should be identified which is a vector in the direction of the largest variance representing the point cloud's orientation.
4. Once the eigenvectors are determined for each point cloud, rigid registration can be obtained by aligning these vectors by defining a transformation matrix for each point cloud. Each matrix aligns its corresponding point cloud with one main axis like X or Y-axis in 2D datasets.
5. Finally, the centroid of each point should be transformed to the proper coordinate. If we are aligning one point cloud to another, the centroid of one of them needs to be translated to the other one using the translation vector in the transformation matrix [67].

A mathematical description of the PCA method is more thoroughly discussed in section 4.4.

3.2.2 SVD based methods

In the previous method, PCA aligns two point clouds using the direction of their largest variances without minimizing the Euclidean distance between corresponding points. Accordingly, this method is sensitive to outliers and performs best when points are normally distributed otherwise it is required to directly minimize the Euclidean distances between two point clouds. However the SVD approach is only available when the total number of points in each point cloud is identical. This is a linear least squares problem that can be easily solved using SVD approach. One of the pioneers in the least square fitting of two 3D point sets is Arun et al. at 1987 [68]. They presented an SVD based algorithm, which decomposes the covariance matrix K as USV^T. The right singular vector U contains the eigenvectors and the squared diagonal matrix S contain the eigenvalues. When the eigenvalue decomposition is obtained, the cross-correlation matrix K between the two centered point clouds which is shown in Eq. (1) can be determined as follows:

$$K = USV^T \tag{1}$$

Then the optimal solution is to find a rotation matrix R and translation matrix T in order to minimize the distance between two point clouds, which are shown in Eq. (2) and (3):

$$R = UV^T \tag{2}$$

And

$$T = P_{c1} - RP_{c2} \tag{3}$$

Where P_{c1} and P_{c2} are the two centered point clouds [69].

3.2.3 ICP Algorithm

Whereas the SVD method directly solves the least squares problem, another approach which iteratively disregards outliers is presented that can improve the aforementioned estimation to find the rotation and translation matrices and it is called Iterative Closest Point (ICP) algorithm. ICP is one of the best-known point cloud registration algorithms which is widely used in geometric matching problems. This algorithm firstly was proposed by Besl et al. at 1991 [70] and soon after became the most dominant method for point cloud registration. The alignment process of two point clouds starts with an initial guess of rigid transformation and continues with refining that by generating pairs of corresponding points and minimizing their distance iteratively. The initial guess can be made by various ways like structural indexing, computing the principal axes of point clouds, user input data, landmark points selection, or exhaustive search of all possible solutions [71].

Although the ICP method is easy to implement in registration algorithms, it is not always efficient and has the disadvantages of large computational expense, which may not even converge to the global optimal solution. Due to the practical difficulty of the ICP algorithm in heavy computations, many researchers have worked to improve the performance of ICP methods and proposed different approaches like point-to-point ICP [72], point-to-line ICP [73], point-to-surface ICP [74], generalized ICP [75] and etc. These methods sometimes are not able to converge, however the speed is significantly improved in comparison to the traditional ICP.

The basic concept of the ICP algorithm to transform two point clouds of P1 and P2 is presented in a pseudocode below where *R*, *T*, *X* and *E* are the rotation, translation, transformation matrices and error value to stop the algorithm execution.

ICP (P_1, P_2){

Compute (Center of mass for P_1, P_2)

Translate (Center of mass of P_1 to P_2)

While (Distance (P_1, P_2)> E_{max} {

Transformation matrix X = min E(X) = min $\frac{1}{N}\sum_i \|P_2 - RP_1 - T\|^2$

P_1=Transform point cloud (P_1, X)}

Final transformed P_1}

Figure 26. Illustration of pseudocode for basic ICP algorithm.

3.3 Non-rigid registration

Surface registration becomes challenging when it comes to deformable objects. Non-rigidly deforming one shape into alignment with another shape requires a non-rigid registration algorithm. Such methods need to find an optimal set of local and global transformations that achieve optimal alignment and this results in a large number of degrees of freedom.

Every registration process employs the optimal transformation to maximize the agreement between the objects, which involves four main components:

- **A transformation model**: this describes the geometric transformation between the source model to be morphed to the target shape. It determines which type and number of transformations (i.e., rigid, or affine transformation) are needed. In which, affine deformation involves scaling and shear in addition to translation and rotation in the rigid deformation.
- **A similarity metric:** this specifies the registration basis which measures how well two shapes are matched. One example is calculating the distances between corresponding features to measure the alignment.
- **An optimization method:** this tries to optimize the transformation parameters to maximize the similarity measurements.
- **A validation protocol:** this would assess the performance and quality of the registration process in terms of accuracy and robustness [57].

Many problems and constraints have been reported in the process of point clouds registration such as uneven point numbers, large point clouds, repetitive data, incomplete point cloud structures, and limited overlaps between points, etc. To overcome these challenges, many studies have investigated different transformation approaches to increase the accuracy and improve the efficiency of registration algorithms. There are many studies that investigated the transformation model selection and proposed different approaches regarding their case study and its application. Some of them utilize a piecewise transformation model with a combination of local and global deformations based on the object features. Allen et al.'s approach used markers and placing them on the object which can help to reconstruct the body posture for deformation modeling [76]. Unlike Allen's method, Pekelny et al. proposed a markerless approach using predefined object information to find and track transformations [77]. These feature-based techniques have correspondence and feature selection problems since there might be some features in one set which do not exist in the others. Therefore, Chui et al. developed a framework using the thin-plate spline as the non-rigid transformation model for the spatial mapping [78].

Myronenko et al. developed a probabilistic registration algorithm that assumes the alignment of two objects as a probability density estimation problem. It regularizes the displacement field by fitting the Gaussian Mixture Model (GMM) centroids as one point cloud to the other point clouds. At the optimum likelihood, alignment and correspondence are achieved because they force GMM centroids to morph coherently and maintain the structure of the point clouds [79]. Papazov et al. modeled the transformation as-rigid-as possible by estimating correspondences through a closest-point search while considering the local and global scaling with use of Ordinary Differential Equations (ODE) which avoids repeating large linear system solution within a non-linear optimization problem [80].

Moreover, local affine transformations are frequently used in non-rigid registration [81], [82]. Rouhani et al. defined the transformation model as an integration of local rigid transformations by clustering the source model into small patches that can deform rigidly. Also, the target model is modeled by implicit and flexible interface which allows a coarse-to-fine approach to prevent local minimum [83]. Amberg et al. also use a locally affine transformation but with proposing a stiffness constraint to penalize differences between transformation matrices of neighboring vertices [84].

In our proposed algorithm for this study, we adopted the local affine transformation of Amberg's method. In this approach, each source vertex is assigned an affine transformation that seeks to move it in the direction of the nearest target vertex while minimising changes in the distance between neighbouring source vertices in order to maintain their original relationships. As this algorithm progresses to a solution, it provides flexibility that enables control over the level of mesh regularization through stiffness parameters that initially ensure adjacent transformations are similar to ensure their relative relationships are maintained and progressively loosen regularization to achieve accurate representation of local geometric details.

3.4 Correspondence issue

Most of the computational cost of ICP is a result of calculating the correspondences between datasets. Establishing the correspondence for each point in a cloud of points is known as the Nearest Neighbor (NN) search. At each iteration, a correspondent point must be selected in the reference model for each point in the target model. This is needed in order to calculate the distance error between each pair of points in the two models. The NN search method was first proposed by Cover et al. in 1967 [85]. Many improvements and various techniques have been presented to overcome the computational complexity and reducing the running time and now it is widely used in pattern recognition and data classification [86]. One of the classical solutions to the Nearest Neighbor problem is to use a K-Dimensional (K-D) Tree algorithm. K-D trees are binary trees that provide a data structure for partitioning and organizing multidimensional data by splitting K dimensional space through hyperplanes, which are widely used to speed up the search to find correspondent points [87], [88].

The goal of non-rigid surface registration, which is mentioned earlier, is to deform one surface to match another using a mapping method while maintaining the point to point correspondence of each point on the original undeformed reference model (i.e. to deform the shape of the reference model to match the geometry of the target model while ensuring the points remain on the same geometric feature). Obtaining surface correspondences can be done manually using landmarks on both surfaces but this is not a time efficient process and it is susceptible to error. In some methods, mapping between the surfaces is obtained by parameterization to mathematical domains like a sphere or cylinder however, it doesn't work well in complex geometries due the huge difference between their topologies [89].

In addition, Amberg's method uses a stiffness parameter as part of the technique that imparts a level of stiffness between neighboring source points, which prevents highly localized deformations (i.e. with a high stiffness parameter the non-rigid registration acts similar to a rigid registration and becomes progressively non-rigid as that value decreases). This in effect forces points to move in a relatively parallel direction when the stiffness parameter is high in early registration iterations, which helps to maintain the feature correspondence of each point [84]. In the next section, the optimized algorithm inspired by Amberg's approach is explained.

3.5 Correspondence Preserving NR-ICP Algorithm

As it was mentioned earlier, one of the goals of this research is to create an accurate scapula SSM and to do so it is necessary to have a set of scapulae described as 3D point clouds with the same number of points where each point is positioned in the same anatomical location for each bone (i.e. point-to-point correspondence). To achieve this, a non-rigid registration method is needed to morph one Atlas point cloud (i.e., source point cloud) to the shapes of all other bones (i.e., target point clouds); however, it is more challenging and more difficult to maintain good correspondence in irregular and complex objects like scapula. To overcome this challenge, we have adapted and optimized the non-rigid ICP method described in the literature by Amberg et al. [84].

The registration process is divided into two main parts: a first pre-processing part that involves rigid registration and second a mesh morphing part that is based on non-rigid registration.

In the pre-processing step, the aim is to prepare the source model for the mesh morphing process and then repose (i.e. reposition and reorient) the source surface as closely as possible to the target model using only rigid transformations. Due to the different coordinate systems of the scapula models, the point cloud of each target shape is arbitrarily oriented in space. Therefore, we first need to make the source and target models aligned, because differences in orientation would negatively affect subsequent NR registration.

To achieve this, we used Principal Component Analysis (PCA) to find the main axis of each 3D model. Despite variations in specific geometry, all scapula have the same overall archetypal shape and thus an initial registration can be achieved by aligning the reference and target point clouds' directions of maximum variability (i.e. first principal component), which is parallel to the lateral border of scapula which is shown in second row of Table 9. Therefore, the alignment process uses the first eigenvector to make the two point clouds coarsely aligned.

After that, size differences need be eliminated. In this step, the source model is scaled to the size of the target model. To achieve this scaling, a rigid registration method that includes a homogeneous scaling transformation is required and for this purpose, an existing finite step ICP algorithm based on finite difference methods was selected [90]. Once the preprocessing steps are finished, NR registration is then applied to the source model resulting in it being morphed to the target geometry while maintaining its original feature correspondence. The correspondence optimization is achieved by adjusting the stiffness variable and stopping criteria described by Amberg et al. [84]. To briefly explain these two parameters:

- **Stiffness variable**: this parameter consists of an n×1 matrix that lists a series of stiffness magnitudes in descending order. These stiffness values are applied to the source model's point cloud in combination with the current affine transformation to deform the source toward the target surface while maintaining a given level of regularization dictated by the stiffness value. In each iteration, a smaller stiffness value is used which reduces regularization and thus vertices can transform progressively more independently. By this means, high stiffness numbers help global transformations early in the process whereas low values allow for local deformations later in the solution. The number of elements in stiffness matrix and their magnitudes depend on the shape and size of the objects and can be determined by performing a sensitivity analysis on the target objects.
- **Stopping criteria**: In general, this condition must be reached in order to stop the execution of the algorithm. In this case, it stops the inner loop when the stopping criteria is met which is defined as some threshold of minimal change in the calculated transformation matrices between two consecutive loop iterations. The ideal stopping value would be zero but to avoid infinite loops, a nonzero value needs to be defined.

The registration steps are shown schematically using one of the targets in our dataset as an example with the source model and presented step by step in Table 9.

Table 9. Illustration of registration process on a target sample model using optimized NR-ICP method.

Preprocessing	Source and target arbitrarily orientated and sized.	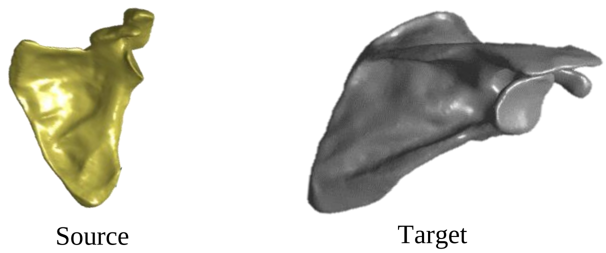
	Source and target aligned in direction of first principal component by PCA.	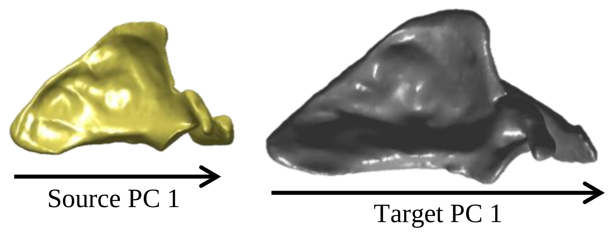
	Source model scaled to the target size without changing Source's shape.	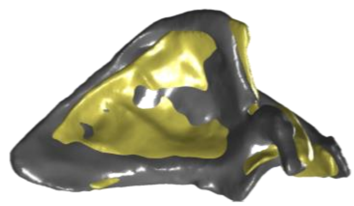
Mesh morphing	Non-rigid registration finished, and source deformed to the target shape by optimized NR-ICP.	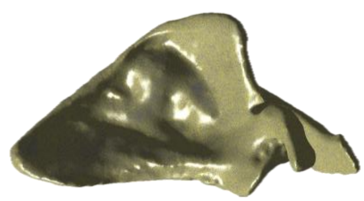

In what follows, by S in Eq. (4) and T in Eq. (5), we denote the source and target surfaces. In our implementation, both S and T are triangulated meshes with different connectivity (Each mesh triangle is made by three nodes and connectivity defines which nodes are included in each triangle). Our algorithm tends to morph the source mesh, S, to get closer to the target mesh, T, and finally end up with a set of meshes for all patient scapulae that have identical connectivity.

$$S = [P_{1,s}, P_{2,S}, P_{3,S} \dots, P_{n,s}]^T \tag{4}$$

S is the list of surface points, $P_{i,S}$, of the source model where n in our study is 119K points that build our source model and each point is a vertex of x, y and z components.

$$T = [P_{1,T}, P_{2,T}, P_{3,T}, \dots, P_{m,T}]^T \quad (5)$$

T is the list of a target's surface points, $P_{j,T}$, where m is not fixed, and it is unique for each target. However, the average number of target points is approximately 106K.

Also, our dataset is a group of target shapes with 61 specimens (i.e. $T_1, T_2, T_3 \; \dots, T_{N=61}$).

The NR-ICP algorithm consists of two main loops:

- **The outer loop**: the source model is made to become progressively closer to the target surface in a specified number of iterations. This loop governs the stiffness constraint defined above and first described by Amberg et al., which is gradually relaxed (e.g. reduced) to enable progressively more localized deformation. Specifically, α, the stiffness weight matrix, is a list of numbers in descending order. By applying α to the stiffness term, we regularized the deformation to start with global deformation and then we successively lower stiffness weights and perform deformations locally. The number of iterations in the outer loop is equal to the number of elements in the stiffness weight matrix. A schematic view of the gradual stiffness relaxation method is shown in Figure 27.

  The choice of the number of iterations depends on the desired accuracy of the results. More iterations will tend to more gradually reduce the stiffness and thus yield improved results on correspondence and geometric fit, but the execution time will increase. Through a sensitivity analysis, the effect of number of outer loop iterations on correspondence accuracy and computational time were determined for the class of shapes to be studied in this work. With a stopping criteria of 0.01 mm the optimal number of iterations was found to be 13 in this application focused on scapula geometry.

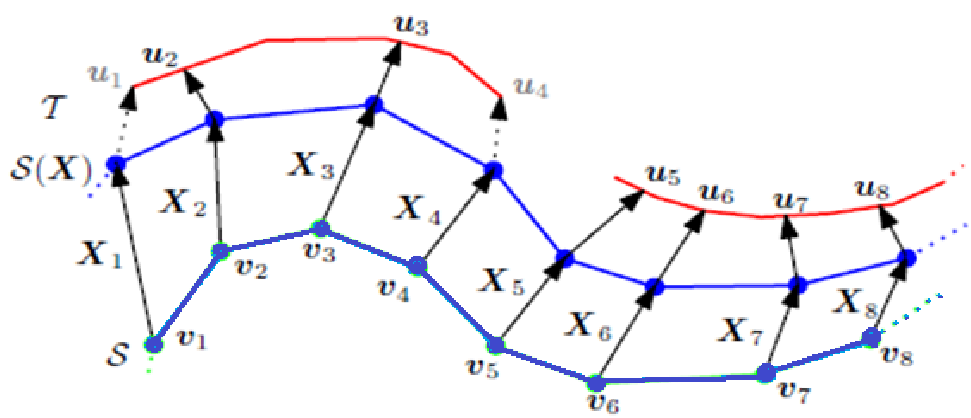

Figure 27. Schematic view of vertex transformation in black in the Amberg's method using stiffness constraint which avoid direct movement of source points in blue toward the target surface in red [84].

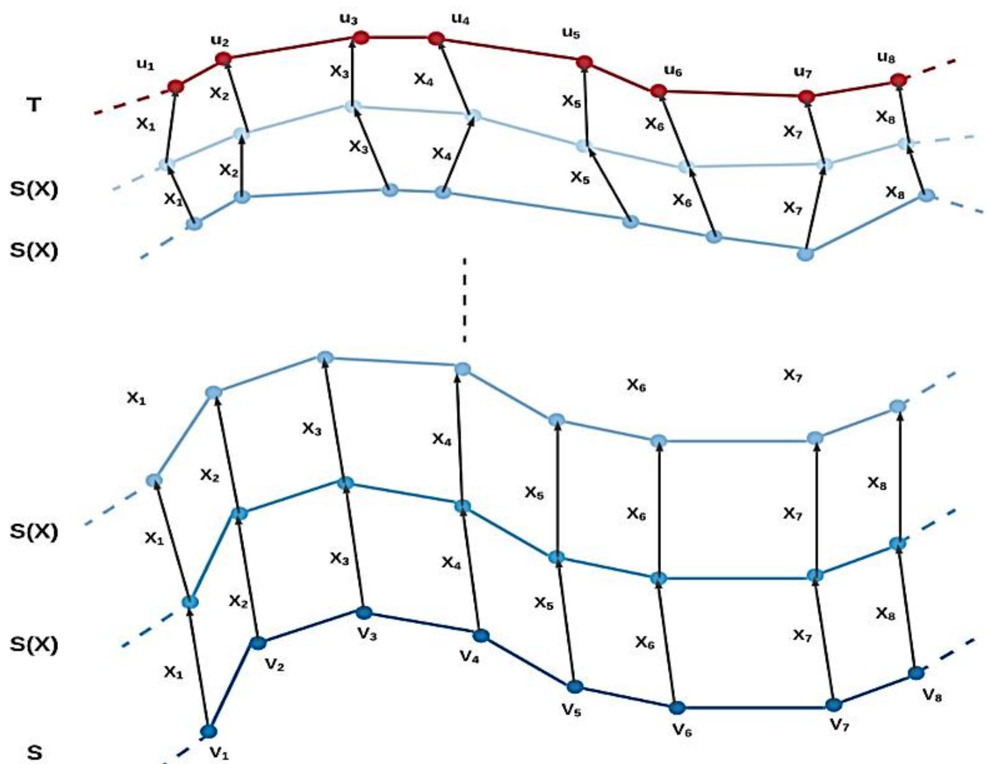

Figure 28. Illustration of relaxation effect on initial steps with higher stiffness values (bottom) where global transformations are in effect and move neighbouring source vertices relatively parallel to each other toward the target and then lower stiffness values (top) that allow local transformation where neighbouring vertices need not move parallel to each other.

- **The inner loop:** this loop finds the optimal deformation for a given and fixed stiffness value, α, in that loop. To find the optimal transformation matrix for each vertex in the source model, preliminary target correspondences are estimated by a nearest neighbor point search method. Then the optimal transformation for the source deformation is calculated by Eq. (13). Due to the stiffness constraint, the source points will not directly move toward the target surface in one step Instead their movement is constrained to cause coherent adjustment of neighbouring points, where the size of the neighbourhood is dictated by the stiffness value. In the next iteration of the outer loop when the stiffness parameter is lowered again, the process continues with new correspondences found by searching from the displaced source points, and this process is repeated until the algorithm converges and meets the stopping criteria.

The purpose of registration is to find an appropriate transformation for each target in our dataset which morph the source to that target shape. We call this transformation matrix X. Each transformation of X for each target shape, is a n×1 matrix which is shown in Eq. (6). Since we try to find transformation matrices to move each point of the source mesh toward the target surface, it results in n number of transformations for each scapula model.

$$X = [X_1, X_2, X_3 \ \dots, X_n]^T \tag{6}$$

Where n is the total number of points in the source model and X_i is the transformation matrix for each point of the source mesh.

A k-dimensional (KD) tree nearest neighbor search function is used to find the nearest point in the target surface. The closest points for each displaced source point P_{Si} is defined as u_i. The distance between corresponding points on the target surface and the deformed source surface must be minimized and the distance function is expressed as E_{dist} and is shown in Eq. (7):

$$E_{dist}(X) = \sum_{i=1}^{n} \| X_i P_{Si} - u_i \|_F{}^2 \tag{7}$$

The distance between a source point, P_{Si}, and its closest point, u_i, on the target surface is defined as $E_{dist}(X)$.

There is a weighting diagonal matrix, of G, which weights differences in the rotational and skew part of the deformation against the translational part and it is represented in Eq. (8):

$$G = [1,1,1,\gamma] \tag{8}$$

Where γ is applied to weight differences in rotation against the translational part of the deformation. The amount of γ depends on the unit and type of deformation in the dataset and γ was set to 1 in this study. To express stiffness in matrix notation, we used the incidence matrix, *M*, which is represented in Eq. (9) for the source points. An incidence matrix shows the relationship between two classes of objects. If they are related, 1 is assigned to that relationship and if they are not related 0. The incidence matrix of source points shows the connectivity of each point to the neighboring points. If an element of *M* is non-zero, it means that the two points corresponding to the row column that define the matrix element are connected to one another.

To write the stiffness term, we must use the Kronecker product. This is a generalization of the outer product and it is used for operation of two matrices with arbitrary size which results in a block matrix. If *A* is an m × n matrix and *M* is a p × q matrix, then the Kronecker product $A \otimes M$ is the pm × qn block matrix. Therefore, the stiffness term in Eq. (10) is written in Frobenius norm form as follows:

$$M = incidence\ matrix\ (S) \tag{9}$$

$$E_{stif}(X) = \| (M \otimes G) X S \|_F{}^2 \tag{10}$$

The Frobenius norm is the matrix norm of an m × n matrix *A* defined in Eq. (11) as the square root of the sum of the absolute squares of its elements.

$$\| A \|_F = \sqrt{\sum_i \sum_j |a_{ij}|^2} \tag{11}$$

The optimal stiffness value depends on the type of surface, or more specifically the number of triangles and the curvature on the surface. The optimal number of iterations also depends on the type of surface and the application. The more similar the surfaces, the fewer iterations are needed for good correspondences and a good geometric fit. For this study, all surfaces are remeshed to 119K vertices, which makes that all surfaces could be registered with the same start and end stiffness value.

The cost function is written in Eq. (12) by the combination of distance term and stiffness term and called as *E(X)*, is as follows:

$$E(X) = E_{dist}(X) + (\alpha \times E_{stif}(X)) \tag{12}$$

$$E(X) = \left\| \begin{matrix} \alpha\,(M \otimes G)X & - & 0 \\ XS & - & U \end{matrix} \right\|_F^{\ 2}$$

$$E(X) = \| AX - B \|_F{}^2$$

Where U is the matrix of closest points of target u_i to source model and α is the stiffness weight and makes the deformation process more and more flexible by incrementally decreasing its value as the source geometry progressively becomes more similar to the target. To minimize E, we set its derivative equal to zero and solve the resulting linear equations. In each iteration of the inner loop, an optimal transformation X for the estimated target correspondences through NN search can be calculated through Eq. (13):

$$X_{optimal} = (A^T A)^{-1} A^T B \tag{13}$$

Once the optimal transformation matrix X is determined for a given iteration of the outer loop (which depends on the geometry at the start of the iteration and the current α stiffness value), we simply apply that X to the source points, which deforms them to have a geometry closer to the target geometry, and then proceed to the next iteration of the outer loop with its incrementally smaller stiffness value, α. This continues until all outer loop iterations are completed, at which point the final version of the deformed source points should closely match the geometry of the target model.

3.6 Evaluation of proposed algorithm

In this section, evaluation methodologies will be discussed in order to assess the quality of the proposed algorithm for non-rigid registration. It is important to evaluate the performance of the registration algorithm in terms of geometric fitting and meaningful correspondences.

3.6.1 Geometric fitting assessment

To assess the quality of the registration method, it is necessary to check how well the source model's surface is mapped to the target models' surfaces, which can be done by quantitative and qualitative analysis on the resulting deformed models.

- **Quantitative analysis**: There are two approaches to check the accuracy of the registration process quantitatively, Root-Mean-Square (RMS) error and Hausdorff distance calculation. RMS measures the pairwise differences of the two datasets and determines how far on average the error is from 0. RMS error is always non-negative, and a value of 0 indicates a perfect fit. Since errors are squared before they are averaged, the RMS gives a relatively high weight to large errors and that's why RMS is useful when large errors are undesirable [91], [92]. In this study, RMS error is used to measure the distance from each point of the deformed source surface to the closest point on the target surface for all models in the dataset.

The Hausdorff distance is the maximum distance from one point in one set to the closest point in the other set. Therefore, Hausdorff distance shows the degree of mismatching between two sets by measuring the distance of one point that is farthest from any point of other set and vice versa [93]. In this study, Hausdorff distance is used to measure the greatest of all the distances from a point in one deformed source surface to the closest point in its target surface of all models in the dataset.

To obtain an accurate geometric fit, the distance between the deformed source surface and the target surface should be minimal. The Root-Mean-Square (RMS) and Hausdorff errors of geometric registration between the original and the deformed models are calculated as 0.25 ± 0.04 mm and 0.76 ± 0.14 mm, respectively. Results of these measurements are shown in Table 10, Figure 29 and Figure 30.

Table 10. Non-rigid registration error represented in RMS and Hausdorff distances on 61 scapula models with ±2 standard deviation.

RMS distance (mm)	**Hausdorff distance (mm)**
0.25 ± 0.04	0.76 ± 0.14

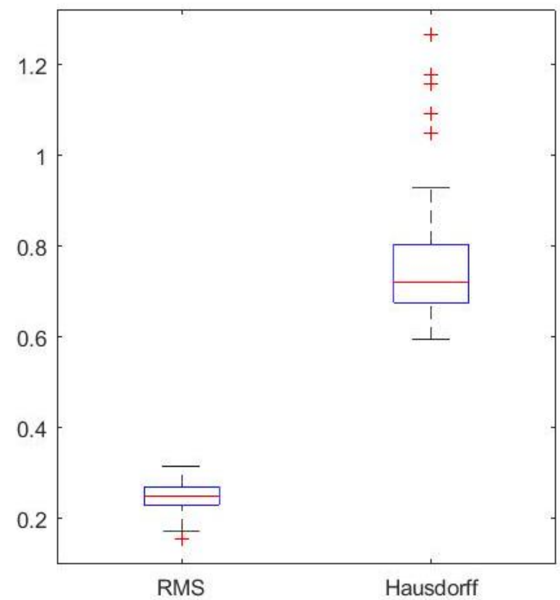

Figure 29. Box chart illustration of RMS and Hausdorff distances of all models in the dataset. Horizontal red lines, red plus signs, horizontal black lines, dash lines and blue rectangle represent median, outliers, min/max, whisker and interquartile range.

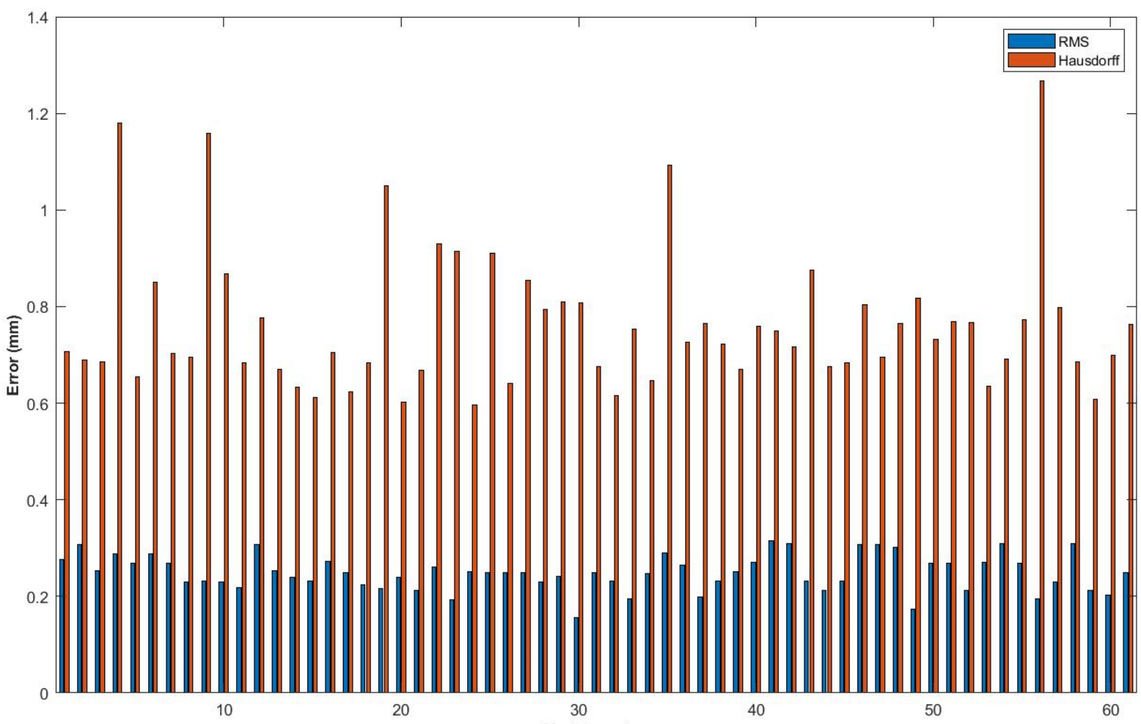

Figure 30. *RMS and Hausdorff distances (Registration error) for each model in dataset.*

It should be noted that the average calculated RMS error of all 61 models (~0.25 mm) of the proposed registration algorithm, is smaller than similar reported study on scapula shape (~0.5 mm) [94].

- **Qualitative analysis:** 3D visualization of the deformed sources along with their target models can be used as a primarily qualitative evaluation in the registration process. A qualitative analysis of one scapula from our dataset is shown in Figure 31.

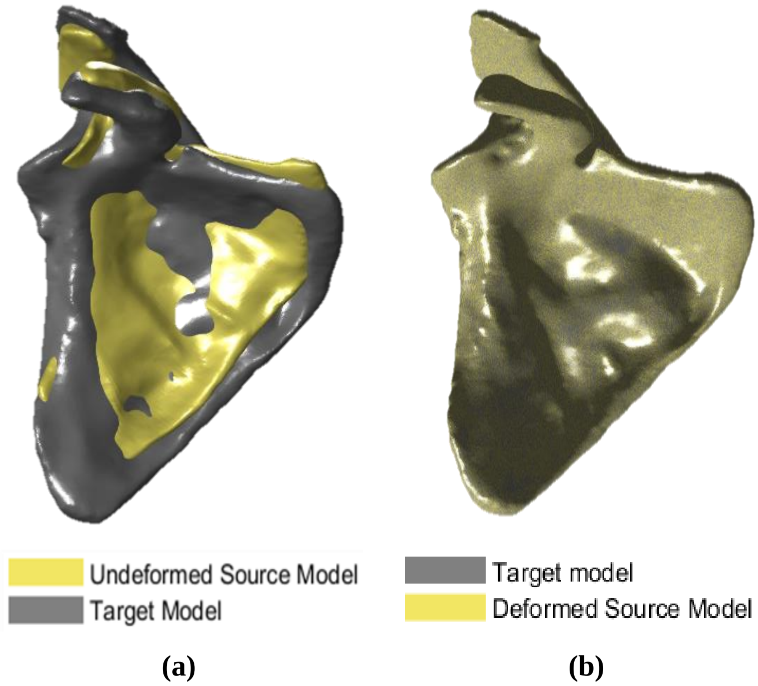

Figure 31. Registration quality is illustrated qualitatively before (a) and after (b) the non-rigid registration process on one sample.

Moreover, the results of quantitative analysis can be demonstrated in a heat map diagram to show the registration errors in different regions presented in Figure 32. In this diagram, RMS error of each point through all models in the dataset is calculated and then their values are mapped for all the points on the mean shape to illustrate that the registration algorithm is independent of the surface curvatures.

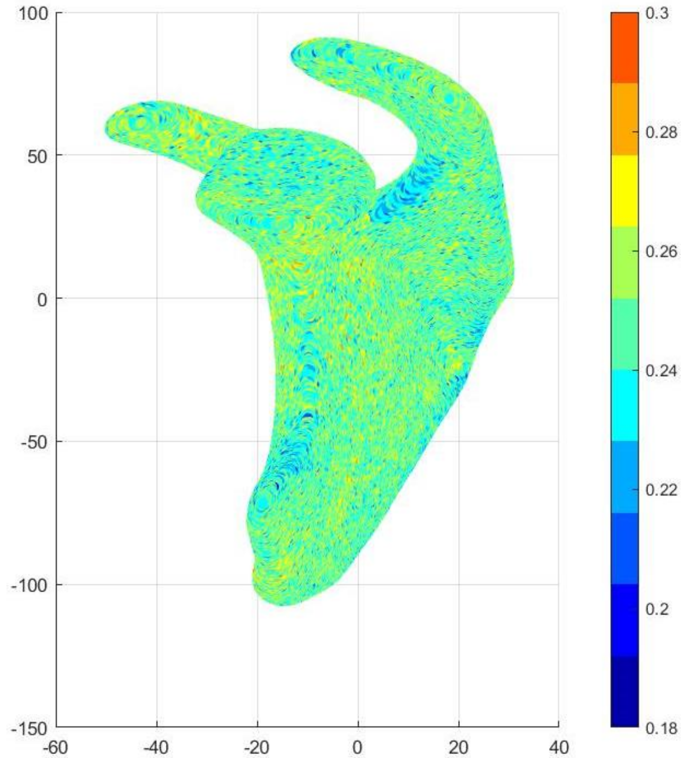

Figure 32. RMS errors of each point are visualized as a heat map diagram for all models in our dataset (units in mm).

It can be observed that the RMS errors of each point through all models in the dataset are evenly distributed on different regions with the range of 0.18 to 0.3 mm. Also, large errors with orange colour do not appear on complex curvatures which shows the registration algorithm is independent of shape complexity like the errors in Acromion neck with more blue range errors.

3.6.2 Correspondence assessment

To evaluate the quality of correspondences, we have to check how accurately each point of the source model has been moved to its new position in the deformed source model while maintaining the original feature correspondences (i.e. to what extent the deformed points continue to lie on the same anatomical features they did in the undeformed source model). Once the NR-ICP algorithm parameters were optimized, the resulting correspondence error was evaluated by comparing the positions of ground truth points and the corresponding point locations produced by the algorithm.

This process starts by having a human observer select anatomical landmarks on the source surface and recording their enumerated index values (i.e. their index number in the list of all points in the mesh). As well, before registration, the observer(s) identify the same anatomical landmarks on the target models and their 3D coordinates are recorded. After registration, the 3D coordinates of the source model landmarks in their deformed positions are retrieved using the above recorded index values. The Euclidean distance between each corresponding landmark on the deformed source and the target models are then calculated. The NR-ICP algorithm would achieve perfect correspondence if all of the calculated Euclidean distances were zero meaning that the anatomical meaning of all landmarks in the undeformed source model exactly matched the human specified location of that anatomical landmark on the target model (N.B. assuming no human error in point selection). Finally, the aforementioned three steps should be repeated for a subset of all models and the average distance can be reported as the correspondence error of the registration method. In this study, a subset of ten models were randomly chosen for correspondence measurements. For the correspondence evaluation, 12 anatomical landmarks were evaluated using the above process. Four anatomical landmarks are located on the glenoid cavity (superior, inferior, anterior and posterior aspects of the glenoid), three on the acromion process, two on the coracoid process, one at the medial end of the spine, one on the superior angle, and one at the inferior angle. The ground truth points selected on the target model are shown in Figure 33 (right) in blue, and on the source model in Figure 33 (left) in red.

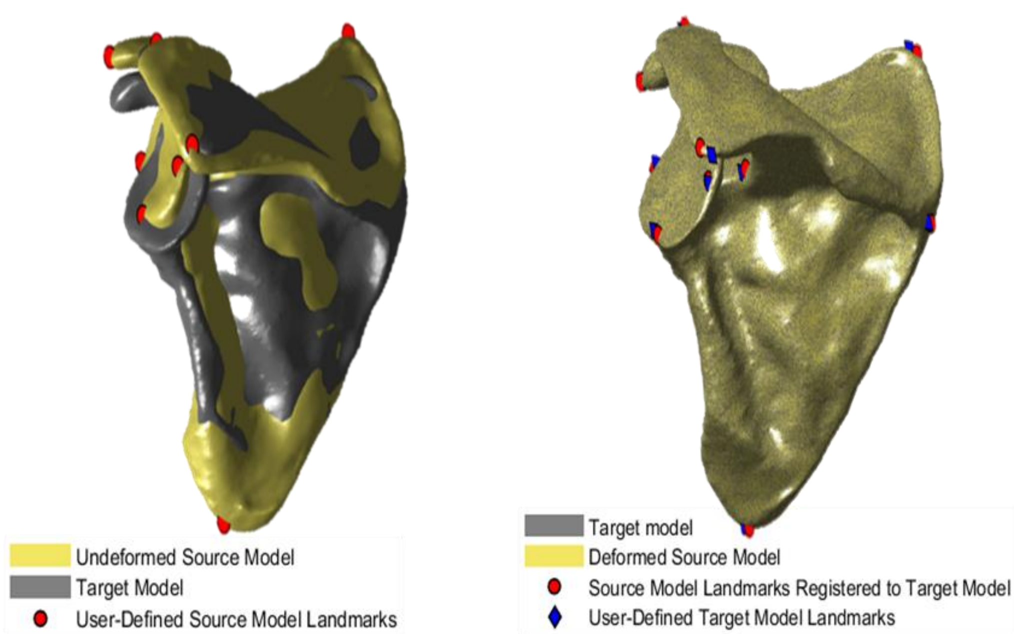

Figure 33. Correspondence evaluation by comparing the positions of 12 ground truth points and the corresponding point locations produced by the algorithm after registration.

The red circles in Figure 33 (right) represent the source landmarks deformed to the target shape through the NR-ICP algorithm. Since the ground truth points are manually selected and can be subject to human error, inter- and intra-observer reliability analysis was performed on a set of 10 scapulae with these 12 anatomical landmarks selected by two independent observers to assess inter-observer reliability and each observer repeated the landmark selection process two times (round 1 and 2) to assess intra-observer reliability. It was found that the 95% confidence interval for intra-observer reliability was ±0.06mm while inter-observer reliability across the two observers was ±0.31mm.

The calculated average Euclidean distance between the ground truth measurements on the 10 target models each with 12 landmark points compared to the deformed source values was found to be 2.74mm. The result of correspondence evaluation is provided in Table 11 and detailed information of correspondence errors on all 12 landmarks for 10 models used by both observers in round 1 is provided in Appendix B.

Table 11. Average correspondence errors of observers in two different rounds on 10 models (numbers in mm).

	Observer 1	**Observer 2**	**Inter-Observer Reliability (mm)**
Round 1	2.93	2.54	0.19
Round 2	2.87	2.61	0.13
Intra-Observer Reliability (mm)	0.03	0.04	

Table 11 illustrates that there is a very small variance between average correspondence errors of two observers and also between two tests, which indicates a great consistency in point selection process between individuals and through each tests. In addition, the average correspondence error of the proposed registration algorithm (2.74mm) is smaller than similar classical affine transformation algorithm result (above 4 mm) in the literature [94].

Utilizing 2D images along with current surgical instruments is not sufficient in correction of severe glenoid deformity due to restricted visualization of glenoid vault in 2D imaging. Therefore, two major techniques, computer-aided surgeries (CAS) and patient-specific instrument (PSI) techniques, have been developed over the last decade to improve correct positioning of glenoid implant in shoulder arthroplasty.

Image-guided surgical navigation systems are increasingly being used in computer-aided surgeries. One of the most important requirement of surgical navigation systems is intraoperative registration method that they employ to map coordinates of preoperative image data into patient coordinate system defined by a localizer during surgery [95]. Thus, developing correspondence maintained algorithm for registration process can help in correct positioning of implant in these type of surgeries.

One method to assess the quality of CAS outcome is similar to the correspondence error calculation procedure that we used in this study. Venne et al. compared conventional and CAS screw placement in RTSA using CT-based pre-operative planning and postoperative evaluation. In this evaluation, five surgeons defined common pre-operative plans on 3D reconstructed cadaveric scapula models using Mimics software and then they performed 3 CAS and 3 conventional simulated procedures. The 3D reconstructed post-operative models were digitally matched to the pre-operative model for error calculation using entry and end points of screw positions. The CAS results was reported significantly more accurate than the conventional ones for the end point location (3.7 ± 2.4 mm < 9.7 ± 6.9 mm) [96].

As end point location error reduced significantly only by using CAS technique (i.e., surgeons and scapula models didn't change during the evaluation process), the CAS error would be resulted from the registration method. Therefore, the correspondence error of our proposed algorithm in section 3.5, which is 2.74 mm can be a reasonable registration result for CAS application and can help to improve the surgical accuracy in shoulder arthroplasty.

Moreover, comparing the correspondence error result with PSI technique results by Suero et al. which measured postoperative implant offset on the glenoid cavity after shoulder arthroplasty, can also assert an improvement in registration accuracy and later in future in surgical outcome. The mean postoperative error in implant position after 10 shoulder arthroplasties (4RTSAs and 6 TSAs) was reported as 3.4 ± 1 mm which greater than our correspondence error [97], [98].

We believe that these correspondence errors demonstrate that the developed algorithm is capable of accurately mapping a common Atlas to the complex and highly varied geometry of eroded scapulae. Therefore, this algorithm is appropriate for use in creating an SSM of scapulae with complex glenoid erosions, which will help to guide treatment in this patient cohort.

Chapter 4

Statistical shape modeling development

In this chapter, Statistical Shape Modeling (SSM), which is a mathematical approach to understand shape variation, will be discussed.

4.1 Statistical shape modeling

Statistical shape modeling is a powerful tool to study the morphological variations and patterns of variability within a population. SSM has a wide range of applications in different fields such as anthropology, biology, pathology, medical imaging, geography, computer vision, etc. SSM gives a statistical understanding of the variability in a given population of archetypally similar shapes (e.g. a given bone).

Statistical shape modeling was pioneered by Cootes et al [99] in 1991. They proposed a method to represent 2D shapes through a parametric description of variability. Later in 1995, the same group presented a new method named Active Shape Model that can build flexible models from a group of objects [100]. Shape modeling has now been used in many studies and in different fields like face recognition [101], and medical application [102].

4.2 Point distribution model

A statistical shape model is fundamentally a point distribution model (PDM). PDM is a statistical deformable shape model based on principal component analysis that describes the mean coordinates and their spatial variability for all nodes that make up the shape under study [100]. This information is derived from a set of known shapes that represent a given population. To build a statistical shape model, each shape instance drawn from the population (e.g. each patient scapula in this work) should be represented as a distributed surface mesh composed of nodes with the same number of nodes on each shape. In order to obtain the nodal data, MATLAB code was used to convert the 3D structures, described in Chapter 3, from STL files to meshed surfaces from which nodal coordinate data could be extracted and the NR-ICP algorithm, also described in Chapter 3, was used to generate surface meshes with identical mesh architecture for the target shapes in our dataset using the source model mesh.

If there are N target shapes in the dataset then each deformed source mesh corresponding to that target model is composed of n node points which can be described as a vector with dimensions 3n (due to the x, y, z coordinates for each node) and this forms a matrix (DS) with dimensions 3n × N representing all of the target shapes with identical mesh structure in the dataset as shown in Eq. (14):

$$DS = \begin{bmatrix} x_{11}, \dots, x_{1n}, y_{11}, \dots, y_{1n},\ z_{11}, \dots, z_{1n} \\ \vdots \\ x_{N1}, \dots, x_{Nn}, y_{N1}, \dots, y_{Nn},\ z_{N1}, \dots, z_{Nn} \end{bmatrix}^T \tag{14}$$

In other words, *DS* matrix contains all target shapes using source model mesh (Deformed Source) as DS_j vector where j= {1, 2, 3… N} and simplified version of *DS* matrix can be represented by Eq. (15):

$$DS = \begin{bmatrix} DS_1 \\ \vdots \\ DS_N \end{bmatrix}^T \tag{15}$$

4.3 Correspondence issue

The most critical part in building PDMs is a fundamental assumption which requires the shape's points to be in point-to-point correspondence with each other. This means that the n^{th} point in each shape describes the same anatomical location as in all other shapes. Establishing precise correspondence among all shapes in a dataset is critical in order to be able to generate an accurate PDM but is significantly complicated by the complexity of anatomical bone geometries in the human body. Therefore, various types of image-based and mesh-based techniques are used in medical application in order to achieve accurate PDMs for the complex anatomical shapes [103], [104].

Given the use of a dataset of shapes with identical correspondence, the data derived from an SSM generated from that dataset will also have a one-to-one correspondences with the original shapes.

4.4 Principal component analysis

Dealing with large data in numerical analysis is a critical challenge. Many techniques have been discovered to reduce the dimensionality while preserving most of the dataset's information [105]. One of the oldest and most commonly used methods is Principal Component Analysis (PCA). It was first presented in the field of statistics by Karl Pearson in 1901. He formulated PCA as closest fit of points in two, three or higher dimensions [106]. Over time, numerous books have been written on this subject [107] and many papers have been published on PCA in different disciplines [105], [108].

In this section, the main idea of PCA is defined in detail. PCA projects the original data into a lower-dimensional space and embeds the data in a more compact representation. PCA is a dimension-reduction tool that is used to transform a number of correlated variables into a smaller number of uncorrelated variables called principal components (PCs). They are usually arranged from the component with the most variability to the least variability. It means that the first principal component accounts for as much of the variability in the data as possible, and each subsequent component accounts for as much of the remaining variability as possible.

To make this concept clear, we can first explain PCA using a 2D example. If we consider data that are scattered in 2D space such as in Figure 34, PCA can yield the main direction and secondary direction of variability as an orthogonal coordinate system in order to illustrate the maximum variance of the points in each direction. The principal axes of the orthogonal coordinate system are calculated by eigenvectors and eigenvalues of the covariance matrix [109], [110].

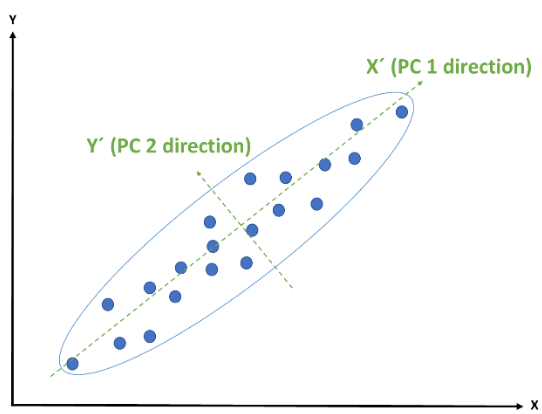

Figure 34. Illustration of PCA concept and the orthogonal coordinate system for 2D data

4.4.1 Covariance matrix

In statistics, measurement of joint variability between two variables is called covariance. If two variables of x and y, behave similarly which means the greater value of one of them correspond to the greater value of the other one, the covariance is positive otherwise it is negative. This sign of the covariance conveys the tendency in a linear relationship between two variables and it can be seen in two variables of x and y for 20 observations (each blue spot is one observation) in Figure 35.

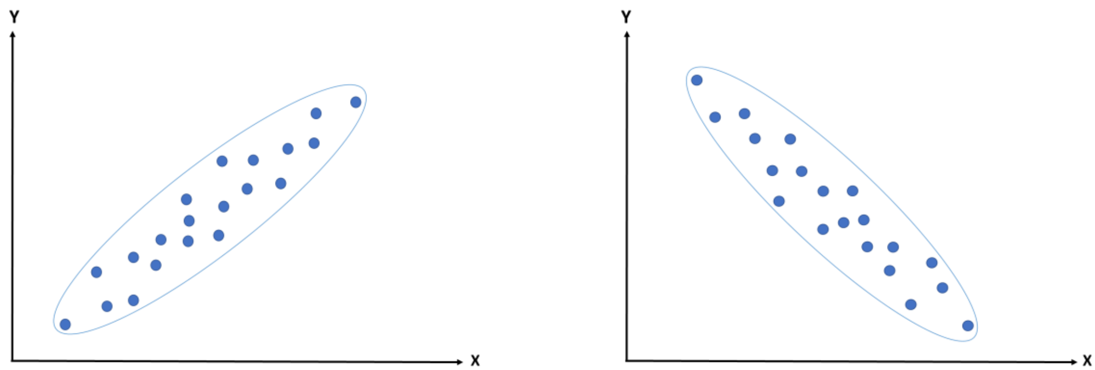

(a) **Covariance (x, y) > 0**

(b) **Covariance (x, y) < 0**

Figure 35. Illustration of covariance's sign which is positive in (a) and negative in (b).

If we have two variables, x and y, the unbiased estimator of the covariance matrix which is a square and symmetric matrix is defined by Eq. (16):

$$Covariance = \begin{bmatrix} Cov(x,x) & Cov(x,y) \\ Cov(y,x) & Cov(y,y) \end{bmatrix} \tag{16}$$

Where in Eq. (17) $Cov(x, y)$ is:

$$Cov(x,y) = \frac{1}{N-1}\sum_{i=1}^{N}(x_i - \bar{x})(y_i - \bar{y}) \tag{17}$$

Also $\bar{x}$ and $\bar{y}$ are the sample mean and N is the total number of observations. Sample means are defined in Eq. (18) and (19):

$$\bar{x} = \frac{1}{N}\sum_{i=1}^{N} x_i \tag{18}$$

$$\bar{y} = \frac{1}{N}\sum_{i=1}^{N} y_i \tag{19}$$

When two variables are identical, the covariance in that specific case is called variance and the covariance matrix can be presented as Eq. (20):

$$Covariance = \begin{bmatrix} Var(x) & Cov(x,y) \\ Cov(y,x) & Var(y) \end{bmatrix} \tag{20}$$

And variance(x) is defined as $Var(x)$in Eq. (21):

$$Var(x) = \frac{1}{N-1}\sum_{i=1}^{N} (x_i - \bar{x})^2 \tag{21}$$

The most important part in statistical research is to determine the variable and observations accurately. Therefore, it is critical to define the variables based on the available data and with respect to the purpose and objectives of the project. As it is discussed in previous chapter, the main goal of this project is statistical shape analysis of the scapula, thus the observations are anatomical shapes of scapulae in the dataset, which are 61 models. As a result, there are 61 observations. With respect to the variables of interest, because each observation is a scapula shape instance, the variables are the spatial coordinates in Cartesian space (x, y, z) of all nodes describing the shape.

For each observation (i.e. a scapula model which is a deformed source model), there are thousands of points on the meshed surface and can be represented by the DS_j vector in Eq.(22), which was already discussed in section 4.2:

$$DS_j = [x_{j1}, \dots, x_{jn}, y_{j1}, \dots, y_{jn},\ z_{j1}, \dots, z_{jn}]^T \tag{22}$$

Where j = {1, 2, 3…, N} and N = 61 in this study. Also, n is the number of points in each mesh and n=119K in this study. Like a covariance matrix for two variables which is a two by two matrix, a covariance matrix can be formed for any higher number of variables as well. Moreover, it should be considered that due to the correspondence issue, the total number of points (e.g. variables) in each model is equal. Thus the covariance matrix for the full dataset, *DS*, is a 3n × 3n matrix and n is the number of points or nodes of the meshed surfaces. The covariance matrix for the dataset is written in Eq. (23):

$$Cov(DS) = \frac{1}{N-1}\sum_{j=1}^{N} \left(DS_j - \overline{DS}\right)\left(DS_j - \overline{DS}\right)^T \tag{23}$$

Where $\overline{DS}$ is the mean shape of all models in the dataset and it can be calculated by Eq. (24):

$$\overline{DS} = [\bar{x}_1, \dots, \bar{x}_n, \bar{y}_1, \dots, \bar{y}_n, \bar{z}_1, \dots, \bar{z}_n]^T \tag{24}$$

Where $\bar{x}_n, \bar{y}_n$, and $\bar{z}_n$ can be determined using Eq. (25):

$$\bar{x}_n = \frac{1}{N}\sum_{j=1}^{N} x_{nj} \tag{25}$$

$$\bar{y}_n = \frac{1}{N}\sum_{j=1}^{N} y_{nj}$$

$$\bar{z}_n = \frac{1}{N}\sum_{j=1}^{N} z_{nj}$$

In this research N = 61 models and n = 119537 points.

As a result, this translates into a very large covariance matrix (n by n) and yields a computationally challenging problem. With high dimensional datasets such as this, the computation problem can be overcome through mathematical manipulations that restate the problem in a simpler form. In this case, a smaller matrix *D*, which has N×N dimensionality, can be computed instead of the covariance matrix of *S*. The most important aspect of this solution is that due to the reasonable dimensions of matrix *D*, calculation of its eigenvectors and eigenvalues is feasible. Matrix *D* can be computed by Eq. (26):

$$D(S) = \frac{1}{N-1}\sum_{j=1}^{N}\left(DS_j - \overline{DS}\right)^T\left(DS_j - \overline{DS}\right) \tag{26}$$

Now eigenvectors and eigenvalues of the matrix *D* are computable and can be calculated by Eq. (27):

$$D\,\psi = \gamma\,\psi \tag{27}$$

Where ψ are the eigenvectors and γ are the eigenvalues. After some simple algebra, the eigenvalues (λ) and eigenvectors (φ) of the initial covariance matrix of *DS* (n by n) can be found as in Eq. (28):

$$\varphi = (DS - \overline{DS})\psi \tag{28}$$

$$\lambda = \gamma$$

The detailed calculation is attached in the Appendix A.

4.4.2 New shape construction

Following generation of a statistical shape model as described earlier in the chapter, a new shape derived from this knowledge of the variability in the population can be constructed through linear combination of the first c modes of variation as shown in Eq. (29):

$$SH_i = \overline{SH} + \sum_{m=1}^{c} \varphi_m b_m \tag{29}$$

Where $\overline{SH}$ is the mean shape and in our case is $\overline{DS}$, *m* is the number of mode of variation, c is the total number of modes that new shapes need to be reconstructed with (i.e., it can be a number from 1 to total number of shapes minus one), φ_m is the *m*th eigenvectors and b_m represent the weight for mode m. It means that each new shape is reconstructed by adding weighted eigenvectors to the mean shape. A method to constrain the weight parameter to avoid unrealistic shapes is to have b_m lay inside $[-3\sqrt{\lambda_m}, 3\sqrt{\lambda_m}]$ which allows the weights to be in the range of plus or minus three standard deviations, in that case the SSM can capture more than 99% of the variation. It should be noted that as this equation is a linear combination of different modes, new shapes can be reconstructed using individual mode of variation (i.e., using m=1 or 2 or 3, etc.) as well as linear combination of different modes.

We can rewrite the previous equation by a linear combination of the eigenvalues, eigenvectors and mean shape. The reconstructed shape model can be also described by Eq. (30):

$$SH_i = \overline{SH} + \sum_{m=1}^{c} \alpha_i \sqrt{\lambda_m} \varphi_m \tag{30}$$

Where λ_m is the m^{th} eigenvalues and the α_i coefficient is a variable which can be chosen from a standard normal distribution with zero mean and unit variance ($\alpha \sim N(0,1)$) that can be either a positive or a negative value [102], [111].

Chapter 5

SSM results and discussion

In this chapter, results of statistical shape modeling on the scapula dataset along with evaluation methods used to assess the performance of SSM will be discussed. Additionally, various anatomical measurements are applied on all specimens in the dataset (i.e. outputs of proposed NRICP algorithm) as well as reconstructed shapes using SSM to compare and demonstrate the ability of SSM to generate new instances. Moreover, another set of anatomical measurements is performed on SSM results to quantify the independent shape variation in each principal mode of variation.

5.1 SSM results

To fulfill the objectives of this study, after registration, Principal Component Analysis is performed on all 61 deformed models as a group to describe independent modes of variation in the dataset. These modes of variation systematically describe shape variation and reconstruct bone shapes representing a specific morphological variant.

In Figure 36, the result of only the first 3 modes of variation in scapula shape across ±2 standard deviations are provided for illustrative purposes but all modes of variation are used for the SSM evaluation process in the next section. The SSM demonstrated that the first mode of variation, as predicted, represented the size variation across the population which is shown in Figure 37. While in the second mode, we can see the decrease in Critical Shoulder Angle and the increase in the height of the scapula from right to left and this is presented in Figure *38*. Finally, in the third mode, we can see an increase in the size of the glenoid cavity along with shifting acromion position from the superoposterior to superoanterior side of the scapula from right to left in Figure *39*.

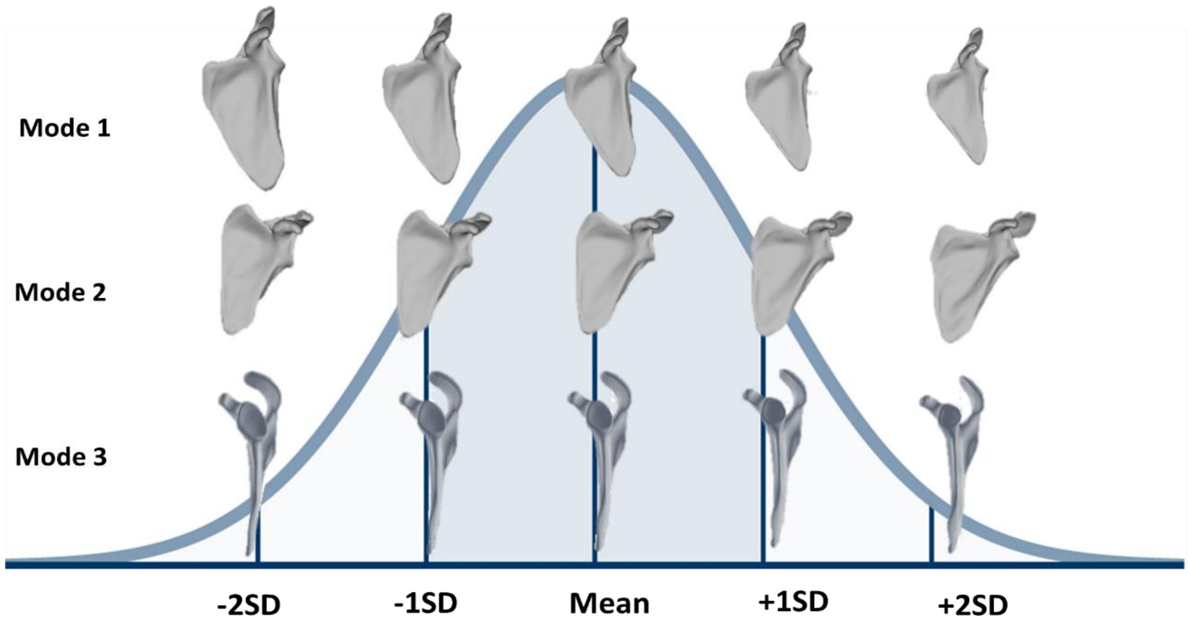

Figure 36. Illustration of first three modes of variation of the scapula by changing the standard deviation (SD) from -2SD to 2SD.

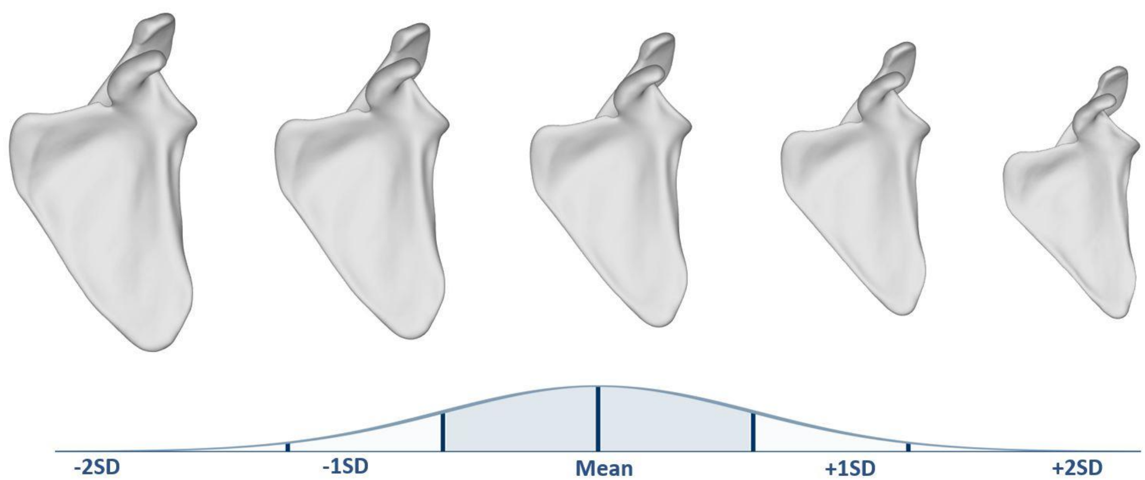

Figure 37. Illustration of first mode of variation which represents the size variation.

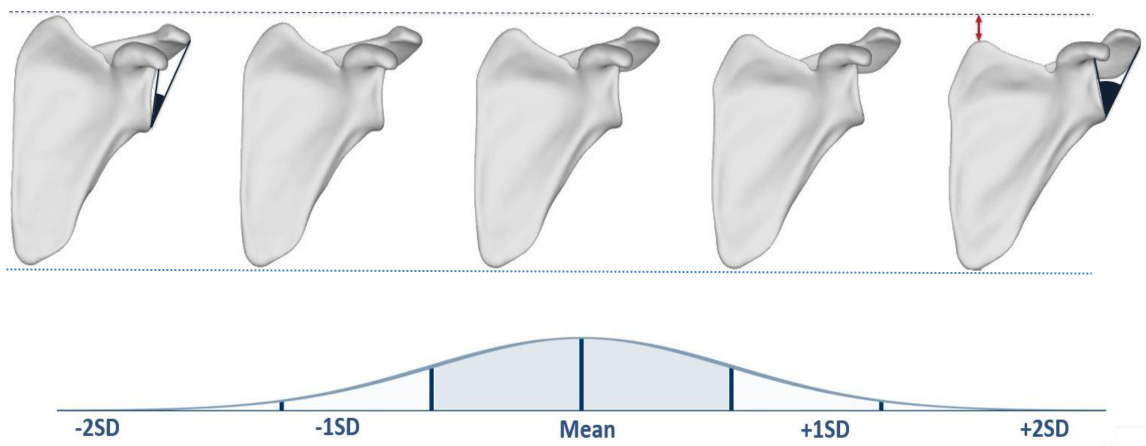

Figure 38. *Illustration of second mode of variation which reflects variation in changes in Critical Shoulder Angle (CSA) and the height of the scapula.*

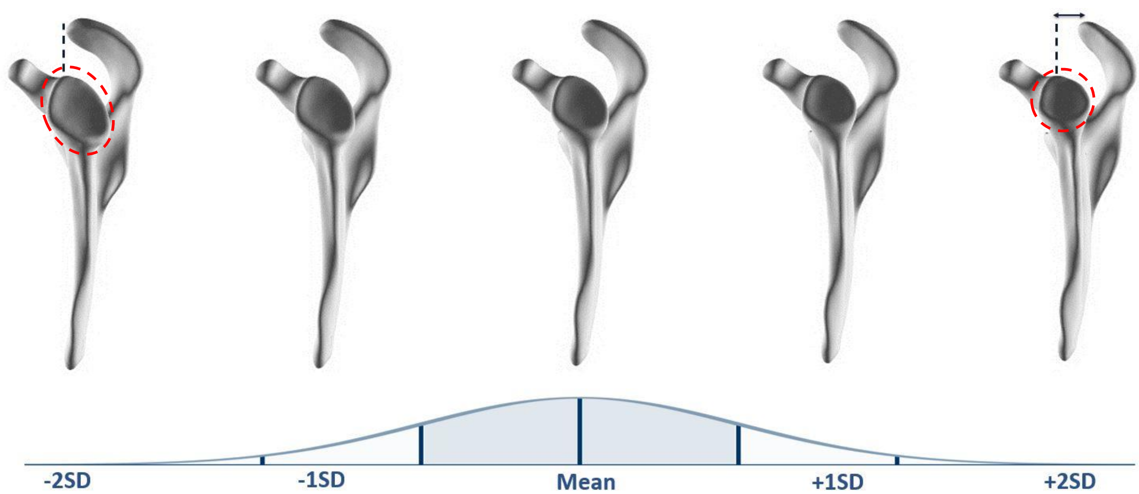

Figure 39. *Illustration of third mode of variation which accounts for a variation in the size of glenoid cavity and shifting acromion position from the superoanterior to superoposterior side of the scapula.*

5.2 SSM evaluation

The efficiency of the statistical model depends on its ability to generate new and valid shape instances using as few parameters as possible. The following sections analyze the statistical models qualitatively and quantitatively [112], [113]:

5.2.1 SSM qualitative analysis

This analysis visually inspects the scapula shapes reconstructed using the SSM and observed to what extent each mode of variation changes independently from the others since the eigenvectors are orthogonal. In this study, the first three principal modes of variation have been visually inspected when changing the standard deviation from -2SD to +2SD and results are represented in Figure 36.

In mode 1, it can be recognized easily that size variation is the only parameter in the shape variation while in mode 2, height is the shape variation parameter without changes in other size parameters. In mode 3, overall size and height of the scapula are not changed but it can be observed clearly that the glenoid size has been decreased from -2SD to 2SD as well as acromion location shifted from the superoanterior to superoposterior side of the scapula.

5.2.2 SSM quantitative evaluation

The SSM quality can be evaluated through three standard criteria of generalization ability, specificity, and compactness which was introduced by Davies et al. for shape modeling to evaluate the capability of SSM to generate valid new instances [113], [112]. These three standard metrics for assessing the quality of constructed shape models will be discussed in detail in the following sections.

5.2.2.1 Generalization ability

This metric measures a model's ability to represent unseen instances of the class of object for a certain number of modes of variation. The generalization ability of each model is measured from the input dataset using leave-one-out (LOO) cross validation. Specifically, an SSM is built using all but one member of the dataset and then the model is fit to the excluded example by least squares fitting of the parameters of Eq. (32) until error is minimized. The accuracy to which the model can describe the unseen example is measured and the process is repeated until all models in the dataset are left out and tested. The approximation error is then averaged over the complete set of models in the dataset and the generality equation is given by Eq. (31):

$$G(M) = \frac{1}{N}\sum_{i=1}^{N} \| \acute{S}H_i(M) - SH_i \|^2 \tag{31}$$

Where SH_i is the excluded shape (i.e. unseen instance) and *N* is the total number of shapes in the dataset. New instances are shown by $\acute{SH}_i(M)$ and generated by Eq. (32):

$$\acute{SH}(M) = \overline{SH} + \sum_{i=1}^{M} \varphi_m b_m \tag{32}$$

Where $\overline{SH}$ is the mean shape, φ_m is the *m*th principal component or eigenvector from the SSM, *M* is the total number of modes of variation being considered in the generalization calculation, and b_m is defined as Eq. (33):

$$b_m \epsilon [-3\sqrt{\lambda_m}, 3\sqrt{\lambda_m}] \tag{33}$$

In this study, a generalization error of 2.6 mm is found when using the first 9 modes. Figure 40 illustrates the generalization ability of our SSM model using up to the first 9 modes of variation, where the x-axis represents the number of modes used to generate new instances and y-axis represents the generality error in mm.

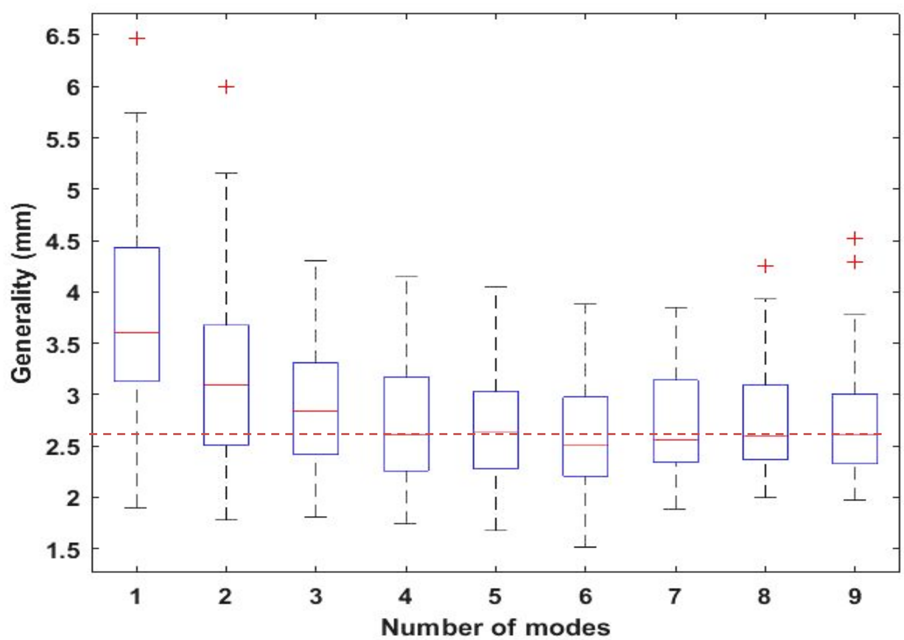

Figure 40. SSM evaluation using leave-one-out cross validation to check generalization ability for the first 9 modes of variation. Horizontal red lines, red plus signs, horizontal black lines, dash lines and blue rectangle represent median, outliers, min/max, whisker and interquartile range.

In Figure 40, it can be noticed that by increasing the number of modes of variation used in generating new instances, the generalization ability of SSM is increased since the generality error has decreased. The highest generalization error is related to the first mode, which only represents the size variation, and it is not possible to reconstruct all the fine anatomical features of scapula models using only one mode of variation. As a result, by adding more modes of variation, generalization ability of the SSM can be improved to build in more anatomical detail. It should be noted that for Figure 40, Euclidean distance is used to represent distances between unseen shapes and closest reconstructed models. Each boxplot covers 61 results since in each time one model from dataset is left out as unseen shape and then closest shape to the unseen shape from new instances that have been generated using m number of modes of variation is found and Euclidean distance between unseen shape and the closest instance is calculated.

In addition, to show the generalization ability over all modes of variation, RMS error of 61 results shown in each boxplot of Figure 40 is calculated for all modes and represented in Figure 41. The reason that RMS criteria is chosen for reporting the generalization ability error of our LOO cross validation results is that RMS magnifies the effect of error between different models in each mode. Since the ability of our SSM model to generate new instances is being assessed in this evaluation.

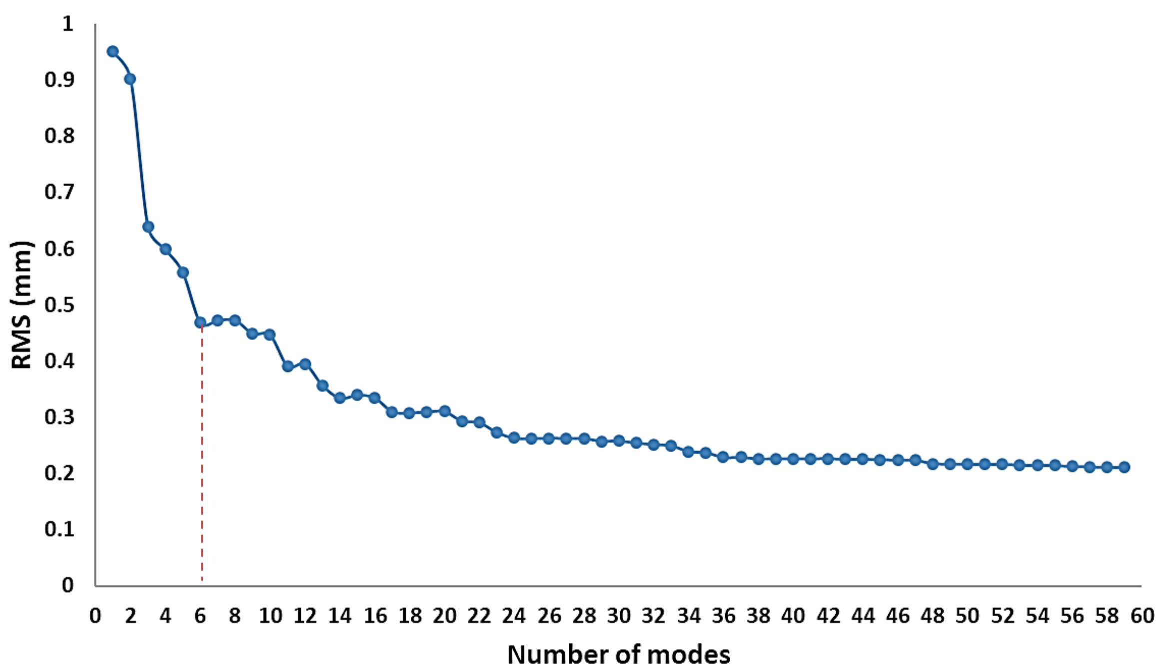

Figure 41. RMS error results for generalization ability of SSM based on number of modes of variation used in shape reconstruction.

Figure 41 shows that RMS error ceased to decrease by 10% after 6 modes of variation, which means that including more number of modes in shape reconstruction would have minimal effect on generating more accurate instances of unseen shapes.

Also, the SSM model built in this study illustrated better results compared to similar research on 85 healthy scapulae (RMS error reported above 2 mm in mode one and more than 1.4 mm for mode 9 while it is less than 0.5 mm in our study, see Figure 42) which used classical affine transformation in their registration algorithm [94], thus further confirming the efficacy of this model.

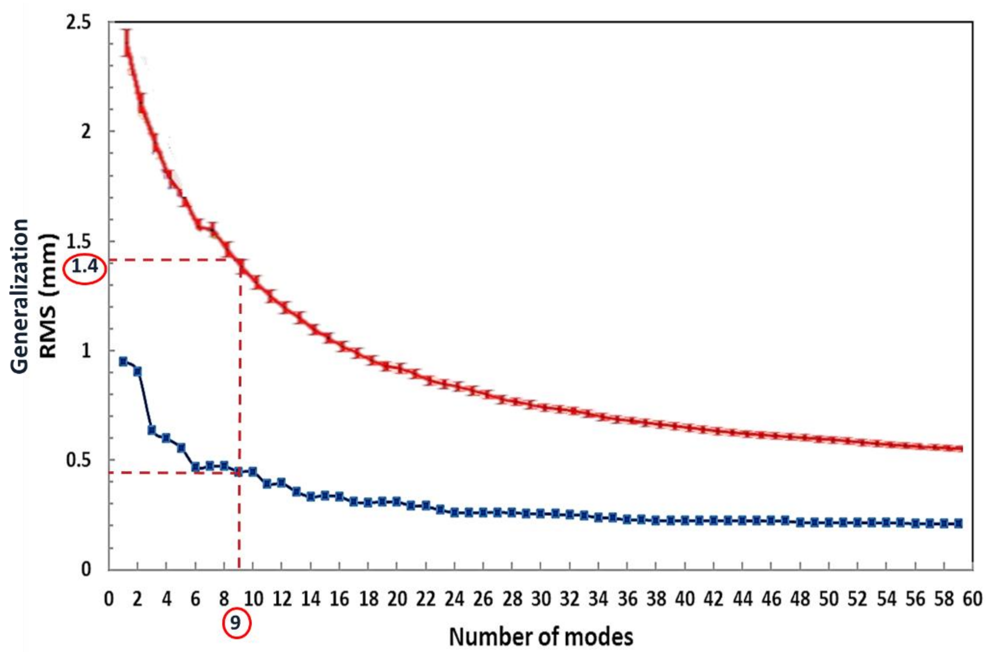

Figure 42. Comparing the generalization results calculated by RMS error for all models of the dataset in blue with similar study in the literature in red [94].

5.2.2.2 Specificity

Specificity measures a model's ability to generate instances that are similar to those in the dataset. It is measured by generating a large set of shape instances using the constructed model. The approximation error is defined as the distance between the generated shape instance and its most similar sample in the dataset. The specificity is the average approximation error of all the generated shape instances which is represented as *SP* in Eq. (34).

$$SP(M) = \frac{1}{N_{SP}} \sum_{i=1}^{N_{SP}} \| SH_i(M) - \acute{SH}_i \|^2 \tag{34}$$

Where $SH_i(M)$ are shape examples randomly generated using M principal modes, N_{SP} =10000 is the total random shapes generated; this number should be considered large enough comparing to size of the dataset and N_{sp} in this test is chosen based on the literature [112], and $\acute{SH}_i$ is the nearest member of the dataset to $SH_i(M)$ which is given by Eq. (35).

$$SH(M) = \overline{SH} + \sum_{i=1}^{M} \varphi_m b_m \tag{35}$$

Figure 43 illustrates the specificity for our SSM model by varying the number of modes of variation from 1 to 9. The calculated specificity over 10,000 instances constructed for the first nine modes of variation ranged between 2 to 3 mm from mode 1 to mode 9. On the contrary to generalization ability results, specificity error increased by including more number of modes of variation in random shape reconstruction. Since more modes of variation result in uncommon shape instances that may not actually appear within the dataset used to construct the SSM.

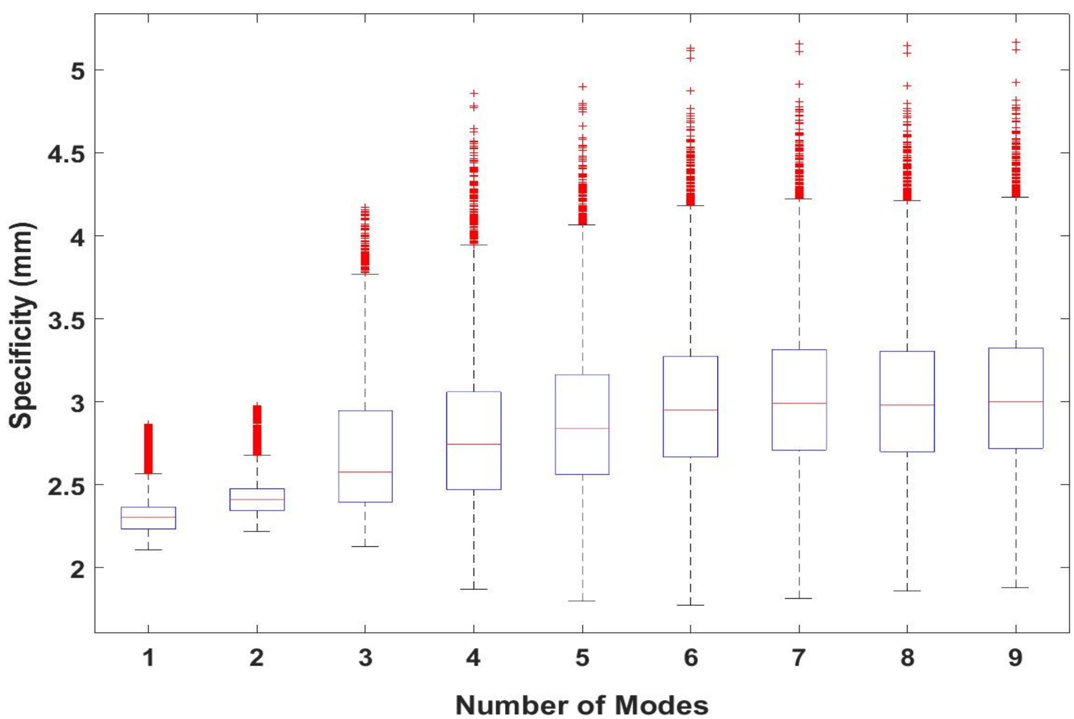

Figure 43. Specificity results over 10,000 instances for different number of modes from mode 1 to mode 9. Horizontal red lines, red plus signs, horizontal black lines, dash lines and blue rectangle represent median, outliers, min/max, whisker and interquartile range.

Specificity error presented in Figure 43 is slightly higher than reported errors in similar researches on scapula due to different number of runs, number of models in dataset, error calculation or presentation methods [94], [114] but the most important difference is that this study is done on eroded scapulae with complex deformities and various geometries while the two studies mentioned are performed on healthy scapulae.

5.2.2.3 Compactness

Another standard metric to evaluate the quality of SSM models is compactness. This metric is defined by Davies et al. to assess how efficiently a model represents the variation across the population. An efficient model is one that uses the fewest number of variables (i.e. modes of variation) possible to describe the most variation. Compactness is measured as the cumulative variance up to and including the M^{th} mode of variation. The compactness equation used for this study is the cumulative summation of the eigenvalues which is normalized to the total variation and it's presented in Eq. (36) [115]:

$$C(M) = \frac{\sum_{i=1}^{M} \lambda_m}{\sum \lambda} \tag{36}$$

Figure 44 shows the compactness for our SSM model with increasing number of modes of variation.

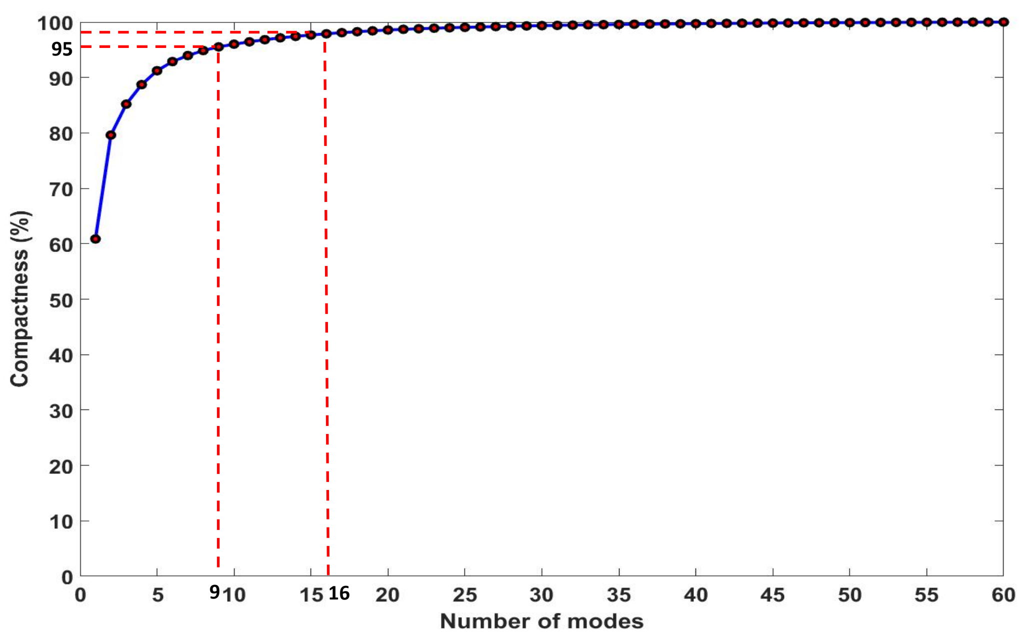

Figure 44. Cumulative variance percentage by number of principal components is shown for all 60 modes of variation.

In this study, the first nine principal components accounted for 95% of variability in the dataset and the first sixteen principal components accounted for 98% variability.

Compactness of this SSM model shows better result than the similar studies in the literature as M. Mayya et al. reported less than 80% variability (see Figure 45) and Salhi et al. reported less than 90% variability for their first 9 modes of variation [94], [114]. It can be seen that the first mode, which describes size variation, accounts for fully 60% of all variation in the dataset, while the second mode, which relates to scapula height variation, accounts for a further ~20% of all variation, and thereafter each mode accounts for less than 5% of variation.

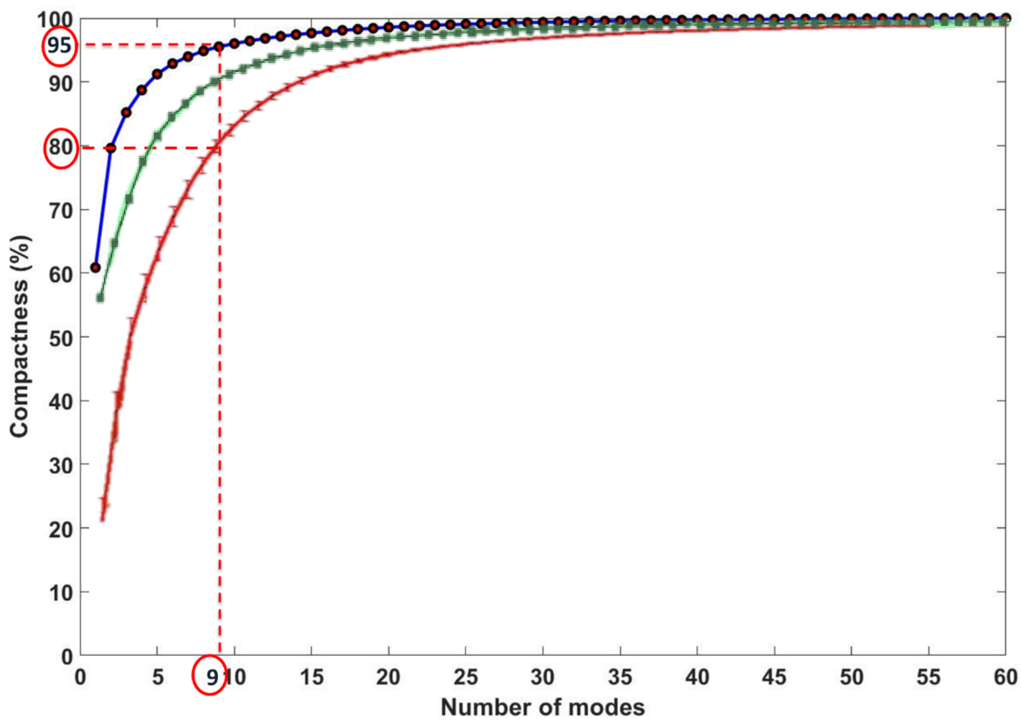

Figure 45. Comparing the compactness results for all modes of variation in blue with similar studies in the literature in red and green which shows 95% variability by 9 modes of variation for our proposed study while in similar studies they account for 80% and 90% variability respectively [94], [114] .

5.3 Anatomical measurements

Many studies have been conducted on quantifying the size and shape of the scapula, and some of them have evaluated the disparity in terms of gender to better understand the variation in both males and females. However, few studies attempted to quantify the variation between healthy and eroded shoulder bones which can be beneficial in surgical planning and implant design for shoulder arthroplasty.

However, computation of anatomical measurements on each specimen in a dataset is a time-consuming process and may produce inconsistent results due to operator error. Therefore, automated anatomical measurements are necessary when we are working with a large group of subjects. To achieve automated measurements, we can employ the knowledge and results we gained from the registration step in the SSM construction process. Since the number of points in the surface meshes generated in the NR registration process are equal and have point-to-point correspondence, we can use their identical index numbering to measure various parameters on all scapulae in a systematic manner. However, consistency in computation of automated anatomical measurements significantly depend on accuracy and robustness of the registration method used in producing surface meshes for each scapula. For that reason, the mesh correspondence preserving registration algorithm developed in Chapter 3 is ideal for creating meshes that allow for automatic anatomical measurements to be calculated.

In this section, the measurement techniques to find important dimensions of the scapula and glenoid articular surfaces will be discussed. Moreover, common terminologies related to the aforementioned measurements will be described.

5.3.1 Coordinate system transformation

One of the most important steps in measuring anatomical parameters is defining the scapula's coordinate system. As mentioned in previous chapters, all of the scapulae in the dataset are placed in the same coordinate system after the pre-processing step in the registration process. To make sure that all of the target shapes are located in the same coordinate system, they are aligned with the main axis of the source model, which was obtained from a PCA. Although, all of the target shapes were in the same coordinate system their orientation was not meaningfully aligned with an anatomical coordinate system. Therefore, a new scapula specific anatomical coordinate system needed to be defined.

5.3.2 Standard scapula coordinate system

A great deal of work has been undertaken to define standardized joint coordinate system (JCS) definitions. Grood and Suntay were the pioneers in this area for the JCS of the knee joint at 1983 [116] whereas the shoulder standardization was first undertaken in 1996 by Van der Helm [117]. In this study, the International Society of Biomechanics (ISB) shoulder JCS recommendation was used [118]. The proposed directions of X, Y and Z coordinates for the glenohumeral joint on a right shoulder is shown in Figure 46. In this definition, the origin of coordinate system is located at the center of glenoid cavity. The X axis is pointing forward (from posterior to anterior) for a right shoulder and pointing backward (from anterior to posterior) for a left shoulder. Also, the Y axis is pointing upward (from inferior to superior) and the Z axis is pointing from medial to lateral.

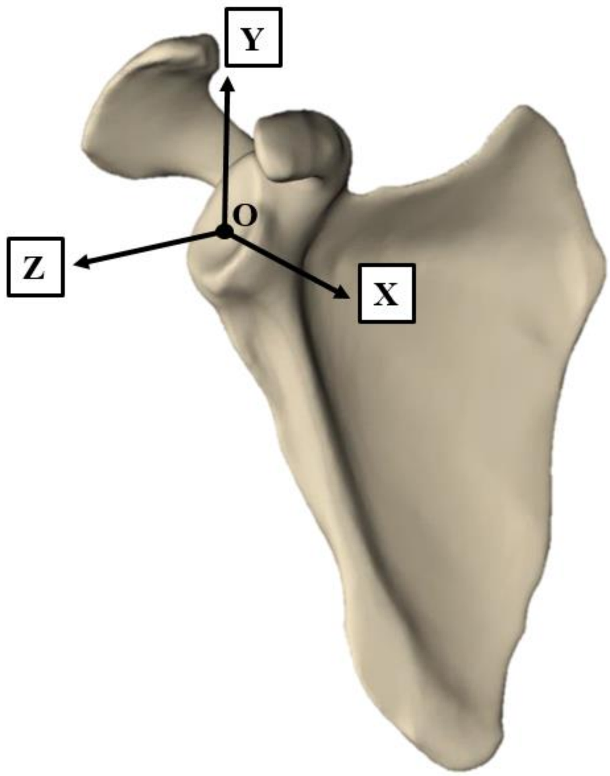

Figure 46. Illustration of recommended direction of X, Y and Z coordinates of ISB on a right shoulder with origin at the center of glenoid.

The first step to transform the coordinate system for our specimens is to define our reference planes (Cartesian planes). The detailed description of the three points (point A, B and C) used to define this plane are detailed in Table 12 and their positions are shown on a left shoulder in Figure 47.

Table 12. Description of three characteristic points of scapula.

Point	Point Name	Point Description
A	Glenoid center	The center of the best-fitting inferior circle on the glenoid cavity while facing the glenoid from lateral to medial [119].
B	Trigonum spinae	The point on the most medial part of scapular spine located at the intersection of the scapular spine and medial border of the scapular body while facing directly from anterior to posterior.
C	Angulus inferior	The most inferior point on the scapula body while facing directly from posterior to anterior.

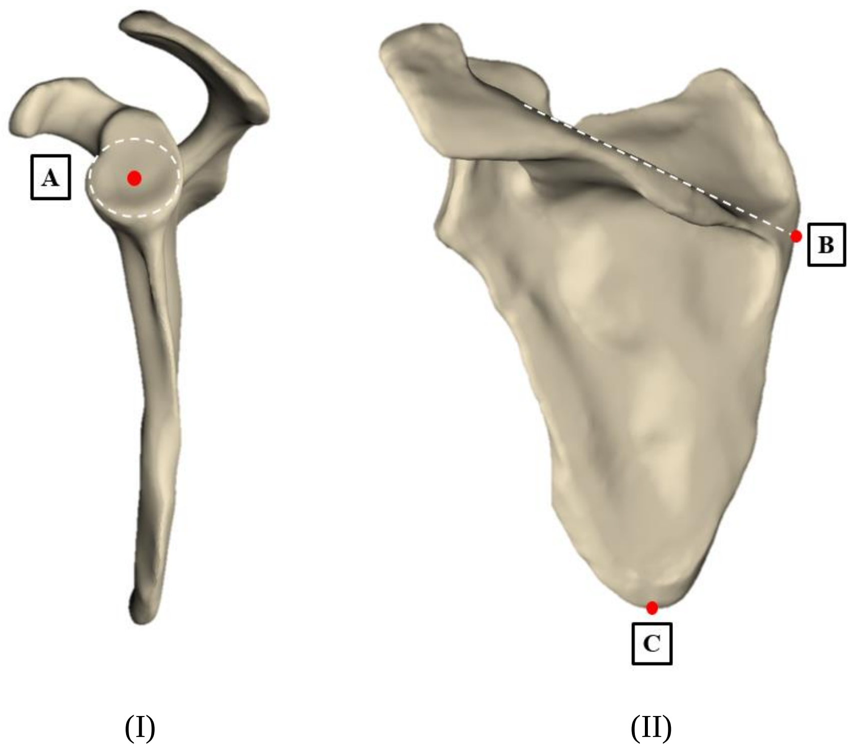

Figure 47. Illustration of three characteristic points required for the coordinate system transformation on left shoulder. (I): lateral view and (II): posterior view.

When the characteristic points are selected, we can define the X, Y and Z coordinates for the left shoulder. According to ISB recommendation, the BA vector will be our Z_{axis} and the X_{axis} should be perpendicular to the plane formed by the three points. Therefore, the cross product of Z axis and CA vector will form our X coordinate. Finally, to determine the Y_{axis}, the cross product of Z and X axes should be calculated. Schematic view of these axes is shown in Figure 48 and detailed equations to find each coordinate are presented in Eq. (37), (38) and (39):

$$\bar{Z}_{axis} = \frac{\bar{A} - \bar{B}}{|\bar{A} - \bar{B}|} \tag{37}$$

$$\bar{X}_{axis} = \frac{\bar{Z}_{axis} \times (\bar{A} - \bar{C})}{|\bar{Z}_{axis} \times (\bar{A} - \bar{C})|} \tag{38}$$

$$\bar{Y}_{axis} = \frac{\bar{Z}_{axis} \times \bar{X}_{axis}}{|\bar{Z}_{axis} \times \bar{X}_{axis}|} \tag{39}$$

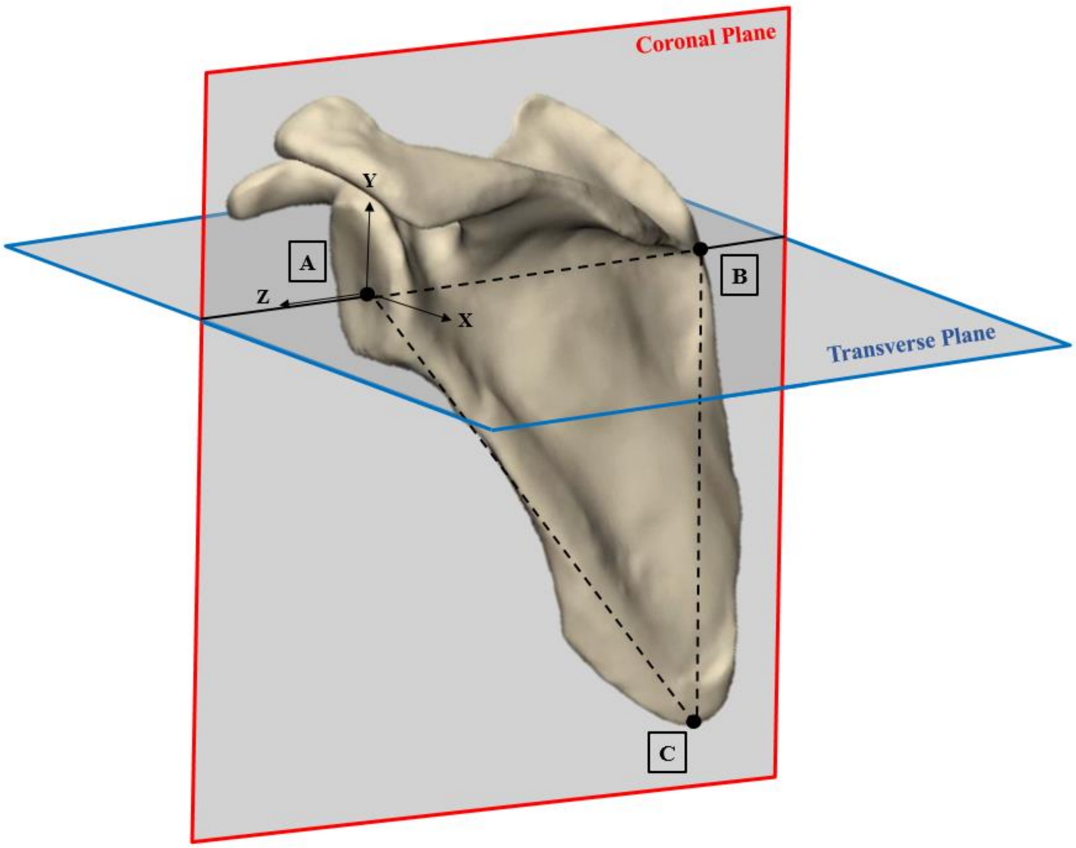

Figure 48. Schematic view of coronal and transverse planes along with three characteristic points and corresponding coordinate system for a left shoulder.

To transform the global coordinate system to the new one, we need a transformation matrix combining translation and rotation matrices. The transformation matrix of scapula from global coordinate system to the new coordinate system is written in Eq. (40):

$$ {}_{G}^{N}T = \begin{bmatrix} {}_{G}^{N}R & {}_{G}^{N}P \\ 0 & 1 \end{bmatrix} \tag{40} $$

Where ${}_{G}^{N}R$ is the rotation matrix (3 by 3 matrix), ${}_{G}^{N}P$ is the translation matrix (3 by 1 matrix) which is shown in Eq. (41) and ${}_{G}^{N}T$ is a 4 by 4 matrix.

It should be noted that since the origin of our new coordinate system is placed on the center of glenoid, the translation matrix is point A.

$$ {}_{G}^{N}P = \begin{bmatrix} x_A \\ y_A \\ z_A \end{bmatrix} \tag{41} $$

And the rotation matrix is described as Eq. (42):

$$ {}_{G}^{N}R = [\bar{X}_{axis} \quad \bar{Y}_{axis} \quad \bar{Z}_{axis}] \tag{42} $$

By applying the aforementioned transformation matrix to each specimen's point cloud which are specified already, their coordinates can be transformed into the new coordinate system. Now, everything is prepared to start the measurement process.

5.3.3 Definition of measurement parameters

Various studies have been performed on to make anatomical measurements of the scapular body to investigate the size, shape and position of different part of the scapula [120], [121]. In addition, several methods and techniques are proposed in clinical research to diagnose dissimilarity or abnormality in different cases for the scapular body [122] , [123] , [124]. These quantifications can be measured on 2D images such as: X-rays, CT scans, MRI etc. [125]or on 3D reconstructed shapes in any data visualization software [126] or even on human body using measurement tools like vernier calipers or inclinometer [127], [128].

In this project, since we have converted our 2D images to 3D point clouds, we have used the 3D approach for our anatomical measurements. For the sake of three-dimensional measurements, we need to pick a set of points as our anatomical landmarks on the scapula body. There are fourteen points which are required to calculate a list of essential parameters in this study. Their detailed descriptions are presented in Table 13 and their locations on a left scapula is shown in Figure 49.

Table 13. Description of 14 anatomical points for measurement purposes.

Point Number	Anatomical Point Name	Point Description
P1	Superior border point	The most superior point on the scapula body while facing directly from posterior to anterior.
P2	Inferior border point	The most inferior point on the scapula body while facing directly from posterior to anterior.
P3	Glenoid center point	The center of the best-fitting inferior circle on the glenoid cavity while facing the glenoid from lateral to medial [119].
P4	Trigonum spinae point.	The point on the most medial part of scapular spine located at the intersection of the scapular spine and medial border of the scapular body while facing directly from anterior to posterior.
P5	Superior glenoid point	Position on superior glenoid rim where long head of biceps inserts while facing the glenoid from lateral to medial.
P6	Inferior glenoid point	Position most inferior on glenoid rim while facing the glenoid from lateral to medial.
P7	Posterior glenoid point	Position on posterior glenoid rim at most extreme point of lower width of glenoid while facing the glenoid from lateral to medial.
P8	Anterior glenoid point	Position on anterior glenoid rim at most extreme point of lower width of glenoid while facing the glenoid from lateral to medial.
P9	Acromion tip point_1	The most anterior point at the end of acromion process while facing the scapula from the lateral to medial.
P10	Acromion process point _1	The most inferio-posterior point of the acromion process while facing the scapula from the lateral to medial.
P11	Acromion tip point_2	The most lateral point at the end of acromion process while facing the scapula from posterior to anterior.
P12	Coracoid tip point_1	The most lateral point at the end of coracoid process while facing the scapula from anterior to posterior.
P13	Acromion process point_2	The most posterior-lateral point of the acromion process while facing the scapula from superior to inferior.
P14	Coracoid tip point_2	The most anterior point at the end of coracoid process while facing the scapula from both superior to inferior and lateral to medial.

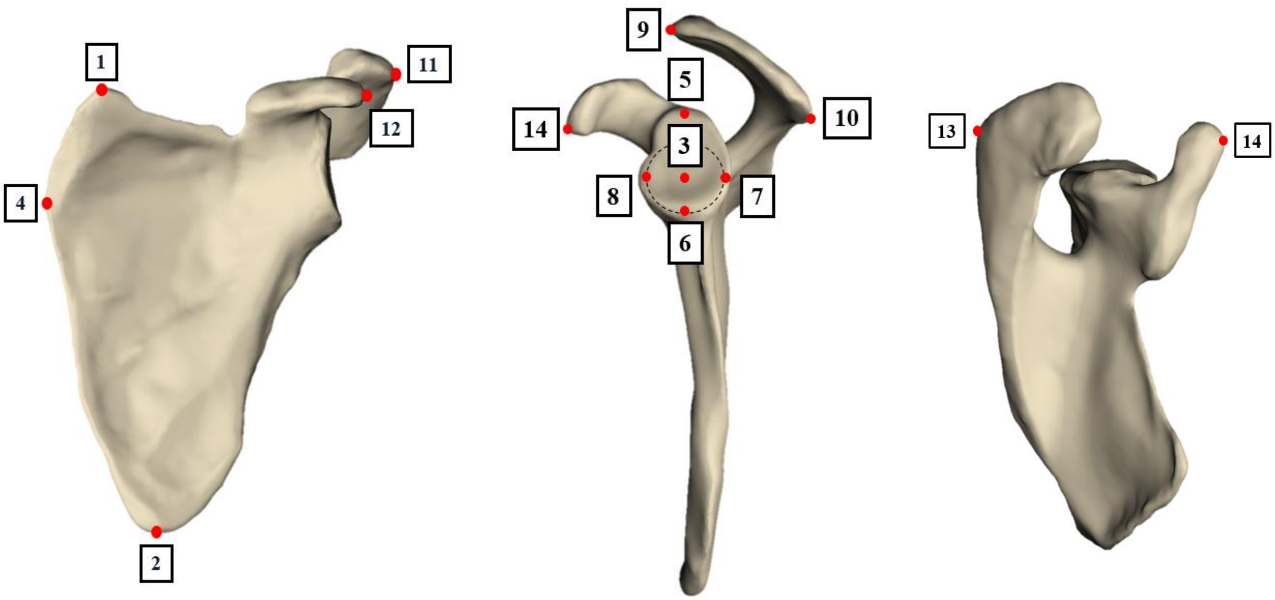

Figure 49. Location of 14 points selected on a left scapula for the anatomical measurements is illustrated in three different views. (a): Anterior view, (b): Lateral view and (c): Superior view.

In this study, these measurements are conducted on 61 scapulae that are representative of a given population of patients. Sixteen anatomic parameters are calculated in different anatomical parts of the scapula including 9 length-related, which are described in Table 14 and also schematically illustrated in Figure 50 and Figure 51. Moreover, 7 angle-related measurements are explained in Table 15 and their schematic illustration are presented in Figure 52 and Figure 53.

Table 14. List of length-related parameters for the anatomic measurements.

Parameter Number	Parameter Name	Parameter Description	Measurement Formula
1	Scapula Height	Distance between the most superior and inferior aspects of the scapula body.	$\lvert\bar{P}_1 - \bar{P}_2\rvert$
2	Scapula Width	Distance between the center of the glenoid and medial end of the spine where it intersects the medial scapular border.	$\lvert\bar{P}_3 - \bar{P}_4\rvert$
3	Glenoid Height	Height of the glenoid cavity along the superior-inferior (SI) direction or Y axis.	$\lvert Y_{P5} - Y_{P6}\rvert$
4	Glenoid Width	Distance between the most anterior and posterior points of the glenoid cavity and which is perpendicular to the SI axis.	$\lvert\bar{P}_7 - \bar{P}_8\rvert$
5	Acromion Length	Length of the acromion process from the anterior apex to the most posterior point.	$\lvert\bar{P}_9 - \bar{P}_{10}\rvert$
6	Lateral Acromion to Glenoid Center Distance	Distance between the most lateral point of the acromion and the center of the glenoid cavity along the medial-lateral direction or Z axis.	$Z_{P11} - Z_{P3}$
7	Coracoid Tip to Glenoid Center Distance	Distance between the most lateral point of the coracoid process to the center of the glenoid cavity along the medial-lateral direction or Z axis.	$Z_{P12} - Z_{P3}$
8	Posterior Inferior (PI) Acromion to Glenoid Center Distance	Distance between the most posterior point of the acromion process to the center of the glenoid cavity along the anterior-posterior (AP) direction or X axis.	$X_{P10} - X_{P3}$
9	Superior Anterior (SA) Acromion to Glenoid Center Distance	Distance between the most anterior point of the acromial tip to the center of the glenoid cavity along the anterior-posterior (AP) direction or X axis.	$X_{P9} - X_{P3}$

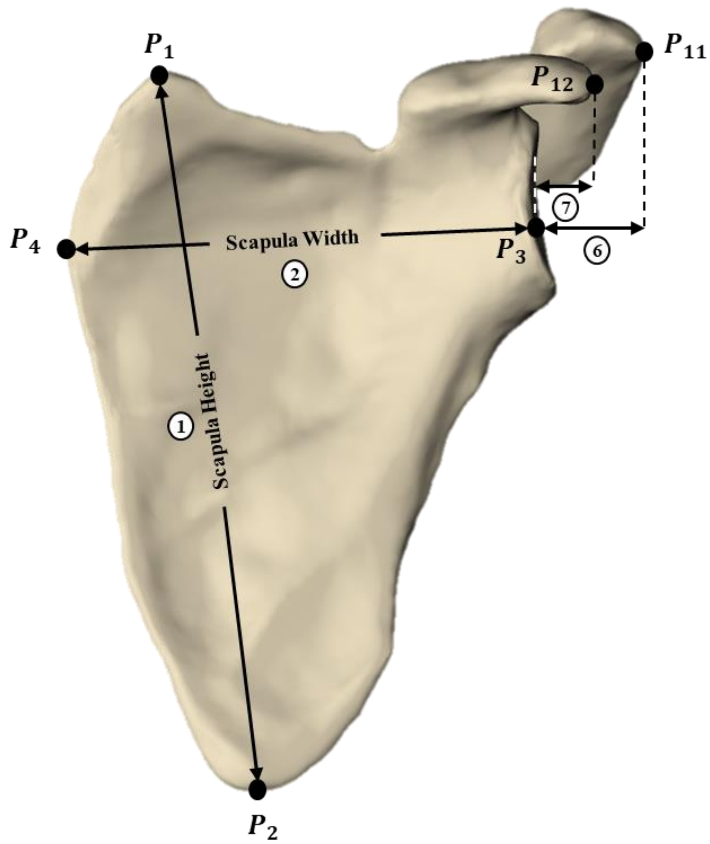

Figure 50. Anterior view of a left shoulder showing measurement parameter 1, 2, 6 and 7.

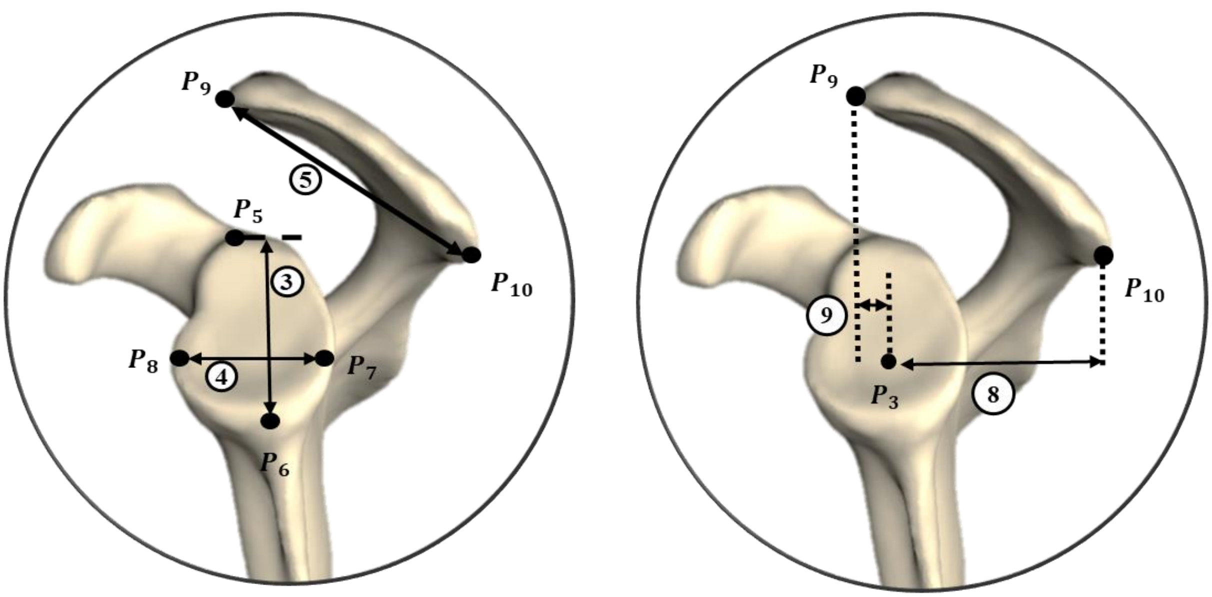

Figure 51. Illustration of lateral view of a left shoulder for measurement parameter 3, 4 and 5 in the left circle and measurement parameter 8 and 9 in the right circle.

Table 15. List of angle-related parameters for the anatomic measurements.

Parameter Number	Parameter Name	Parameter Description	Measurement Formula
10	Fulcrum Axis	Angle between the line connecting the most anterior point of the coracoid to the most posterior-lateral point of acromion and the medial lateral direction or Z axis.	$\cos^{-1}\frac{(\bar{P}_{13}-\bar{P}_{14}).\bar{Z}}{\lvert\bar{P}_{13}-\bar{P}_{14}\rvert}$
11	Inclination Angle	Angle between the superior-inferior (SI) glenoid axis and the medial-lateral direction or Z axis.	$\cos^{-1}\frac{(\bar{P}_{5}-\bar{P}_{6}).\bar{Z}}{\lvert\bar{P}_{5}-\bar{P}_{6}\rvert}$
12	Version Angle	Angle between the anterior-posterior (AP) glenoid axis and the medial-lateral direction or Z axis.	$\cos^{-1}\frac{(\bar{P}_{7}-\bar{P}_{8}).\bar{Z}}{\lvert\bar{P}_{7}-\bar{P}_{8}\rvert}$
13	Acromial Tilt Angle	Projected angle on the sagittal plane (X-Y plane) between the acromion process and the line connecting the most posterior point of the acromion to the most anterior point of the coracoid process.	$\cos^{-1}\frac{(\bar{P}_{9}-\bar{P}_{10}).(\bar{P}_{14}-\bar{P}_{10})}{\lvert\bar{P}_{9}-\bar{P}_{10}\rvert\lvert\bar{P}_{14}-\bar{P}_{10}\rvert}$ $Z_{\bar{P}_9,\bar{P}_{10},\bar{P}_{14}}=0$
14	Critical Shoulder Angle (CSA)	Angle between the SI glenoid axis and the connecting line the most lateral point of the acromion to the most inferior point of the glenoid cavity.	$\cos^{-1}\frac{(\bar{P}_{5}-\bar{P}_{6}).(\bar{P}_{11}-\bar{P}_{6})}{\lvert\bar{P}_{5}-\bar{P}_{6}\rvert\lvert\bar{P}_{11}-\bar{P}_{6}\rvert}$
15	SI Glenoid-Acromion Angle	Projected angle on the sagittal plane (X-Y plane) between the acromion process and superior-inferior (SI) glenoid axis.	$\cos^{-1}\frac{(\bar{P}_{5}-\bar{P}_{6}).(\bar{P}_{9}-\bar{P}_{10})}{\lvert\bar{P}_{5}-\bar{P}_{6}\rvert\lvert\bar{P}_{9}-\bar{P}_{10}\rvert}$ $Z_{\bar{P}_5,\bar{P}_6,\bar{P}_9,\bar{P}_{10}}=0$
16	SI Glenoid-Acromion-Coracoid Angle	Projected angle on the sagittal plane (X-Y plane) between the superior-inferior (SI) glenoid axis and the line connecting the most posterior point of acromion to the most anterior point of the coracoid.	$\cos^{-1}\frac{(\bar{P}_{6}-\bar{P}_{5}).(\bar{P}_{14}-\bar{P}_{10})}{\lvert\bar{P}_{6}-\bar{P}_{5}\rvert\lvert\bar{P}_{14}-\bar{P}_{10}\rvert}$ $Z_{\bar{P}_5,\bar{P}_6,\bar{P}_{10},\bar{P}_{14}}=0$

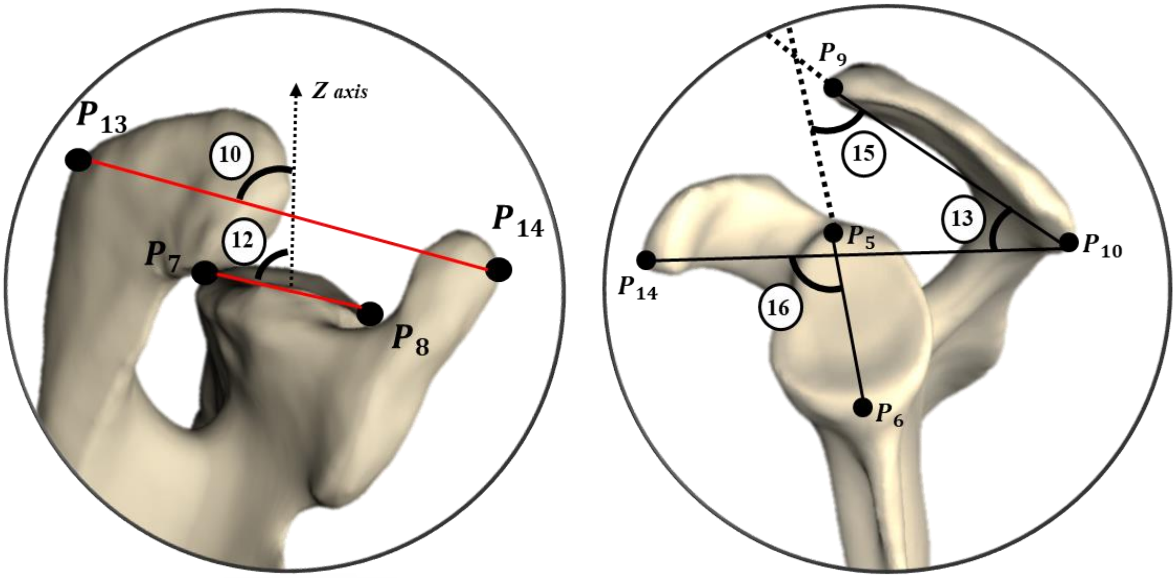

Figure 52. Illustration of superior view of a left shoulder for measurement parameter 10 and 12 in the left circle and lateral view for measurement parameter 13, 15 and 16 in the right circle.

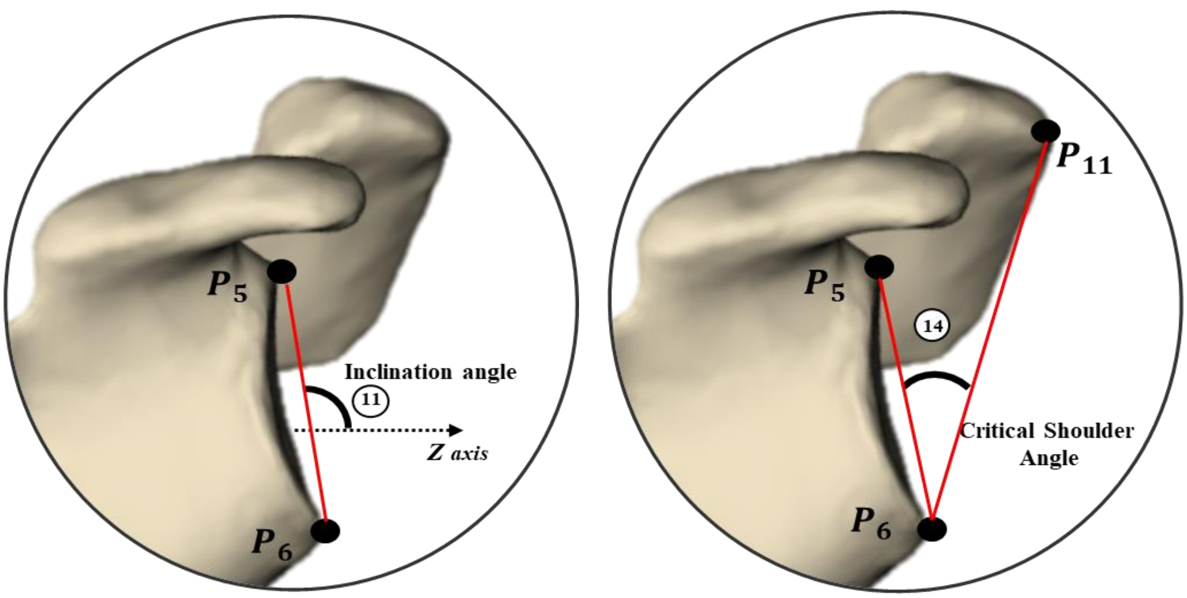

Figure 53. Illustration of anterior view of a left shoulder for Inclination angle (measurement parameter 11) in the left circle and Critical Shoulder Angle (measurement parameter 14) in the right circle.

Sixteen anatomic parameters are calculated in different anatomical parts of scapula included of 9 length-related and 7 angle-related measurements on all 61 models and also on 10K reconstructed shapes which are presented in Table 16. These anatomical measurements are performed on the SSM generated shapes created during the specificity testing in a previous section in order to further validate that the SSM generates shapes with realistic anatomical parameters that are key to the intended orthopaedic planning application. As a reminder, these 10k shapes were generated by using the first nine modes of variation, which accounted for 95% of the variability in our dataset.

Table 16. Average scapular measurement results for 16 parameters.

Parameter number	Parameter name	Average (61 Models)	Average (10k Reconstructed Shapes) *	Unit
1	Scapula Height	**153.47 ± 13.72**	**153.45 ± 13.38**	mm
2	Scapula Width	**104.97 ± 8.85**	**104.98 ± 8.76**	mm
3	Glenoid Height	**39.10 ± 4.93**	**39.07 ± 4.42**	mm
4	Glenoid Width	**31.27 ± 4.32**	**31.13 ± 3.60**	mm
5	Acromion Length	**45.67 ± 5.64**	**45.56 ± 4.88**	mm
6	Lateral Acromion to Glenoid Center Distance	**28.08 ± 5.26**	**28.10 ± 4.89**	mm
7	Coracoid Tip to Glenoid Center Distance	**13.69 ± 4.23**	**13.69 ± 3.13**	mm
8	PI Acromion to Glenoid Center Distance	**37.50 ± 4.54**	**37.49 ± 4.39**	mm
9	SA Acromion to Glenoid Center Distance	**1.79 ± 7.38**	**1.78 ± 7.02**	mm
10	Fulcrum Axis	**87.92 ± 4.22**	**87.84 ± 3.62**	degrees
11	Inclination Angle	**96.13 ± 7.03**	**96.13 ± 3.73**	degrees
12	Version Angle	**102.92 ± 7.59**	**102.79 ± 5.99**	degrees
13	Acromial Tilt Angle	**28.42 ± 4.99**	**28.42 ± 3.56**	degrees
14	Critical Shoulder Angle (CSA)	**34.04 ± 9.58**	**33.95 ± 7.71**	degrees
15	SI Glenoid-Acromion Angle	**53.12 ± 7.72**	**53.18 ± 6.05**	degrees
16	SI Glenoid-Acromion-Coracoid Angle	**98.46 ± 5.06**	**98.40 ± 3.28**	degrees

***10K reconstructed shapes with first 9 modes of variations.**

As described in Table 16, anatomical measurements on the list of 61 scapulae in the dataset are in great agreement with SSM reconstructed shapes which were generated randomly using the first nine modes of variation. This comparison proves that the SSM model built based on 61 scapula models is able to reconstruct fine details of the complex shape of the scapula including reproducing all critical angles and distances between different parts of scapula structure.
Moreover, by comparing the measurement results of eroded scapulae with healthy scapula, it can be noticed that glenoid erosion appeared in greater glenoid version angle (102.92 ± 7.59 ° > 96.2 ± 5.5 °), smaller Fulcrum angle (87.92 ± 4.22 ° < 89.9 ± 5.3°) and larger glenoid width (31.27 ± 4.32 > 29.6 ± 4.0) [120].

5.3.4 Anatomical measurements on SSM results

Anatomical measurements on shapes generated using only 1 of each of the first three modes of variation were conducted to quantitatively demonstrate the independent shape variation represented by each principal mode of variation for ± 2 standard deviation. Required anatomical parameters and related anatomical points are provided in detail in section 5.3.3. It should be noted that the purpose here is not to measure these anatomical values in order to yield values that precisely reflect the population but rather to study to what extent variation of these parameters is exclusively described by one principal mode of variation, which is the fundamental intent of using SSM. If, in the current assessment, the parameters are found to indeed primarily vary with only one principal component, this will indicate two important points of verification:

1. It will further confirm that the required point-to-point correspondence between models in the input model dataset was accurately achieved, as poor correspondence (i.e. cases of the same point representing different anatomy in each model) would result in erroneous data being included in the PCA, which would cause anatomical features to be represented by multiple modes.
2. It will confirm that the SSM is based on a sufficiently large N as an SSM can only have up to one less principal mode as it has observations (i.e. N-1 modes), and too few modes results in each representing multiple forms of variation.

Result of anatomical measurements on first three modes of variation is presented in Table 17.

Table 17. Anatomic measurements on SSM results for the first 3 modes of variation for ± 2 standard deviation.

	Glenoid Height (mm)	Glenoid Width (mm)	Critical Shoulder Angle (°)	Inclination Angle (°)	Version Angle (°)	Acromial Tilt (°)	Scapula Height (mm)	Scapula Width (mm)
Mean shape	**40.05**	**30.95**	**32.99**	**11.10**	**14.64**	**31.09**	**155.27**	**104.63**
Mode 1	40.05±6.51	30.95±5.30	32.99±-5.38	11.10±-1.90	14.64±0.42	31.09±-0.88	155.27±25.96	104.63±15.19
Mode 2	40.05±2.45	30.95±1.57	32.99±-8.21	11.10±-0.08	14.64±5.36	31.09±0.36	155.27±7.00	104.63±-5.87
Mode 3	40.05±3.16	30.95±3.15	32.99±-3.82	11.10±-0.83	14.64±4.01	31.09±-3.45	155.27±2.18	104.63±-4.07

Table 17 presents the anatomical measurements performed on shapes generated using only one of each of the first three modes of variation. The largest deviations in measurements for each mode of variation are marked in red. The first mode of variation, which is representing the size variation, produces by far the largest deviation in scapula height and width. The second mode describes changes in the Critical Shoulder Angle (CSA), with some associated variation in scapula height. Finally, the third mode produces the largest changes in glenoid size and acromial tilt, while not significantly affecting other parameters.

Chapter 6

Statistical intensity modeling

One of the major challenges in joint replacement surgery and the implant design process is the great anatomical variability in human musculoskeletal system. The previous chapters have worked to address one of the most important forms of variation, which is shape, but another critical form of skeletal variation is that of the heterogeneous mechanical properties of bones. Understanding the statistical variation of bone properties continuously across the bone geometry and across the population, can provide critical insights that can improve implant design and methods for patient specific surgical planning. Therefore, the focus of this chapter is the comprehensive study and quantitative analysis of scapula bone mechanical properties.

In previous chapters, we talked about the Statistical Shape Modeling (SSM) in detail. In this chapter, we will discuss Statistical Intensity/Density modeling (SIM)[3]. The are two main differences between SSM and SIM; first of all, the required 3D models for SSM were constructed using surface mesh structures whereas in SIM, 3D volumetric mesh models are required. Second of all, SSM represents variation in shape based on the geometry of a set of input shapes of interest whereas SIM demonstrates how material properties are distributed throughout the population while the variable of interest can be bone density or other material properties. In a nutshell, SIM can quantitatively express bone mechanical property variability by describing and combining the average bone property distribution with the principal modes of variation for the entire population.

---

[3] N.B.: The term SIM and SDM have both previously been used in the literature to denote a model that statistically describes material properties. Density in 'SDM' refers to the fact that the model has been developed using input models where the intensity values (typically in Hounsfield Unit (HU)) of the medical images they are based on have been converted into density units using previously described regressions. Conversely, SIMs represent the actual HU intensity values of the medical images rather than converting to density. In this thesis, the choice to build a model as an SIM rather than SDM was made as the regression equations to convert to density are continually developing in the literature and thus the author felt it more prudent to represent data in base units that can be converted to density when a shape instance is generated based on the latest equations.

6.1 SIM applications

Just as SSMs can be used not only to describe shape variation but also to generate shape instances that can be used in various forms of modeling, SIMs can be used not only to describe material property variation but also to generate bone instances with a specific distribution of properties, which could, for instance, later be used to create a Finite Element Model. Finite Element Analysis (FEA) has been used widely to predict the biomechanical behavior, fracture risk and mechanical performance of bone and various implant designs while considering the bone density distribution [129], [130], [131].

This is traditionally achieved by generating a model from the CT scan of a specific person and thus it is challenging to know whether their results generalize to the population. However, if an FEA model could be generated based on the knowledge of the statistical variation of bone properties in a population, it would be possible to understand the context of the FEA results and generalize them. An SIM provides the information needed to create such an FEA model. The actual creation of FEA models from an SIM is beyond the scope of this thesis.

6.2 SIM requirements

Due to the fact that Statistical Intensity Analysis describes the variation in material properties that change throughout a shape rather than just at its surface, to create an SIM it is necessary to have volumetric mesh representations for all specimens in the dataset. These volumetric meshes are made up of 3D elements rather than 2D triangulated faces as in the case of the inputs used to make an SSM.

Furthermore, unlike the triangulated meshes used in SSM construction in which the relevant information to describe the shape is simply the nodal coordinates, each of the 3D elements that make up a volumetric mesh must have an intensity value assigned to it, which corresponds to the bone property at that spatial location. As a result, the first step to develop an SIM on a desired population is to generate volumetric meshes for each bone in the dataset.

6.2.1 Volumetric mesh generation

Volumetric meshes are constructed using volumetric tetrahedral elements of the same type used in the creation of 3D Finite Element Analysis models. Furthermore, in order to statistically analyze the intensity variation throughout the population, each volumetric mesh must have the same nodal structure. In other words, each volume mesh should have the same number of nodes with the same number in each model located in the same location, which is known as correspondence.

In the previous chapters discussing SSM construction, this correspondence is achieved for surface models by using a mesh morphing algorithm (i.e. non-rigid registration algorithm) and choosing one surface mesh as a source (i.e. an atlas that is applied to all other models) to deform it to the shape of each scapula model in the dataset, while keeping the nodal structure. In the case of SIM, the task of creating corresponding volumetric meshes is significantly more challenging than the analogous task for creating an SSM using mesh morphing. This is because each of the surface meshes undergoing mesh morphing in the SSM construction process have a clearly defined surface geometry. However, in the case of the volumetric correspondence problem, the volume mesh also includes elements that are entirely located within the interior of the shape, which is amorphous and thus does not have unique features to assist with mesh morphing.

Fortunately, an SIM is normally developed in conjunction with an SSM, and the prior knowledge gained from making the correspondence surface models for the SSM can be used to guide the creation of corresponding volumetric meshes for all scapulae in our population. This can be achieved by using a finite element analysis-derived volumetric mesh deformation process and a volume source mesh that has the exact same nodal structure on its outside surface as the surface source mesh used to create the SSM.

6.2.1.1 Volumetric mesh algorithm requirements

The initial requirements to create a volumetric mesh algorithm are as follows:

- **Model 1:** The surface source mesh used in the SSM.
- **Model 2:** A volumetric source mesh with the exact surface geometry and nodal structure of the surface source mesh but filled with volume elements.
- **Model 3:** A set of correspondence surface meshes of all other scapulae used to create an SSM.

6.2.1.2 Volumetric mesh algorithm steps

Model 1 and each of the models of type 3 above have the same surface nodal structure, therefore the distance between each point of model 1 and its corresponding point in each model 3 instance can be easily calculated by subtracting the nodal coordinates of source points from target points (e.g., node 1 in model 1 from node 1 in one of the type 3 models). This will show how far each node in the source surface mesh was shifted to produce the same geometry as the current model 3 instance (see schematic in Figure 55).

Since the model 2 volume mesh has the same surface nodes as our surface source mesh (i.e. model 1), the amount of deformation needed for each of the nodes on the outer surface of the volume mesh in order to match the model 3 meshes is known as described in the above paragraph but finding a method to deform the internal volumetric nodes in such a way that anatomical correspondence is achieved for each of the bones that make up the dataset is needed. This problem can be solved using the Finite Element Method (FEM) since this approach is intended for volumetric meshes. The main steps of this algorithm can be divided into three steps as follows:

- **Surface mesh distances:** At the beginning of this process, the aforementioned nodal distances between the source surface mesh (i.e. model 1) and one of the correspondence surface meshes (i.e. an instance of the model 3 type) are calculated. A schematic view of this distances is shown in Figure 55.
- **Displacement boundary conditions:** The calculated distances for all of the surface nodes can be treated as a set of displacement boundary conditions for all nodes on the outside surface of the volumetric source mesh (i.e. model 2).
- **Mesh morphing simulation:** A simulation using the set of boundary conditions and treating the volumetric mesh as a finite element model, can be run that calculates the deformed position for each internal node of the volume source mesh that satisfies the applied boundary conditions. Because of the inherent connectivity of the volumetric mesh and the formulation of finite element problems as finding the solution that minimizes potential energy, the anatomical location of each internal node is maintained thus yielding a volumetric mesh that matches the target geometry while maintaining volumetric correspondence to the source mesh. It is this correspondence characteristic

that enables the material property variations to be described in a systematic manner that can be used to create a SIM.

The aforementioned algorithm is adapted from a method described by Soltanmohammadiet al. at J.Biomech.Eng.2020 which is a mesh morphing algorithm implemented in an FEM software (ABAQUS) [132].

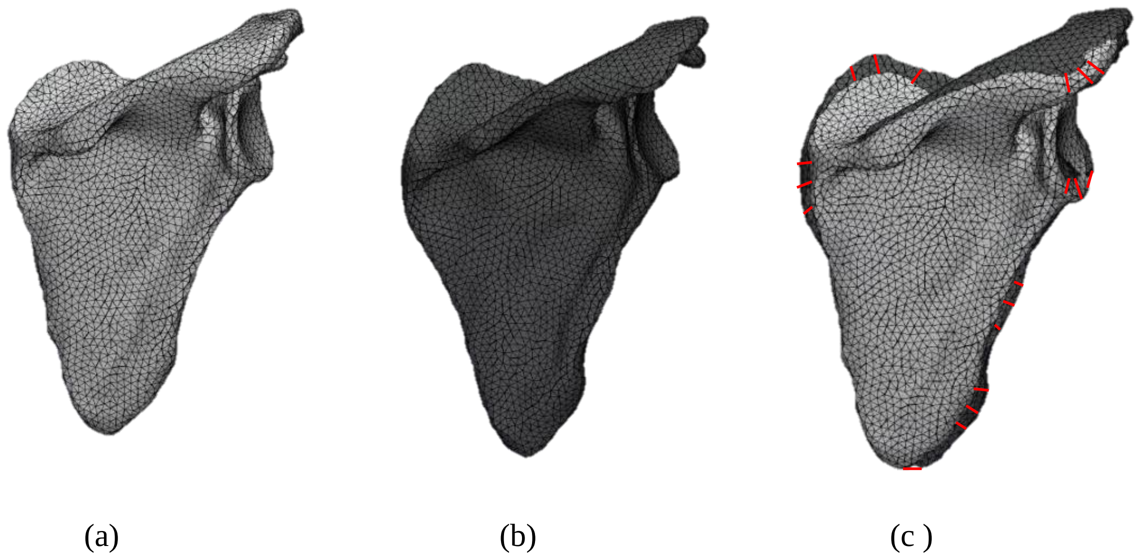

Figure 54. Schematic view of surface mesh distances from source mesh (a) to each deformed mesh (b) which are representing target shapes as indicated by the example set of red lines in (c).

6.2.1.3 Source volumetric mesh information

The 3D mesh structure of the source volume mesh is created in Gmsh software based on the associated source surface mesh (with 119,537 surface nodes as described in Chapter 2) that is used to create the SSM. Gmsh is an open source 3D finite element mesh generator that provides fast and user-friendly meshing tools and advanced visualization capabilities [133]. It should be noted that to create 3D volumetric mesh from surface mesh of source model, an STL file of the surface structure with the correct coordinate system is imported in Gmsh software which is shown in Figure 55.

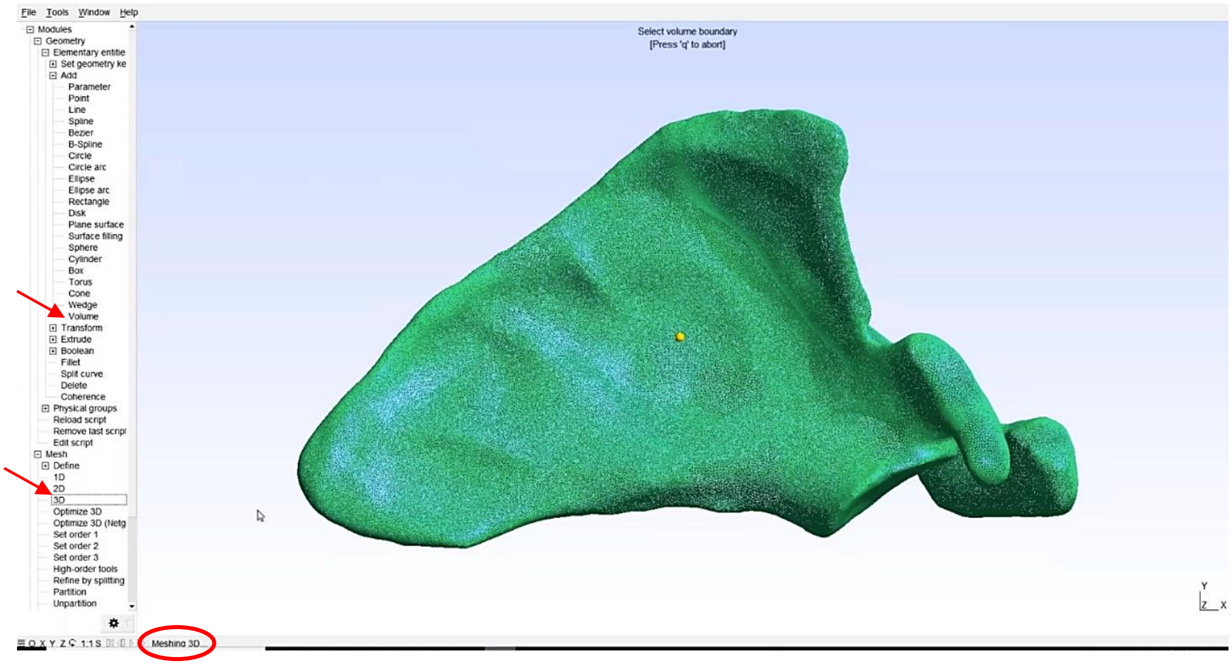

Figure 55. Illustration of Gmsh software workspace which is used to generate 3D volumetric mesh structure from surface mesh of source model.

Specifically, the surface nodes of the source surface mesh are used as seed points for the generation of a linear tetrahedral volumetric mesh. The key property of the volumetric mesh is to limit the element maximum edge length to 0.7 mm to achieve a fine mesh quality. This resulted in a mesh structure with 1,144,301 spatial nodes and 244,735 tetrahedral elements.

6.2.2 Material property assignment

The purpose of SIM is to represent the material property distribution in a group of bones. Thus, after volumetric mesh structures of all scapulae in the dataset are created using the Finite Element approach, it is necessary to then assign material property values to all volumetric elements. The material property data in this study is driven from the CT images of each scapula model in the dataset using Hounsfield Unit (HU) values which is explained in detail in the next section.

6.2.2.1 Hounsfield unit

These are relative scalar units used in grayscale CT images to describe CT numbers in a standard form. This scale with a total 4096 values (12 bit) is started from black (-1024 HU) to white (3071 HU). The black color is calibrated to represent air and white for the densest tissue in a human body (tooth enamel). An HU value of zero corresponds to water. Accordingly, tissues which are denser than water get positive values and those with less density get negative values. For instance, fat is approximately -100 HU, muscle ~100 HU and bone has a range between 200 HU for trabecular bone to about 2000 HU for cortical bone. Finally, the maximum HU is assigned to metal components of implants which is 3071 HU. This scale of Hounsfield unit values are shown on an example CT scan image of the shoulder girdle in Figure *56*.

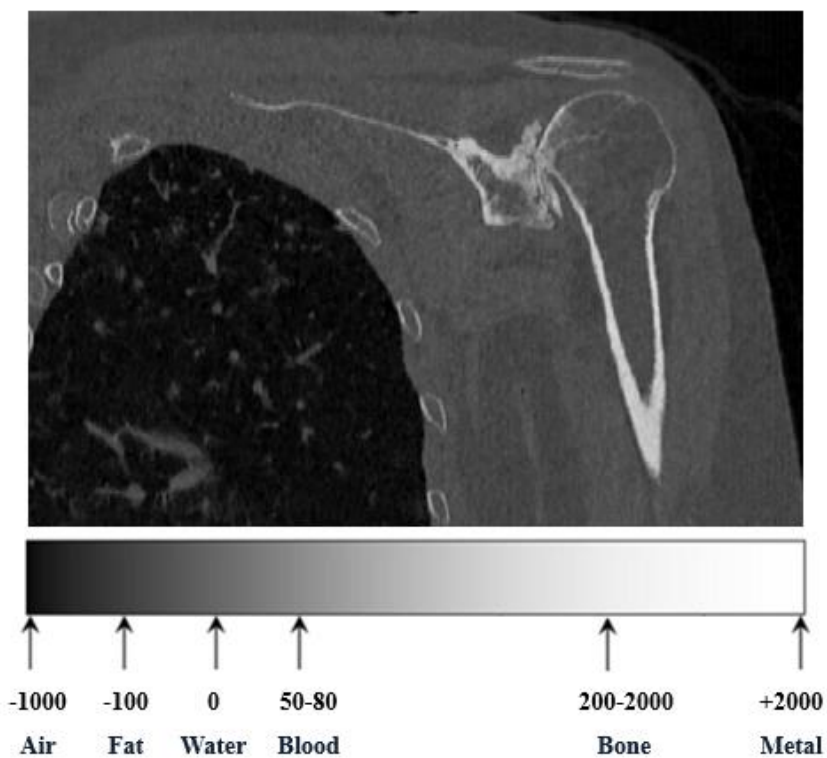

Figure 56. *Hounsfield scale showing corresponding CT numbers for different substances.*

6.2.2.2 Bone property assignment steps

The output of volumetric mesh morphing algorithm is a 3D volumetric mesh structure in .VTK format which needs to be used in bone property assignment process. As bone property data can only be derived from CT images, volumetric mesh models should be imported into Mimics software using the .INP format. However, it should be noted that the coordinate system of the volumetric mesh models are similar to their corresponding surface meshes that were previously defined in the pre-processing step of the proposed NRICP algorithm in chapter 3. As a result, volumetric mesh models cannot be directly imported into Mimics software for material property assignment due to the differing coordinate system of the CT images. For that reason, the following steps were applied on the output files to convert the .VTK file to a usable .INP file for Mimics software:

1. Convert volumetric mesh model from .VTK to .INP using meshio which is an open source Python code [134].
2. Define surface mesh for the 3D volumetric mesh (.INP format) in Abaqus software using corresponding deformed surface mesh which was already generated by the proposed NRICP algorithm in chapter 3 (see Figure 57) and export the modified mesh as an .INP file.
3. Import the combined volumetric and surface mesh .INP file into the 3-matic software (a companion software to Mimics) as well as importing the corresponding surface mesh from Mimics software with the original coordinate system.
4. Use alignment tools (N-point registration module) in 3-matic to align the volumetric mesh to the original surface mesh (see Figure 58 and Figure 59).
5. Export volumetric mesh with corrected coordinate system from 3-matic to Mimics software (see Figure 60).
6. Use material assignment module in Mimics software (see Figure 61) to assign bone property to the volumetric mesh model.
7. Perform a HU calibration by reading HU values of different materials such as: air, cortical bone, fat, blood and muscle from CT images of each model in Mimics software (see Figure 62 and Figure 63) and using expected HU values of -1000 HU for air, 1200 HU for cortical bone, -100 for fat, 20 HU for blood and 30 HU for muscle. A regression can then be calculated including the slope of this line (m in Figure 61) along with the intercept (b in Figure 61), and be applied tothe material assignment window (see Figure 61).
8. Export the result in .CSV file which contains the HU value of each node per coordinates in the volumetric mesh model.

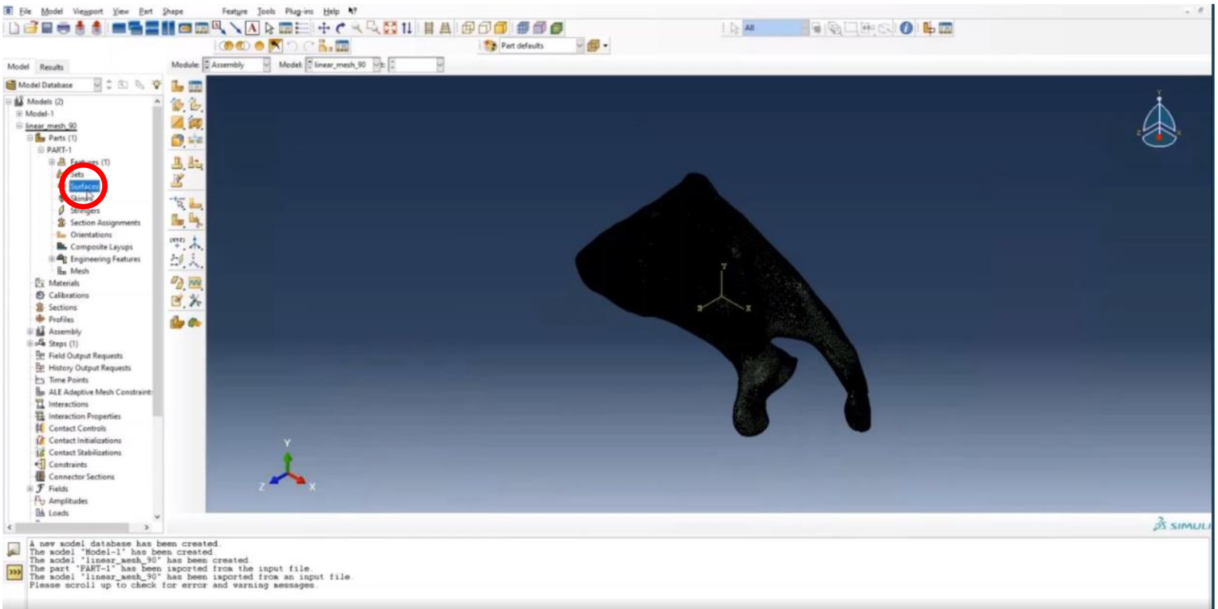

Figure 57. Define deformed surface mesh for the corresponding 3D volumetric mesh in Abaqus software.

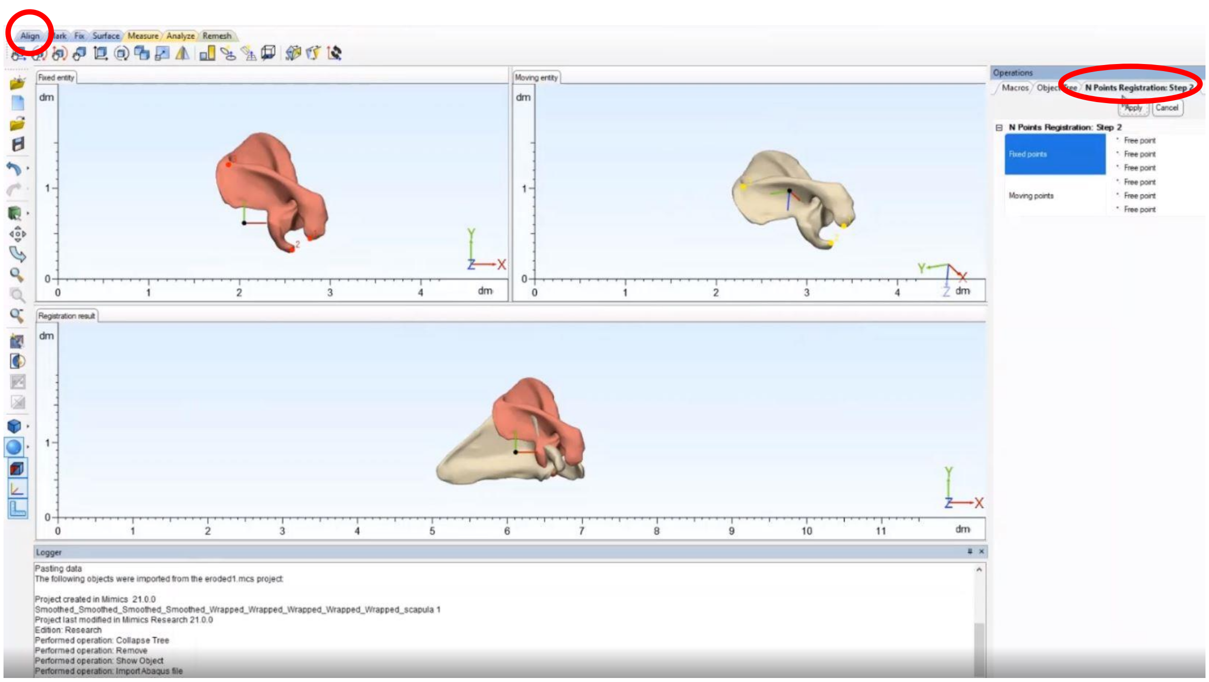

Figure 58. Before rigid alignment of volumetric mesh exported from Abaqus to original coordinate system of corresponding surface mesh exported from Mimics using alignment tools in 3-matic software.

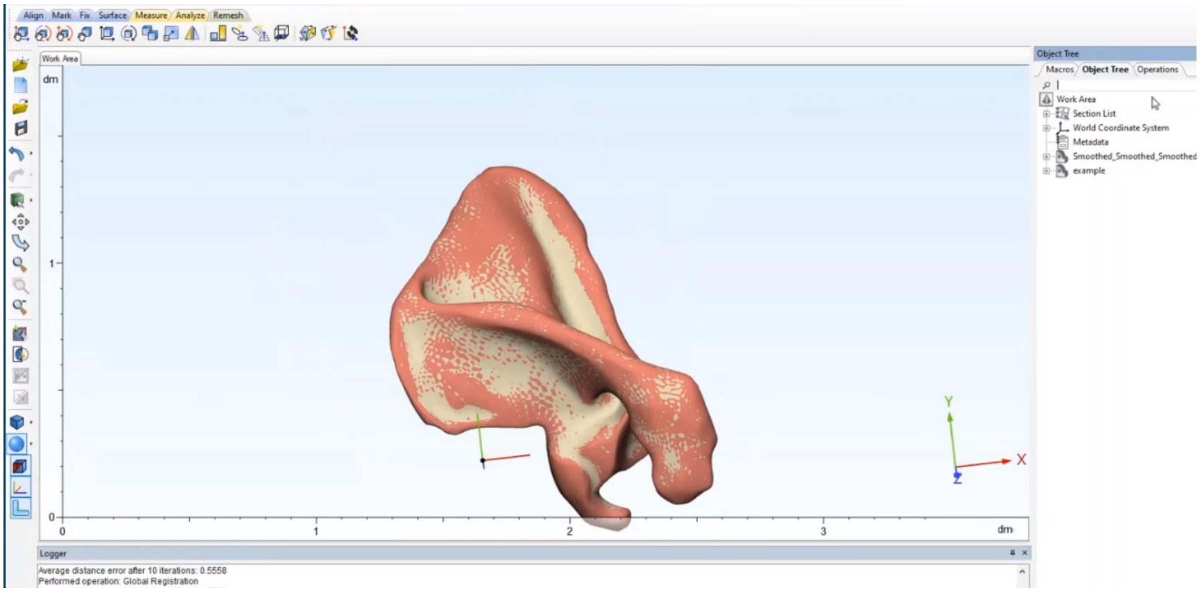

Figure 59. After alignment of volumetric mesh to corresponding surface mesh in 3-matic.

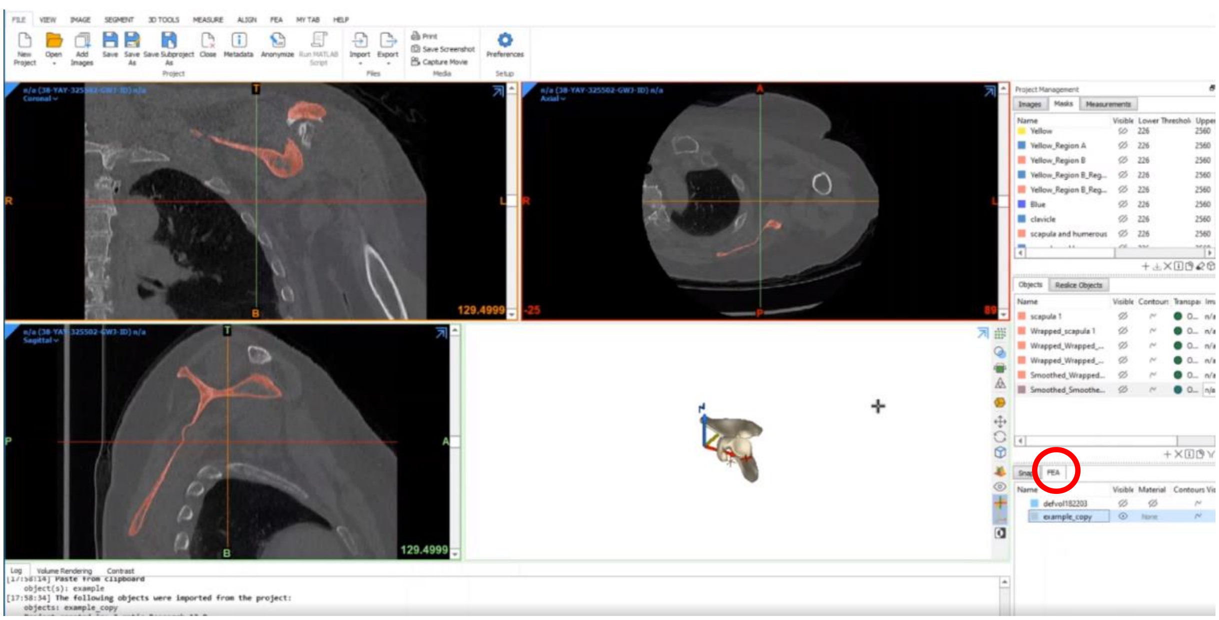

Figure 60. Volumetric mesh model in INP format corresponding to CT images imported in FEA section of Mimics software.

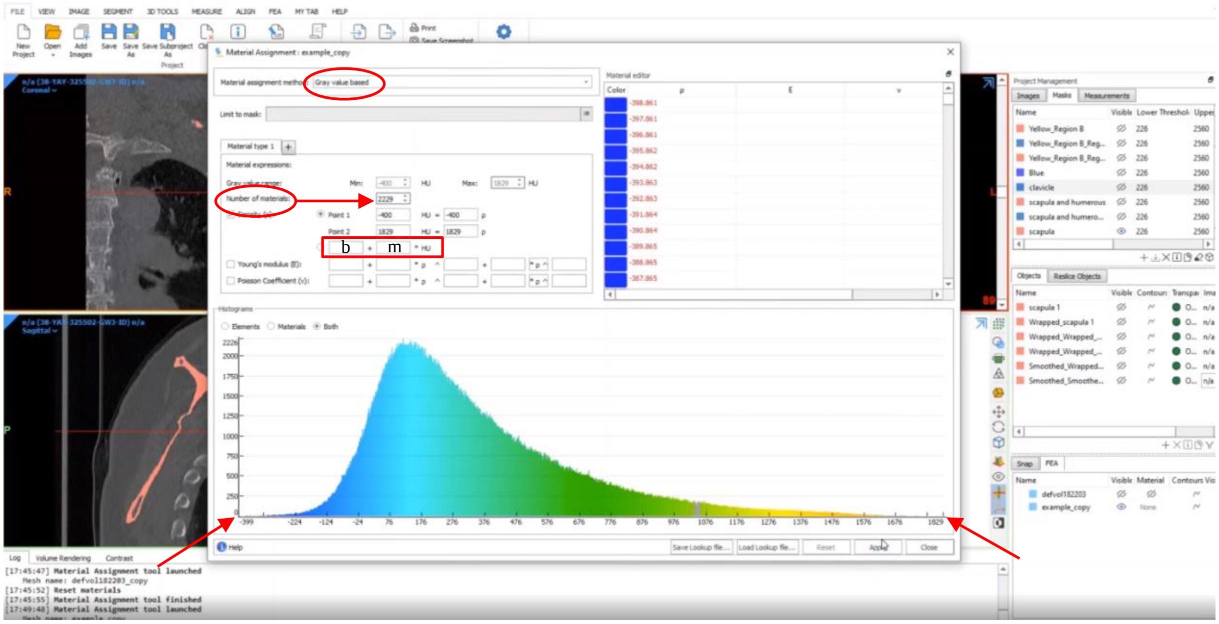

Figure 61. Material assignment using gray value based method in Mimic software used to assign bone properties from CT images to corresponding volumetric mesh model (m and b are the slope and intercept of regression line for HU calibration).

Figure 61 shows the material assignment module in Mimics software for one example from the dataset using the gray value based method. In this scapula model's histogram, the x-axis shows the gray value range which is started from -400 HU to 1829 HU (see arrows in Figure 61) for this bone and y-axis shows the total number of voxels with corresponding HU values. By choosing 2229 (400+1892) as the number of materials in this case, each material type will get a separate and unique HU value. This process should be repeated for each model in the dataset in order to properly assign the bone property to the volumetric meshes based on the associated CT scan.

In this study, the described calibration method based on measured material property of biological tissue samples is applied on the HU values extracted from the Mimics software for each scapula model in our dataset [135]. This is not meant to convert HU values to density, but rather to act as an exact HU unit calibration since clinical CT scans almost never include a discrete, standardized calibration phantom. A conversion to density can be applied at a later date using the most current regression in the literature.

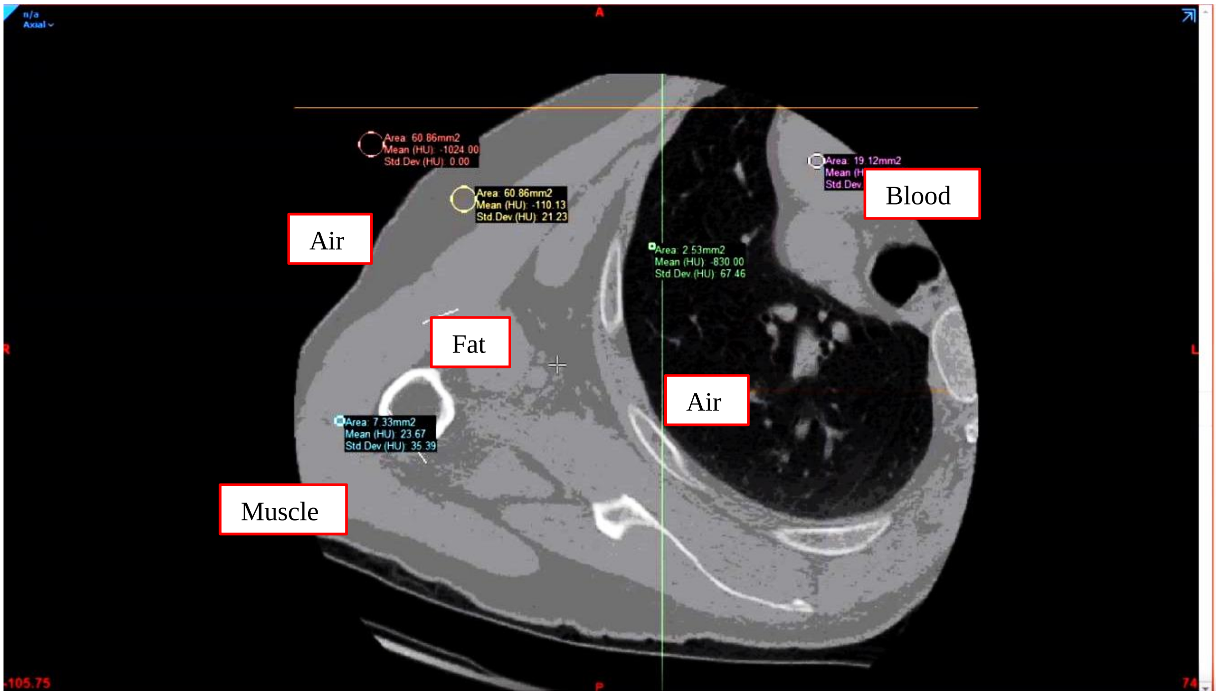

Figure 62. Illustration of calibration step in Mimics software to capture HU values of different materials on one CT slice.

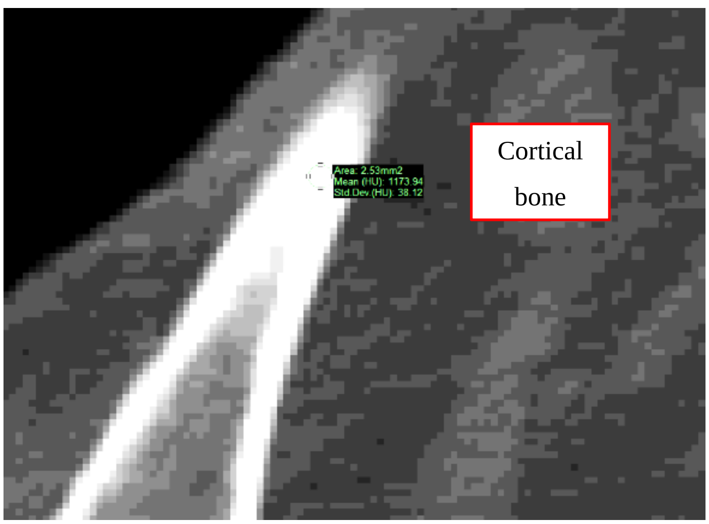

Figure 63. HU value reading from cortical bone in one CT slice for calibration step.

6.3 SIM generation

Once volumetric models of all scapulae with material properties overlaid on their corresponding nodes are ready, an SIM can be created by performing PCA, which is previously described in detail in chapter 4, on the material properties of all nodes for the 61 specimens in our dataset. Since HU values are used as the material property of bone in this study, SIM should be created from the list of HU values which is called as intensity values and it is shown in Eq. (43). Therefore, mean intensity over 61 models in the dataset is calculated by averaging the HU value of each node from the list of 1,144k nodes in each model and it is presented in Eq. (44).

$$I = [HU_1, HU_2, \dots, HU_{vn}]^T \quad (43)$$

$$\bar{I} = [\overline{HU}_1, \overline{HU}_2, \dots, \overline{HU}_{vn}\ ]^T \quad (44)$$

$$\overline{HU}_{vn} = \frac{1}{N}\sum_{j=1}^{N}(HU_{vn})_j \quad (45)$$

Where *I* is the intensity matrix of *HU* values for all the nodes in each volumetric mesh which is a *vn* by 1 matrix, *vn* is the total number of nodes in each volumetric models which is identical for all models (*vn*=1,144k), $\overline{HU}$ is the average *HU* calculated for each node between all models (*N*=61), and $\bar{I}$ is the mean intensity matrix of all models in the dataset which is also a *vn* by 1 matrix. Therefore the covariance matrix for the intensity dataset can be written as Eq.(46):

$$Cov(I) = \frac{1}{N-1}\sum_{j=1}^{N}\left(I_j - \bar{I}\right)\left(I_j - \bar{I}\right)^T \quad (46)$$

As a result, this translates into a very large covariance matrix (*vn* by *vn*) and yields a computationally challenging problem. As it was mentioned earlier in chapter 4, the computation problem can be overcome through mathematical manipulations that restate the problem in a simpler form. A smaller matrix *D*, which has *N*×*N* dimensionality, can be computed instead of the covariance matrix of *I* and calculation of its eigenvectors and eigenvalues is feasible. Matrix *D* can be computed by Eq. (47):

$$D(I) = \frac{1}{N-1}\sum_{j=1}^{N}\left(I_j - \bar{I}\right)^T\left(I_j - \bar{I}\right) \quad (47)$$

Then eigenvectors and eigenvalues of the matrix *D* can be calculated by Eq.(48):

$$D\ \psi = \gamma\ \psi \quad (48)$$

Where ψ are the eigenvectors and γ are the eigenvalues. After some simple algebra, the eigenvalues (λ) and eigenvectors (φ) of the initial covariance matrix of *I* (*vn* by vn*)* can be found as in Eq.(49), and the detailed calculation is attached in the Appendix A:

$$\varphi = \frac{1}{\sqrt{\gamma}}(I - \bar{I})\psi \qquad (49)$$

$$\lambda = \gamma$$

A new intensity model as described earlier in the chapter 4 for SSM, can be constructed through linear combination of the first c modes of variation as shown in Eq.(50):

$$I_i = \bar{I} + \sum_{m=1}^{c} \varphi_m b_m \qquad (50)$$

Where $\bar{I}$ is the mean intensity distribution, *m* is the number of mode of variation, c is the total number of modes that new intensity models need to be reconstructed with (i.e., it can be a number from 1 to total number of scapulae minus one), φ_m is the corresponding eigenvector and b_m represent the weight for mode m. It means that each new intensity model is reconstructed by adding weighted eigenvectors to the mean intensity distribution matrix. A method to constrain the weight parameter to avoid unrealistic shapes is to lie b_m inside $[-3\sqrt{\lambda_m}, \sqrt{3\lambda_m}]$ which allows the weights to be in the range of plus or minus three standard deviations, in that case the SIM can capture more than 99% of the variation. It should be noted that as this equation is a linear combination of different modes, new intensity models can be reconstructed using individual modes of variation (i.e., using m=1 or 2 or 3, etc.) as well as linear combination of different modes.

To rewrite the previous equation using eigenvectors and eigenvalues for generating new intensity models, the reconstructed intensity model can be described as I_i in Eq. (51):

$$I_i = \bar{I} + \sum_{m=1}^{c} \alpha_i \sqrt{\lambda_m} \varphi_m \qquad (51)$$

Where φ_m is the m^{th} eigenvectors, λ_m is the m^{th} eigenvalues and the α_i coefficient is the standard deviation which is a standard normal distribution with zero mean and unit variance ($\alpha \sim N(0,1)$) that can be either a positive or a negative value [102], [111].

6.4 SIM results

PCA is applied to the volumetric models in order to create an SIM of the entire scapulae to explore the intensity variability throughout the population. To represent the intensity values on each node, the mean scapula shape from the SSM is used and a volumetric mesh is created for that mean shape. Then calculated HU values resulting from the PCA and reconstruction equation (Eq. (51)) are assigned to each node and heat maps of the HU values are created using ParaView software (an open-source software for data analysis and visualization application [136]), to show the intensity variation in several cross sections of the mean scapula.

The first three main modes of variation are described by perturbing the mean intensity by ± 2 standard deviations of each principal component and the SIM results of only first three modes of variation on 3 different cross sections (sagittal, frontal and axial) are presented for illustrative purposes in Figure 64, Figure 65 and Figure 66.

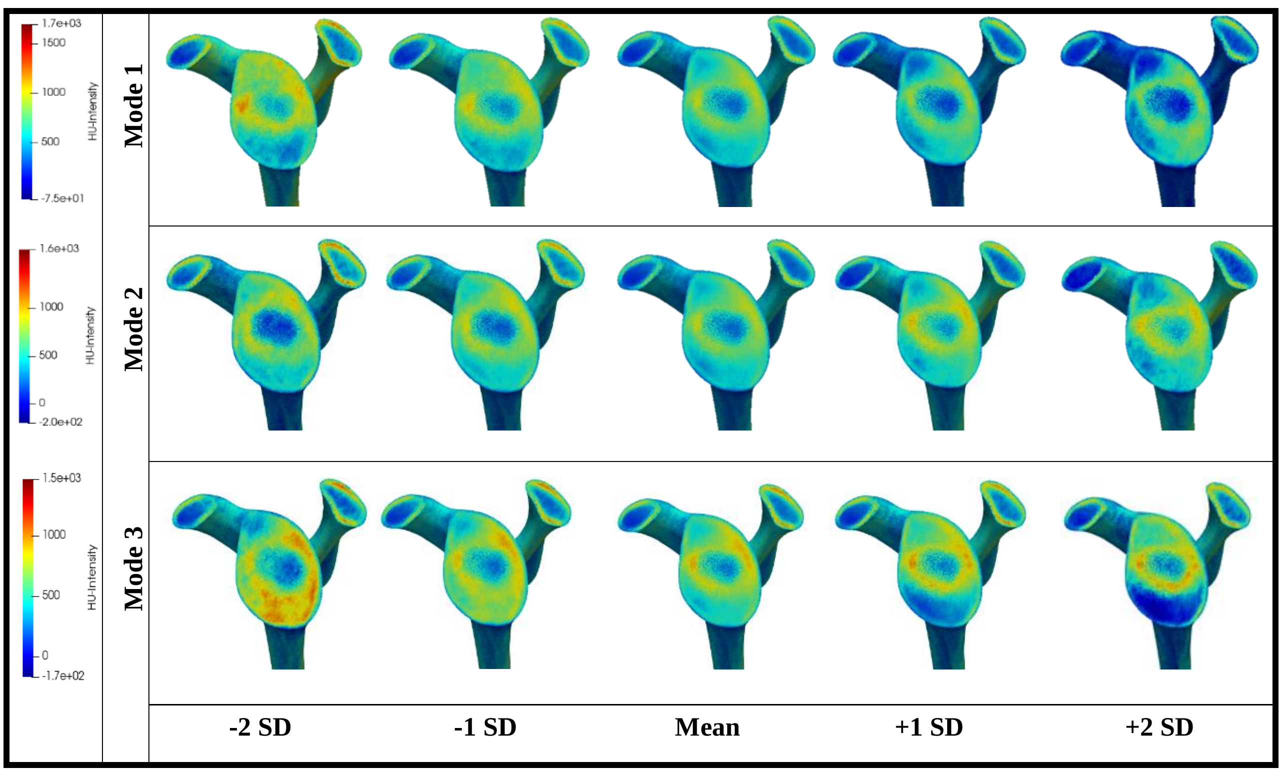

Figure 64. HU-Intensity distribution on sagittal section of glenoid cavity for first three modes of variation.

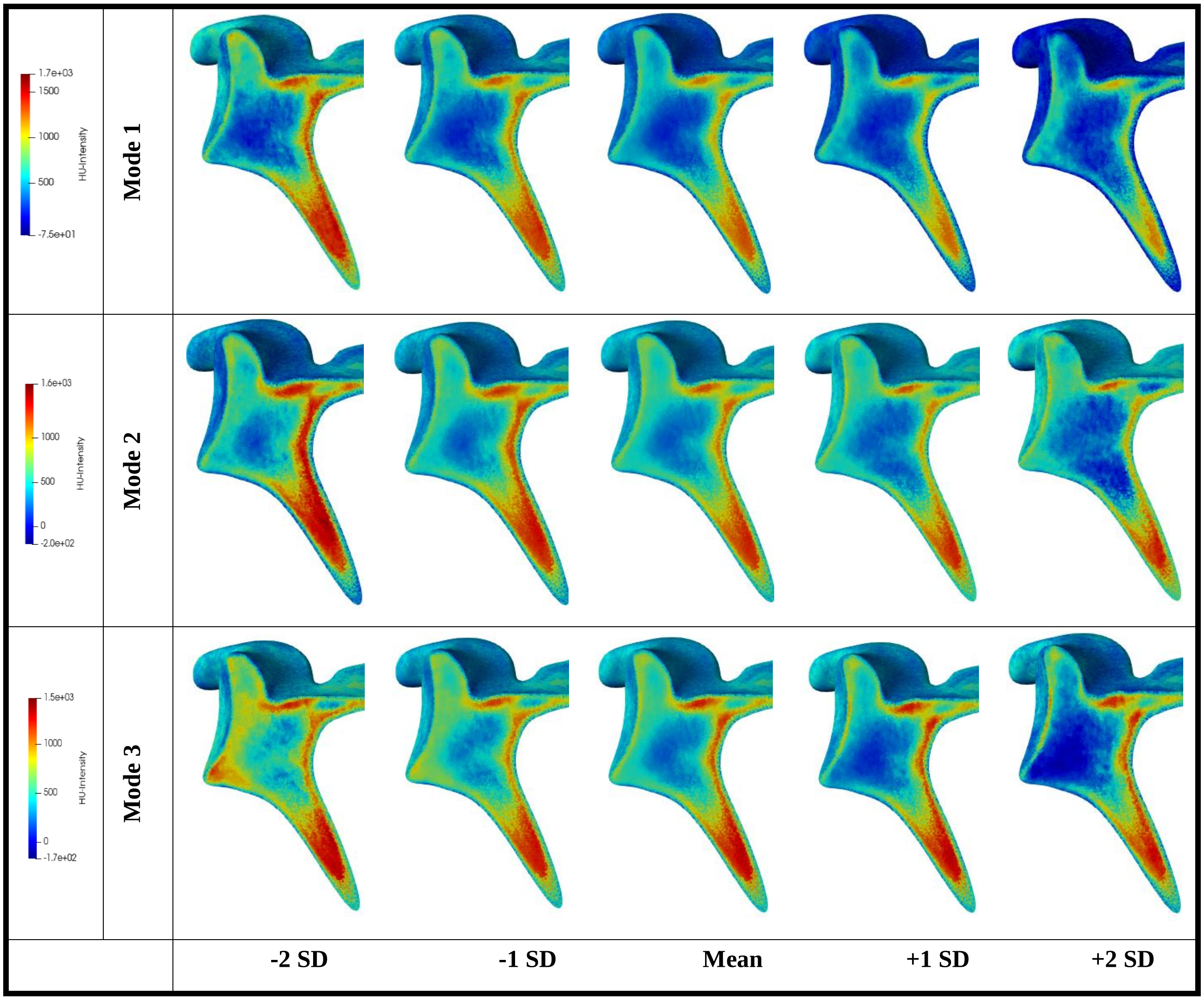

Figure 65. HU-Intensity distribution on frontal section of scapula at the origin of glenoid center for first three modes of variation.

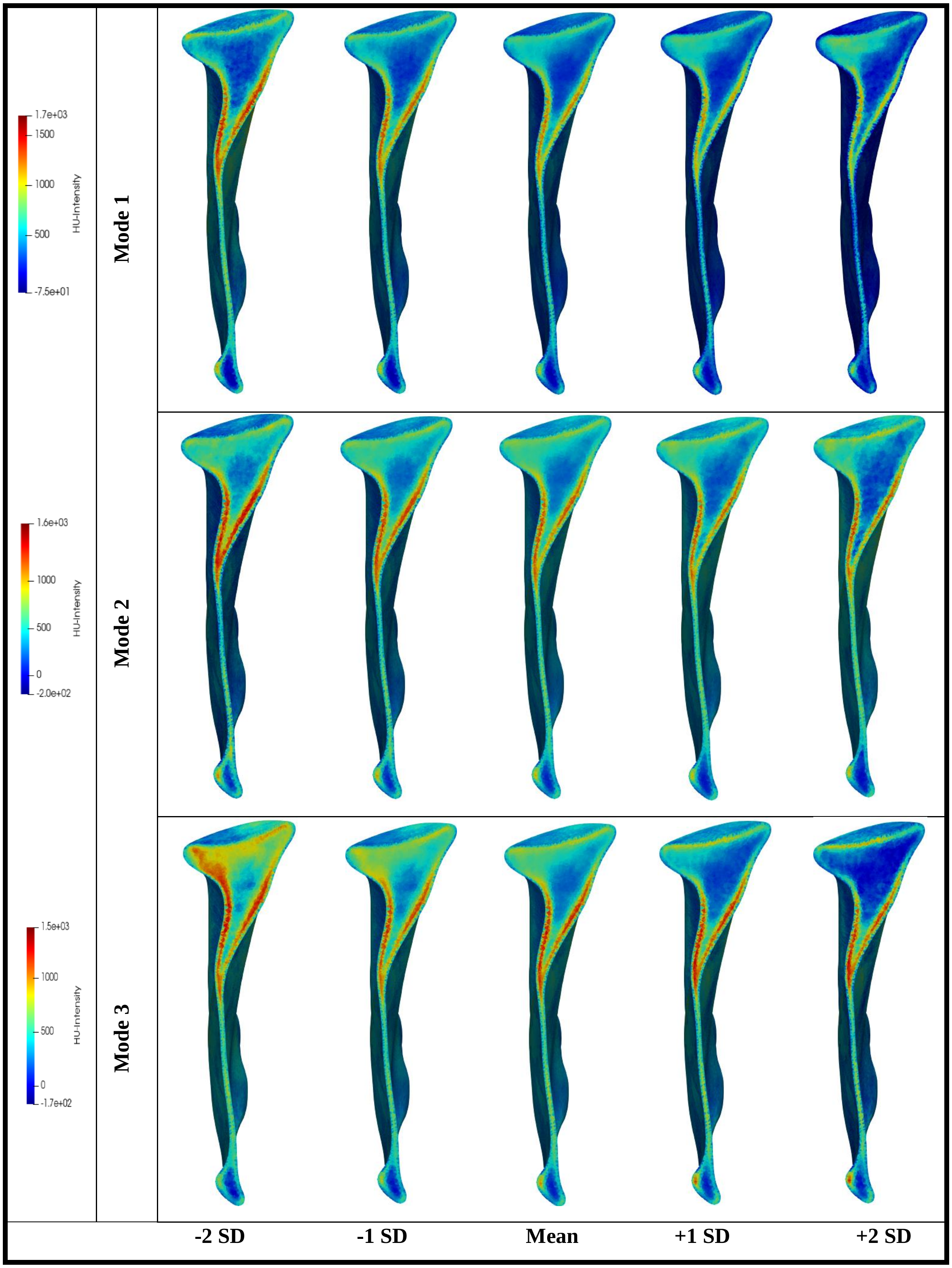

Figure 66. HU-Intensity distribution on axial section of scapula at the origin of glenoid center for first three modes of variation.

The SIM developed on 61 scapular bones, has shown that the first mode of variation accounts for overall changes in intensity across the entire bone (mean±1SD of entire shape: 456.8±108.7 HU), while the second mode represents localized changes in the glenoid vault bone quality (mean±1SD of representative node: 316.9±69.2 HU). The third mode shows changes in intensity at the posterior and inferior glenoid rim associated with posteroinferior glenoid rim erosion (mean±1SD of representative node: 599.4±188.3 HU).

The bone intensity distributions associated with the third mode of variation revealed differences in the intensity of the posteroinferior glenoid rim compared to the anterosuperior glenoid rim, which could help in identifying the critical regions of the scapula anatomy when designing shoulder implants for patients with erosion. The glenoid cavity is the main region of interest in shoulder implant design and loosening of these implants is still the main problem in shoulder arthroplasty [137], [138]. Specifically, the quality of bone surrounding the shoulder implant fixation in the glenoid region plays an important role in implant loosening, which then impacts natural biomechanics of glenohumeral joint in the patient [139].

Scapula shape and glenoid orientation data from SSM in a group of patients who were treated by shoulder arthroplasty can support implant design and sizing while bone intensity distribution can help in fixation design, screw orientation and placement. As bone intensity in the posteroinferior glenoid cancellous bone of mode 3 is less than other regions (see Figure 65) this suggests that avoiding fixation in this region and preferentially placing screws in the anterosuperior region of the glenoid may yield improved implant fixation.

In addition, to assess the quality of the SIM, its compactness is calculated using the same method as described in chapter 5 including SIM compactness for different number of modes (Figure 68).

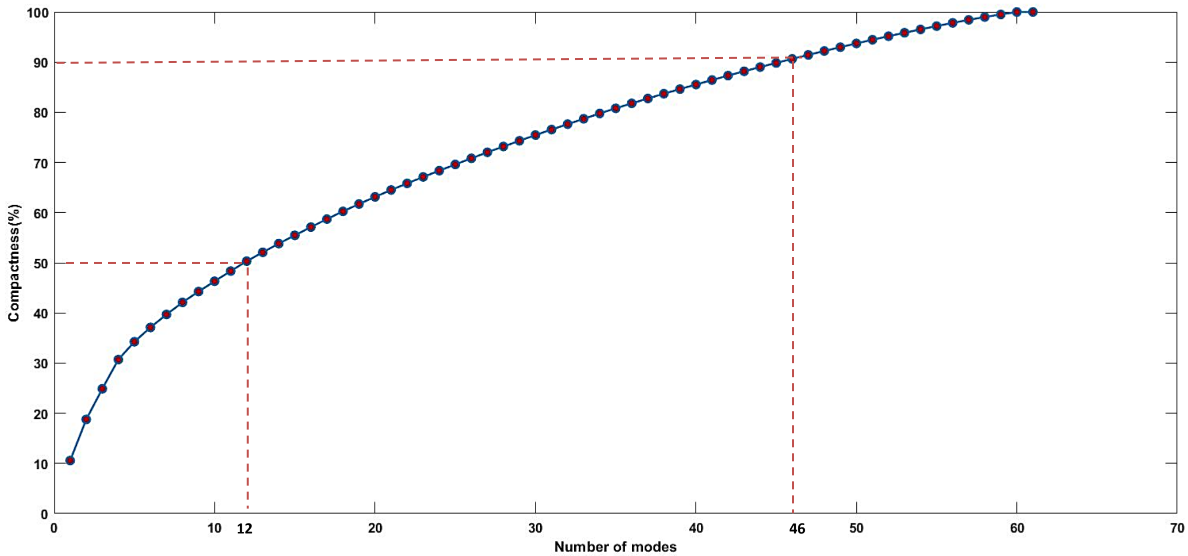

Figure 67. SIM compactness results by modes of variation.

This compactness evaluation on the SIM shows a much lower percentage of the variation in bone property distribution is captured by the first mode of variation as compared to the first mode in the SSM. This is not surprising as there is no obvious dominant factor that disproportionately affects bone intensity distribution as size does when it comes to shape variation. Thus, many more modes of variation must be used to represent a high proportion of the variation (e.g. 12 modes for 50% and 46 modes for 90%).

The SIM results show regional variations in intensity characteristic of a glenoid erosion patient population. Capturing these variations in bone properties indicate that this SIM could act as a validate source for the generation of Finite Element models with systematically varied bone properties, which can produce results that better inform our understanding of the biomechanics of various treatment options for patients with glenoid erosion. Additionally, one of the main strengths of this SIM study is its use of volumetric mesh models for all scapulae which enables Finite Element modeling to be used in evaluation and assessment of implanted bones in the future.

Chapter 7

Conclusion

The shoulder joint is a complex structure to manage both clinically and computationally. Clinical and surgical understanding of shoulder function before and after intervention leads to successful outcomes and pain free shoulders. State-of-the-art techniques used in medical imaging, machine learning, and musculoskeletal modeling can provide such an understanding or efficacy to a certain extent. However, these techniques do not individually excel in completely understanding the morphological and biomechanical aspects of the shoulder joint. Thus, new pathways must be established either by adapting existing approaches from disparate fields or by devising completely new techniques.

In this thesis, I had set my research aims towards the goal of building a combined framework of two research domains: Statistical Shape Modeling (SSM) and Statistical Intensity Modeling (SIM) to investigate the shape morphology and material property variation of eroded scapulae of patients who were treated by RTSA.

7.1 Summary

A better understanding of how the shape and intensity of the shoulder vary among members of a population can help design more effective population-based orthopedic implants. The objectives of this study were to develop SSMs and SIMs for the shoulder serving as tools to describe the main modes of variability in the shape and intensity distributions of bones within the population of interest expressed as a set of parameters called Principal components or main modes of variation.

The first chapter provided thorough details about shoulder anatomy, glenoid erosion and shoulder arthroplasty as well as motivation and objectives that led this thesis to its goal.

The second chapter explained the data preprocessing steps to prepare the point clouds needed for the registration part of the study.

The third chapter was focused on the registration process and related research along with presenting the correspondence preserving NR-ICP algorithm optimized for orthopaedics. Moreover, different evaluation methods to assess the performance of the proposed algorithm in terms of geometric fitting and anatomical correspondence were discussed.

The forth chapter explained how to develop an SSM from scapula models using Principal Component Analysis. In this chapter, the PCA method was also explained mathematically in detail.

In the fifth chapter, SSM results were presented and evaluation approaches to assess the quality of SSM were presented. The result of the SSM demonstrated that the first mode of variation, as predicted, represented size variation, the second mode of variation described changes in Critical Shoulder Angle (CSA) and the height of scapula main body, and the third mode of variation related closely to the size of glenoid cavity and the acromial position (i.e. Acromial tilt shifting superoanterior to superoposterior). The geometric registration error and correspondence error demonstrated that the developed algorithm is capable of accurately mapping a common Atlas to the complex and highly varied geometry of eroded scapulae. The robustness of the SSM was evaluated using three standard metrics: compactness, generality, and specificity. This showed that the SSM results elucidate the morphological variation of the scapula within the RTSA patient population. In addition, the anatomical measurements on all scapula models in the dataset as well as SSM results with explanation on standard coordinate system definition were performed and measurement outcomes were discussed on the studied population.

In the sixth chapter, statistical intensity modeling was discussed and bone intensity distribution on three different cross sections of scapula shape were demonstrated and compared for the first three modes of variation. The SIM results showed that the first mode of variation accounts for overall changes in intensity across the entire bone, while the second mode represents localized changes in the glenoid vault bone quality and the third mode demonstrated changes in bone intensity at the posterior and inferior glenoid rim associated with posteroinferior glenoid rim erosion. These data and analysis methods showed that they can significantly assist in the development of patient-specific planning technologies and musculoskeletal modeling that investigates the effects for morphological and bone property variation.

7.2 Limitations

This study has certain limitations:

1. The developed statistical shape models are a combination of B and E types and thus the resulting modes of variation and anatomical measurements combine the effects of these two different types of erosion. In the future, separate SSM models can be made to capture each erosion-type's modes of variation and be able to compare the anatomical measurement results between different types of erosion.
2. The material property assignment process used in SIM generation, did not account for Partial Volume Artifacts, which cause underestimation or overestimation of the material properties at the boundaries between two material types. Thus, a voxel that encompassed muscle and cortical bone tissue has a lower value than the theoretic Hounsfield value of the cortical bone as it is averaged between the theoretical HU values of the two tissues. Therefore, this artifact reduced the HU intensity at the outside cortical shell of the scapula bone models and resulted in unrealistically low cortical bone properties. In the future, the SIM models should be remade using material property assignment process that accounts for these Partial Volume Effects [140], [141].

7.3 Future works

The most direct way this work can be expanded is by developing SSMs and SIMs that are stratified by various variables of interest (e.g. sex, race, age, presence/type of glenoid erosion) to gain an understanding of if/how shape and bone property distribution varies across them. These findings would be able to guide implant design and determine the need for certain population specific implants.

For future research, sensitivity analysis on the choice of the source model for the registration algorithm can be performed to determine the effect of scapula size on the algorithm's error.

Future studies can focus on other bones like the humerus which are contained in the existing imaging datasets. Such an analysis will provide valuable insights in cases of pathological deformity in humerus bone morphology. As well, the SSM results can be used to generate subject-specific musculoskeletal models that eliminate errors associated with generic model parameters that are currently used and will enable studies of the effects on biomechanics of the interactions between bone shape morphology and implant design parameters. Furthermore, the SIM data combined with the SSM data can be used to systematically generate Finite Element Models that represent a specific, known portion of the patient population. Results from such a model will be significantly more generalizable and thus useful in orthopaedic implant design.

Deep learning methodologies have been involved in the creation of many important tools in medical imaging (e.g. image segmentation, tumor detection, image classification). This statistical modeling work could be combined with deep learning to yield a range of new orthopaedic innovations. This research direction is motivated by:

1. The difficult access to imaging data for patients with different races, sexes and ages. The combination of SSM and deep learning could provide data augmentation that could overcome this issues.
2. The segmentation of different medical image modalities (MRI, CT, etc.) using deep learning has shown promising results in adult population. The segmentation of pediatric bones remains a challenging task as the bone is in a growth phase and differentiating the growth cartilage tissue from the bone is not a straightforward task.
3. Classification of healthy and eroded shoulder using the anatomical measures extracted automatically from medical images along with the bone shape.

References

1. White, T.D. and P.A. Folkens, *The human bone manual*. 2005: Elsevier.
2. Vaughan, C.L., B.L. Davis, and J.C. O'connor, *Dynamics of human gait*. 1992: Human Kinetics Publishers.
3. Huri, G. and N.K. Paschos, *The shoulder*. 2017: Springer.
4. ELSEVIER. *3D4MEDICAL_Complete Anatomy 2021*. 2021; Available from: https://3d4medical.com/.
5. Wang, Q., et al., *Weight-bearing, muscle loading and bone mineral accrual in pubertal girls—a 2-year longitudinal study.* Bone, 2007. **40**(5): p. 1196-1202.
6. Rockwood, C.A., *The shoulder*. Vol. 1. 2009: Elsevier Health Sciences.
7. Moseley, H., *3 The Clavicle: Its Anatomy and Function.* Clinical Orthopaedics and Related Research®, 1968. **58**: p. 17-28.
8. Veeger, H. and F. Van Der Helm, *Shoulder function: the perfect compromise between mobility and stability.* Journal of biomechanics, 2007. **40**(10): p. 2119-2129.
9. Paine, R.M. and M. Voight, *The role of the scapula.* Journal of Orthopaedic & Sports Physical Therapy, 1993. **18**(1): p. 386-391.
10. PearsonEducation. *Shoulder muscles*. 2009; Available from: https://www.pearson.com/ca/en.html.
11. Terry, G.C. and T.M. Chopp, *Functional anatomy of the shoulder.* Journal of athletic training, 2000. **35**(3): p. 248.
12. Renfree, K.J. and T.W. Wright, *Anatomy and biomechanics of the acromioclavicular and sternoclavicular joints.* Clinics in sports medicine, 2003. **22**(2): p. 219-237.
13. Culham, E. and M. Peat, *Functional anatomy of the shoulder complex.* Journal of Orthopaedic & Sports Physical Therapy, 1993. **18**(1): p. 342-350.
14. StatisticsCanada. *Table 13-10-0096-06 Arthritis, by age group*. 2019; Available from: https://www150.statcan.gc.ca/t1/tbl1/en/tv.action?pid=1310009606.
15. Flatow, E.L., et al., *Instability of the shoulder: Complex problems and failed repairs. Part II. Failed repairs.* Journal of Bone and Joint Surgery, 1998. **80**(2): p. 284.
16. Robinson, C.M. and J. Aderinto, *Posterior shoulder dislocations and fracture-dislocations.* JBJS, 2005. **87**(3): p. 639-650.
17. Yamamoto, A., et al., *Prevalence and risk factors of a rotator cuff tear in the general population.* Journal of shoulder and elbow surgery, 2010. **19**(1): p. 116-120.
18. Aletaha, D. and J.S. Smolen, *Diagnosis and management of rheumatoid arthritis: a review.* Jama, 2018. **320**(13): p. 1360-1372.
19. Assouline-Dayan, Y., et al. *Pathogenesis and natural history of osteonecrosis*. in *Seminars in arthritis and rheumatism*. 2002. Elsevier.
20. Grogan, B.F. and C.M. Jobin, *Evaluation of Humeral and Glenoid Bone Deformity in Glenohumeral Arthritis*, in *Complex and Revision Shoulder Arthroplasty*. 2019, Springer. p. 3-13.
21. Ascione, F. and H.D. Routman, *Severe Glenoid Erosion (B2, B3, C, E2, E3) Treated with RSA*, in *Complex and Revision Shoulder Arthroplasty*. 2019, Springer. p. 59-73.

22. Millett, P.J., R. Gobezie, and R.E. Boykin, *Shoulder osteoarthritis: diagnosis and management.* American Family Physician, 2008. **78**(5): p. 605-611.
23. Walch, G., et al., *Morphologic study of the glenoid in primary glenohumeral osteoarthritis.* The Journal of arthroplasty, 1999. **14**(6): p. 756-760.
24. Bercik, M.J., et al., *A modification to the Walch classification of the glenoid in primary glenohumeral osteoarthritis using three-dimensional imaging.* Journal of shoulder and elbow surgery, 2016. **25**(10): p. 1601-1606.
25. Sirveaux, F., et al., *Grammont inverted total shoulder arthroplasty in the treatment of glenohumeral osteoarthritis with massive rupture of the cuff: results of a multicentre study of 80 shoulders.* The Journal of bone and joint surgery. British volume, 2004. **86**(3): p. 388-395.
26. Lévigne, C., et al., *Scapular notching in reverse shoulder arthroplasty.* Journal of shoulder and elbow surgery, 2008. **17**(6): p. 925-935.
27. Edmonds, A., *Shoulder arthroplasty.* Hand and Upper Extremity Rehabilitation: A Practical Guide, 2005: p. 389.
28. Bankes, M.J. and R.J. Emery, *Pioneers of shoulder replacement: themistocles Gluck and Jules Emile Péan.* Journal of Shoulder and Elbow Surgery, 1995. **4**(4): p. 259-262.
29. Flatow, E.L. and A.K. Harrison, *A history of reverse total shoulder arthroplasty.* Clinical Orthopaedics and Related Research®, 2011. **469**(9): p. 2432-2439.
30. Zadeh, H.G. and P.T. Calvert, *Recent advances in shoulder arthroplasty.* Current Orthopaedics, 1998. **12**(2): p. 122-134.
31. Wirth, M.A. and C.A. Rockwood Jr, *Current concepts review-complications of total shoulder-replacement arthroplasty.* JBJS, 1996. **78**(4): p. 603-16.
32. Evarts, C.M., *Surgery of the musculoskeletal system*. Vol. 1. 1983: Churchill Livingstone.
33. Sanchez-Sotelo, J., R.H. Cofield, and C.M. Rowland, *Shoulder hemiarthroplasty for glenohumeral arthritis associated with severe rotator cuff deficiency.* JBJS, 2001. **83**(12): p. 1814-1822.
34. Matsen III, F.A., et al., *The reverse total shoulder arthroplasty*. JBJS, 2007. **89**(3): p. 660-667.
35. ChoosePTGuide. *Physical Therapy Guide to Shoulder Replacement (Arthroplasty).* 2020; Available from: https://www.choosept.com/symptomsconditionsdetail/physical-therapy-guide-to-total-shoulder-arthroplasty-replacement.
36. Boileau, P., et al., *Grammont reverse prosthesis: design, rationale, and biomechanics.* Journal of shoulder and elbow surgery, 2005. **14**(1): p. S147-S161.
37. Berliner, J.L., et al., *Biomechanics of reverse total shoulder arthroplasty.* Journal of shoulder and elbow surgery, 2015. **24**(1): p. 150-160.
38. Walker, M., et al., *How reverse shoulder arthroplasty works.* Clinical Orthopaedics and Related Research®, 2011. **469**(9): p. 2440-2451.
39. Kontaxis, A. and G. Johnson, *The biomechanics of reverse anatomy shoulder replacement–a modelling study.* Clinical Biomechanics, 2009. **24**(3): p. 254-260.
40. Jobin, C.M., et al., *Reverse total shoulder arthroplasty for cuff tear arthropathy: the clinical effect of deltoid lengthening and center of rotation medialization.* Journal of shoulder and elbow surgery, 2012. **21**(10): p. 1269-1277.
41. Cheung, E., et al., *Complications in reverse total shoulder arthroplasty.* JAAOS-Journal of the American Academy of Orthopaedic Surgeons, 2011. **19**(7): p. 439-449.

42. Gunther, S.B. and T.L. Lynch, *Total shoulder replacement surgery with custom glenoid implants for severe bone deficiency.* Journal of shoulder and elbow surgery, 2012. **21**(5): p. 675-684.
43. Rodríguez, J.A., et al., *Pre-operative planning for reverse shoulder replacement: the surgical benefits and their clinical translation.* Ann Joint, 2019. **4**: p. 1-15.
44. Kasban, H., M. El-Bendary, and D. Salama, *A comparative study of medical imaging techniques.* International Journal of Information Science and Intelligent System, 2015. **4**(2): p. 37-58.
45. Beutel, J., H.L. Kundel, and R.L. Van Metter, *Handbook of medical imaging*. Vol. 1. 2000: Spie Press.
46. MaterialiseNV. *Materialise Mimics*. 2020; Available from: https://www.materialise.com/en/medical/mimics-innovation-suite/mimics.
47. Eldevik, K., W. Nordhøy, and A. Skretting, *Relationship between sharpness and noise in CT images reconstructed with different kernels.* Radiation protection dosimetry, 2010. **139**(1-3): p. 430-433.
48. Withey, D.J. and Z.J. Koles, *A review of medical image segmentation: methods and available software.* International Journal of Bioelectromagnetism, 2008. **10**(3): p. 125-148.
49. Withey, D.J. and Z.J. Koles. *Medical image segmentation: Methods and software*. in *2007 Joint Meeting of the 6th International Symposium on Noninvasive Functional Source Imaging of the Brain and Heart and the International Conference on Functional Biomedical Imaging*. 2007. IEEE.
50. Martin, C.M., et al., *Comparison of 3D reconstructive technologies used for morphometric research and the translation of knowledge using a decision matrix.* Anatomical sciences education, 2013. **6**(6): p. 393-403.
51. Mildenberger, P., M. Eichelberg, and E. Martin, *Introduction to the DICOM standard.* European radiology, 2002. **12**(4): p. 920-927.
52. AcademyMedical/MaterialiseMimics. *Mimics Innovation Suite Tutorials*. 2020; Available from: https://www.materialise.com/en/academy-medical/mimics-innovation-suite/tutorials.
53. Roscoe, L., *Stereolithography interface specification.* America-3D Systems Inc, 1988. **27**(2020): p. 10.
54. Leyden, R.N., et al., *Stereolithography method and apparatus*. 1992, Google Patents.
55. Materialise3-matic. *Tutorials*. 2020; Available from: https://www.materialise.com/en/academy-software/resources/3-matic.
56. Hruschka, V., et al., *Comparison of nanoparticular hydroxyapatite pastes of different particle content and size in a novel scapula defect model.* Scientific reports, 2017. **7**(1): p. 1-11.
57. Deserno, T.M., *Fundamentals of biomedical image processing*, in *Biomedical Image Processing*. 2010, Springer. p. 1-51.
58. Audette, M.A., F.P. Ferrie, and T.M. Peters, *An algorithmic overview of surface registration techniques for medical imaging.* Medical image analysis, 2000. **4**(3): p. 201-217.
59. Huysmans, T., J. Sijbers, and V. Brigitte, *Automatic construction of correspondences for tubular surfaces.* IEEE transactions on pattern analysis and machine intelligence, 2009. **32**(4): p. 636-651.

60. Zheng, G., et al., *A 2D/3D correspondence building method for reconstruction of a patient-specific 3D bone surface model using point distribution models and calibrated X-ray images.* Medical image analysis, 2009. **13**(6): p. 883-899.
61. Tam, G.K., et al., *Registration of 3D point clouds and meshes: A survey from rigid to nonrigid.* IEEE transactions on visualization and computer graphics, 2012. **19**(7): p. 1199-1217.
62. Rueckert, D., et al., *Nonrigid registration using free-form deformations: application to breast MR images.* IEEE transactions on medical imaging, 1999. **18**(8): p. 712-721.
63. Bellekens, B., et al., *A benchmark survey of rigid 3D point cloud registration algorithms.* Int. J. Adv. Intell. Syst, 2015. **8**: p. 118-127.
64. Johnson, A.E. and M. Hebert. *Surface registration by matching oriented points*. in *Proceedings. International Conference on Recent Advances in 3-D Digital Imaging and Modeling (Cat. No. 97TB100134)*. 1997. IEEE.
65. Pan, Y., et al. *Iterative global similarity points: A robust coarse-to-fine integration solution for pairwise 3d point cloud registration*. in *2018 International Conference on 3D Vision (3DV)*. 2018. IEEE.
66. Castellani, U. and A. Bartoli, *3d shape registration*, in *3D Imaging, Analysis and Applications*. 2020, Springer. p. 353-411.
67. Yambor, W.S., B.A. Draper, and J.R. Beveridge, *Analyzing PCA-based face recognition algorithms: Eigenvector selection and distance measures*, in *Empirical evaluation methods in computer vision*. 2002, World Scientific. p. 39-60.
68. Arun, K.S., T.S. Huang, and S.D. Blostein, *Least-squares fitting of two 3-D point sets.* IEEE Transactions on pattern analysis and machine intelligence, 1987(5): p. 698-700.
69. Marden, S. and J. Guivant. *Improving the performance of ICP for real-time applications using an approximate nearest neighbour search*. in *Proceedings of Australasian Conference on Robotics and Automation*. 2012.
70. Besl, P.J. and N.D. McKay. *Method for registration of 3-D shapes*. in *Sensor fusion IV: control paradigms and data structures*. 1992. International Society for Optics and Photonics.
71. Rusinkiewicz, S. and M. Levoy. *Efficient variants of the ICP algorithm*. in *Proceedings third international conference on 3-D digital imaging and modeling*. 2001. IEEE.
72. Rusu, R.B., *Semantic 3d object maps for everyday manipulation in human living environments.* KI-Künstliche Intelligenz, 2010. **24**(4): p. 345-348.
73. Censi, A. *An ICP variant using a point-to-line metric*. in *2008 IEEE International Conference on Robotics and Automation*. 2008. Ieee.
74. Low, K.-L., *Linear least-squares optimization for point-to-plane icp surface registration.* Chapel Hill, University of North Carolina, 2004. **4**(10): p. 1-3.
75. Segal, A., D. Haehnel, and S. Thrun. *Generalized-icp*. in *Robotics: science and systems*. 2009. Seattle, WA.
76. Allen, B., B. Curless, and Z. Popović, *Articulated body deformation from range scan data.* ACM Transactions on Graphics (TOG), 2002. **21**(3): p. 612-619.
77. Pekelny, Y. and C. Gotsman. *Articulated object reconstruction and markerless motion capture from depth video*. in *Computer Graphics Forum*. 2008. Wiley Online Library.
78. Chui, H. and A. Rangarajan, *A new point matching algorithm for non-rigid registration.* Computer Vision and Image Understanding, 2003. **89**(2-3): p. 114-141.

79. Myronenko, A. and X. Song, *Point set registration: Coherent point drift.* IEEE transactions on pattern analysis and machine intelligence, 2010. **32**(12): p. 2262-2275.
80. Papazov, C. and D. Burschka. *Deformable 3D shape registration based on local similarity transforms*. in *Computer Graphics Forum*. 2011. Wiley Online Library.
81. Feldmar, J. and N. Ayache, *Rigid, affine and locally affine registration of free-form surfaces.* International journal of computer vision, 1996. **18**(2): p. 99-119.
82. Liao, M., et al. *Modeling deformable objects from a single depth camera*. in *2009 IEEE 12th International Conference on Computer Vision*. 2009. IEEE.
83. Rouhani, M., E. Boyer, and A.D. Sappa. *Non-rigid registration meets surface reconstruction*. in *2014 2nd International Conference on 3D Vision*. 2014. IEEE.
84. Amberg, B., S. Romdhani, and T. Vetter. *Optimal step nonrigid ICP algorithms for surface registration*. in *2007 IEEE Conference on Computer Vision and Pattern Recognition*. 2007. IEEE.
85. Cover, T. and P. Hart, *Nearest neighbor pattern classification.* IEEE transactions on information theory, 1967. **13**(1): p. 21-27.
86. Bhatia, N., *Survey of nearest neighbor techniques.* arXiv preprint arXiv:1007.0085, 2010.
87. Friedman, J.H., J.L. Bentley, and R.A. Finkel, *An algorithm for finding best matches in logarithmic expected time.* ACM Transactions on Mathematical Software (TOMS), 1977. **3**(3): p. 209-226.
88. Sproull, R.F., *Refinements to nearest-neighbor searching in k-dimensional trees.* Algorithmica, 1991. **6**(1): p. 579-589.
89. Danckaers, F., et al. *Correspondence preserving elastic surface registration with shape model prior*. in *2014 22nd International Conference on Pattern Recognition*. 2014. IEEE.
90. Tihonkih, D., A. Makovetskii, and V. Kuznetsov. *A modified iterative closest point algorithm for shape registration*. in *Applications of Digital Image Processing XXXIX*. 2016. International Society for Optics and Photonics.
91. Shcherbakov, M.V., et al., *A survey of forecast error measures.* World Applied Sciences Journal, 2013. **24**(24): p. 171-176.
92. Chai, T. and R.R. Draxler, *Root mean square error (RMSE) or mean absolute error (MAE).* Geoscientific Model Development Discussions, 2014. **7**(1): p. 1525-1534.
93. Huttenlocher, D.P., G.A. Klanderman, and W.J. Rucklidge, *Comparing images using the Hausdorff distance.* IEEE Transactions on pattern analysis and machine intelligence, 1993. **15**(9): p. 850-863.
94. Mayya, M., et al., *Mesh correspondence improvement using regional affine registration: Application to statistical shape model of the scapula.* Irbm, 2015. **36**(4): p. 220-232.
95. Verborgt, O., et al., *Computer navigation and patient-specific instrumentation in shoulder arthroplasty.* Sports medicine and arthroscopy review, 2014. **22**(4): p. e42-e49.
96. Venne, G., et al., *Comparing conventional and computer-assisted surgery baseplate and screw placement in reverse shoulder arthroplasty.* Journal of shoulder and elbow surgery, 2015. **24**(7): p. 1112-1119.

97. Suero, E.M., et al., *Use of a custom alignment guide to improve glenoid component position in total shoulder arthroplasty.* Knee Surgery, Sports Traumatology, Arthroscopy, 2013. **21**(12): p. 2860-2866.
98. Cabarcas, B.C., et al., *Accuracy of patient-specific instrumentation in shoulder arthroplasty: a systematic review and meta-analysis.* JSES open access, 2019. **3**(3): p. 117-129.
99. Cootes, T.F., et al., *Trainable method of parametric shape description.* Image and Vision Computing, 1992. **10**(5): p. 289-294.
100. Cootes, T.F., et al., *Active shape models-their training and application.* Computer vision and image understanding, 1995. **61**(1): p. 38-59.
101. Blanz, V. and T. Vetter. *A morphable model for the synthesis of 3D faces*. in *Proceedings of the 26th annual conference on Computer graphics and interactive techniques*. 1999.
102. Heimann, T. and H.-P. Meinzer, *Statistical shape models for 3D medical image segmentation: a review.* Medical image analysis, 2009. **13**(4): p. 543-563.
103. Parker, A., et al. *Application of point distribution models to the automated analysis of echocardiograms*. in *Computers in Cardiology 1994*. 1994. IEEE.
104. Wang, S., W. Zhu, and Z.-P. Liang. *Shape deformation: SVM regression and application to medical image segmentation*. in *Proceedings Eighth IEEE International Conference on Computer Vision. ICCV 2001*. 2001. IEEE.
105. Jolliffe, I.T. and J. Cadima, *Principal component analysis: a review and recent developments.* Philosophical Transactions of the Royal Society A: Mathematical, Physical and Engineering Sciences, 2016. **374**(2065): p. 20150202.
106. Pearson, K., *LIII. On lines and planes of closest fit to systems of points in space.* The London, Edinburgh, and Dublin Philosophical Magazine and Journal of Science, 1901. **2**(11): p. 559-572.
107. Jolliffe, I.T., *Principal components in regression analysis*, in *Principal component analysis*. 1986, Springer. p. 129-155.
108. Wold, S., K. Esbensen, and P. Geladi, *Principal component analysis.* Chemometrics and intelligent laboratory systems, 1987. **2**(1-3): p. 37-52.
109. Shlens, J., *A tutorial on principal component analysis.* arXiv preprint arXiv:1404.1100, 2014.
110. Ringnér, M., *What is principal component analysis?* Nature biotechnology, 2008. **26**(3): p. 303-304.
111. King, A.P. and R. Eckersley, *Statistics for biomedical engineers and scientists: How to visualize and analyze data*. 2019: Academic Press.
112. Styner, M.A., et al. *Evaluation of 3D correspondence methods for model building*. in *Biennial International Conference on Information Processing in Medical Imaging*. 2003. Springer.
113. Davies, R., C. Twining, and C. Taylor, *Statistical models of shape: Optimisation and evaluation*. 2008: Springer Science & Business Media.
114. Salhi, A., et al., *Statistical shape modeling approach to predict missing scapular bone.* Annals of biomedical engineering, 2020. **48**(1): p. 367-379.
115. Munsell, B.C., P. Dalal, and S. Wang, *Evaluating shape correspondence for statistical shape analysis: A benchmark study.* IEEE Transactions on Pattern Analysis and Machine Intelligence, 2008. **30**(11): p. 2023-2039.

116. Grood, E.S. and W.J. Suntay, *A joint coordinate system for the clinical description of three-dimensional motions: application to the knee.* 1983.
117. van der Helm, F.C. *A standardized protocol for motion recordings of the shoulder*. in *First conference of the international shoulder group*. 1997. Shaker Publishers BV, Delft University of Technology The Netherlands.
118. Wu, G., et al., *ISB recommendation on definitions of joint coordinate systems of various joints for the reporting of human joint motion—Part II: shoulder, elbow, wrist and hand.* Journal of biomechanics, 2005. **38**(5): p. 981-992.
119. Verstraeten, T., L. De Wilde, and J. Victor, *The normal 3D gleno-humeral relationship and anatomy of the glenoid planes.* Journal of the Belgian Society of Radiology, 2018. **102**(1).
120. Jacobson, A., et al., *Glenohumeral anatomic study: a comparison of male and female shoulders with similar average age and BMI.* Bulletin of the NYU Hospital for Joint Diseases, 2015. **73**(1): p. S68.
121. Knowles, N.K., et al., *Quantification of the position, orientation, and surface area of bone loss in type B2 glenoids.* Journal of Shoulder and Elbow Surgery, 2015. **24**(4): p. 503-510.
122. Li, X., et al., *Relationship between the critical shoulder angle and shoulder disease.* Jbjs Reviews, 2018. **6**(8): p. e1.
123. Knowles, N.K., L.M. Ferreira, and G.S. Athwal, *Premorbid retroversion is significantly greater in type B2 glenoids.* Journal of Shoulder and Elbow Surgery, 2016. **25**(7): p. 1064-1068.
124. Boileau, P., et al., *The reverse shoulder arthroplasty angle: a new measurement of glenoid inclination for reverse shoulder arthroplasty.* Journal of Shoulder and Elbow Surgery, 2019. **28**(7): p. 1281-1290.
125. Matsumura, N., et al., *Computed tomography measurement of glenoid vault version as an alternative measuring method for glenoid version.* Journal of Orthopaedic Surgery and Research, 2014. **9**(1): p. 1-7.
126. Moineau, G., et al., *Three-dimensional measurement method of arthritic glenoid cavity morphology: feasibility and reproducibility.* Orthopaedics & Traumatology: Surgery & Research, 2012. **98**(6): p. S139-S145.
127. Thomas, S.J., et al., *Internal rotation and scapular position differences: a comparison of collegiate and high school baseball players.* Journal of Athletic Training, 2010. **45**(1): p. 44-50.
128. Watson, L., et al., *Measurement of scapula upward rotation: a reliable clinical procedure.* British Journal of Sports Medicine, 2005. **39**(9): p. 599-603.
129. Van Rietbergen, B. and K. Ito, *A survey of micro-finite element analysis for clinical assessment of bone strength: the first decade.* Journal of biomechanics, 2015. **48**(5): p. 832-841.
130. Keaveny, T.M., *Biomechanical computed tomography—noninvasive bone strength analysis using clinical computed tomography scans.* Annals of the New York Academy of Sciences, 2010. **1192**(1): p. 57-65.
131. Engelke, K., B. van Rietbergen, and P. Zysset, *FEA to measure bone strength: a review.* Clinical reviews in bone and mineral metabolism, 2016. **14**(1): p. 26-37.

132. Soltanmohammadi, P., et al., *Investigating the Effects of Demographics on Shoulder Morphology and Density Using Statistical Shape and Density Modeling.* Journal of Biomechanical Engineering, 2020. **142**(12): p. 121005.
133. Geuzaine, C. and J.F. Remacle, *Gmsh: A 3-D finite element mesh generator with built-in pre-and post-processing facilities.* International journal for numerical methods in engineering, 2009. **79**(11): p. 1309-1331.
134. meshio. *mesh format convertor code*. 2020; Available from: https://pypi.org/project/meshio/.
135. Rietbergen, B.v., *Mechanical behavior and adaptation of trabecular bone in relation to bone morphology*. 1996: [Sl: sn].
136. ParaView. *data visualization software*. 2020; Available from: https://www.paraview.org/.
137. Melis, B., et al., *Glenoid loosening and failure in anatomical total shoulder arthroplasty: is revision with a reverse shoulder arthroplasty a reliable option?* Journal of shoulder and elbow surgery, 2012. **21**(3): p. 342-349.
138. Farron, A., A. Terrier, and P. Büchler, *Risks of loosening of a prosthetic glenoid implanted in retroversion.* Journal of shoulder and elbow surgery, 2006. **15**(4): p. 521-526.
139. Matsen III, F.A., et al., *Glenoid component failure in total shoulder arthroplasty.* JBJS, 2008. **90**(4): p. 885-896.
140. Glover, G. and N. Pelc, *Nonlinear partial volume artifacts in x-ray computed tomography.* Medical physics, 1980. **7**(3): p. 238-248.
141. Hsieh, J. *Partial volume artifact reduction in computed tomography*. in *Proceedings of 3rd IEEE International Conference on Image Processing*. 1996. IEEE.

Appendix A

Calculation for eigenvectors and eigenvalues in high dimensional matrices like X:

$$Cov(s) = \frac{1}{N-1} XX^T$$

And a smaller matrix D is defined as:

$$D = \frac{1}{N-1} X^T X$$

And eigenvalues (γ) and eigenvectors (ψ) are now computable by:

$$D\,\psi = \gamma\,\psi$$

Then:

$$\frac{1}{N-1} X^T X\,\psi = \gamma\,\psi$$

$$X^T X\,\psi = (N-1)\,\gamma\,\psi$$

If we left multiply both sides with matrix X:

$$X(X^T X\,\psi) = X((N-1)\,\gamma\,\psi)$$

$$XX^T(X\,\psi) = (N-1)\,\gamma(X\,\psi)$$

$$\frac{1}{(N-1)} XX^T(X\,\psi) = \gamma(X\,\psi)$$

Finally, we have:

$$Cov(s)(X\,\psi) = \gamma(X\,\psi)$$

And eigenvectors (φ) of initial covariance matrix are:

$$\varphi = X\psi$$

Or for eigenvector of each observation (i) in X:

$$\varphi_i = \frac{1}{\sqrt{\gamma_i N}} X\psi_i$$

And eigenvalues (λ) are:

$$\lambda = \gamma$$

Appendix B

Detailed information of correspondence error results for 12 landmarks chosen from different regions of scapula on 10 randomly selected models by observer 1 and 2.

		Model Number										STD per landmark	Average error by landmark	Average error by region	Regions
		1	2	3	4	5	6	7	8	9	10				
Landmark Number	1	3.34	5.46	2.87	4.65	0.00	1.20	3.40	4.81	6.57	4.60	**1.87**	**3.69**	**3.42**	**Acromion**
	2	6.66	2.63	1.88	2.89	8.39	2.24	5.16	4.58	7.91	6.66	**2.30**	**4.90**		
	3	3.08	1.17	2.96	1.92	2.34	0.00	1.41	1.81	1.31	0.75	**0.91**	**1.68**		
	4	1.04	1.87	1.37	0.91	2.96	1.70	1.17	1.71	0.00	1.51	**0.72**	**1.42**	**1.42**	**Coracoid**
	5	0.52	2.39	1.80	1.40	0.80	2.11	2.03	0.79	0.61	2.35	**0.71**	**1.48**	**1.48**	**Notch**
	6	0.79	1.06	1.13	1.91	3.55	2.21	1.62	2.15	2.23	3.82	**0.95**	**2.05**	**2.53**	**Glenoid**
	7	1.94	2.29	0.00	0.95	1.19	3.50	2.87	2.02	1.65	0.59	**1.00**	**1.70**		
	8	6.50	3.36	3.14	3.97	6.17	1.22	1.92	3.30	3.95	4.66	**1.57**	**3.82**		
	9	2.60	3.56	0.99	1.37	2.42	4.96	2.18	1.36	1.86	4.10	**1.23**	**2.54**		
	10	1.58	5.09	2.38	1.38	2.40	2.51	2.15	2.26	4.78	1.89	**1.20**	**2.64**	**2.64**	**Spine**
	11	2.65	4.54	1.49	1.20	1.13	8.12	1.91	2.68	1.17	0.97	**2.12**	**2.59**	**2.31**	**Body**
	12	4.01	3.09	1.59	1.19	1.97	2.57	1.96	1.77	0.43	1.70	**0.95**	**2.03**		
STD per model		**1.94**	**1.37**	**0.88**	**1.17**	**2.27**	**2.01**	**1.03**	**1.17**	**2.43**	**1.84**				
Average error by model		**2.89**	**3.04**	**1.80**	**1.98**	**2.78**	**2.70**	**2.32**	**2.44**	**2.71**	**2.80**				

Figure 68. Correspondence error results for 12 landmarks on 10 randomly selected models by observer 1.

		Model Number										STD per landmark	Average error by landmark	Average error by region	Regions
		1	2	3	4	5	6	7	8	9	10				
Landmark Number	1	2.71	3.62	4.88	3.23	2.79	1.20	4.74	6.70	6.11	2.96	**1.61**	**3.89**	**3.87**	**Acromion**
	2	14.22	1.49	1.44	3.82	7.43	1.90	6.33	8.25	8.23	4.14	**3.81**	**5.72**		
	3	0.62	2.80	3.25	1.69	0.87	3.88	3.80	1.03	0.79	1.19	**1.24**	**1.99**		
	4	1.04	1.87	0.00	1.74	1.94	1.70	1.62	2.92	0.75	0.96	**0.76**	**1.45**	**1.45**	**Coracoid**
	5	0.27	2.85	1.46	1.40	0.35	1.57	1.04	1.48	1.59	2.87	**0.82**	**1.49**	**1.49**	**Notch**
	6	2.29	1.91	3.32	1.11	3.01	1.77	0.89	0.95	2.42	4.33	**1.06**	**2.20**	**3.36**	**Glenoid**
	7	1.96	2.99	2.95	1.74	5.50	4.42	5.66	2.79	0.69	1.85	**1.57**	**3.05**		
	8	8.70	9.83	4.69	3.97	7.57	8.76	2.69	2.21	2.88	3.92	**2.74**	**5.52**		
	9	1.97	3.74	1.05	5.41	1.78	3.70	1.19	0.95	1.88	5.09	**1.59**	**2.68**		
	10	0.00	3.56	0.68	0.64	1.19	2.21	1.35	0.70	3.77	1.89	**1.20**	**1.60**	**1.60**	**Spine**
	11	2.31	4.39	7.05	1.41	1.78	6.13	3.07	2.80	0.00	0.89	**2.15**	**2.98**	**2.77**	**Body**
	12	3.69	6.52	0.81	1.80	1.99	3.81	1.56	2.19	0.53	2.65	**1.67**	**2.55**		
STD per model		**3.95**	**2.22**	**2.02**	**1.38**	**2.36**	**2.14**	**1.82**	**2.27**	**2.39**	**1.35**				
Average error by model		**3.31**	**3.80**	**2.63**	**2.33**	**3.02**	**3.42**	**2.83**	**2.75**	**2.47**	**2.73**				

Figure 69. Correspondence error results for 12 landmarks on 10 randomly selected models by observer 2.